

## ABSTRACT

Title of dissertation:     **DIAGNOSING CLOUDS AND HAZES  
IN EXOPLANET ATMOSPHERES**

Jonathan David Fraine, Doctor of Philosophy, 2015

Dissertation directed by:  Professor L. Drake Deming  
                                  Department of Astronomy

Exoplanet atmospheres provide a probe into the conditions on alien worlds, from hot Jupiters to Super-Earths. We can now glimpse the behaviour of extreme solar systems that defy our understanding of planet formation and capture our imaginations about the possibilities for understanding planets and life in our universe.

I combined multi-epoch, multi-instrument observations from both space and ground based facilities. I developed observational techniques and tools to constrain exoplanetary atmospheric compositions, temperature profiles, and scale heights over a span of planetary masses and wavelengths, that provided a probe into the properties of these diverse planetary atmospheres.

I led a team that used the Spitzer Space Telescope, with the IR Array Camera (IRAC), to observe the well known transiting Super-Earth, GJ 1214b ( $\sim 2.7 R_{\oplus}$ ). My precisely constrained infrared transit depth, error  $\sim \mathcal{O}(40 \text{ ppm})$ , significantly constrained the lack of any molecular detections out to a wavelength of  $5\mu\text{m}$ . The significance of this null detection challenges self-consistent models for the atmosphere of this super-Earth. Models must invoke thick, grey opacity clouds that

uniformly cause the atmosphere to be opaque at all wavelengths.

My team and I used the Hubble Space Telescope Wide Field Camera 3 (HST-WFC3) to spectroscopically probe the atmosphere of the transiting warm Neptune, HAT-P-11b ( $\sim 4.5 R_{\oplus}$ ), and detected the first molecular signature from a small exoplanet ( $R_p < R_{\text{Saturn}}$ ), inferring the presence of a hydrogen rich atmosphere. The average densities of many transiting exoplanets are known, but the degree to which atmospheric composition – abundance of Hydrogen relative to other atoms and molecules – correlates with the bulk composition has not yet been established. In an effort to characterize the atmospheric metallicity in greater detail, my team observed HAT-P-11 using warm Spitzer IRAC at 3.6 and 4.5  $\mu\text{m}$ . The non-detections of eclipses HAT-P-11b provided upper limits on the temperature profile at 3.6 and 4.5  $\mu\text{m}$ .

I am one of the founding members of the ACCESS collaboration (Arizona-CfA-Católica Exoplanet Spectroscopy Survey), a ground based observational campaign to spectroscopically survey a catalogue of exoplanetary atmospheres using major optical telescopes. I observed several of our targets from the 6.5m Magellan-Baade telescope. The results of my first observation provided low signal-to-noise constraints on the cloud properties of the hot Jupiter WASP-4b, as well as the UV radiation environment produced by its host star, WASP-4.

The combination of these observational constraints provided greater insight into the end-products of the planet formation process, and developed the knowledge base of our community for both cloudy and clear worlds.

DIAGNOSING CLOUDS AND HAZES  
IN EXOPLANET ATMOSPHERES

by

Jonathan David Fraine

Dissertation submitted to the Faculty of the Graduate School of the  
University of Maryland, College Park in partial fulfillment  
of the requirements for the degree of  
Doctor of Philosophy  
2015

Advisory Committee:  
Professor L. Drake Deming, Chair/Advisor  
Professor Derek R. Richardson, Co-Advisor  
Professor J. Patrick Harrington  
Professor Andrés Jordán  
Professor Heather A. Knutson

© Copyright by Jonathan David Fraine 2015

## Preface

Two of the major components of this Ph.D. thesis were previously published. The first of which (Chapter 2) was published in the *Astrophysical Journal*. The second (Chapter 3) was published in *Nature*. The following table details the titles, authors, and dates of publication:

Title	Authors	Publication Date	Chapter
Spitzer Transits of the Super-Earth GJ 1214b and Implications for Its Atmosphere	Jonathan D. Fraine, Drake Deming, Michaël Gillon, Emmanuël Jehin, Brice-Olivier Demory, Björn Benneke, Sara Seager, Nikole K. Lewis, Heather Knutson, and Jean-Michel Désert	03/2013	§2
Water Vapour Absorption in the Clear Atmosphere of a Neptune-sized Exoplanet	Jonathan Fraine, Drake Deming, Björn Benneke, Heather Knutson, Andrés Jordán, Néstor Espinoza, Nikku Madhusudhan, Ashlee Wilkins, and Kamen Todorov	09/2014	§3

## Dedication

I dedicated this thesis to my family; to my parents, sister, and nieces, who have forever inspired me to shoot for the stars; to my wife who has supported me emotionally through the worst of times and the best of times; and to our unborn son, with whom I hope to share a life of intrigue, happiness, and, above all, curiosity.

## Acknowledgments

I owe my gratitude to all the people who have made this thesis possible and because of whom my graduate experience has been one that I will cherish forever.

First and foremost I'd like to thank my advisor, Professor Drake Deming for giving me an invaluable opportunity to work on challenging and extremely interesting projects over the past four years. He has always made himself available for help and advice; there has never been an occasion when I've knocked on his door and he hasn't given me time. He always allowed me the freedom to explore every avenue available to me, while still keeping me focused on the project at hand. It has been a pleasure to work with and learn from such an extraordinary scientist.

I would also like to thank my co-advisors, Drs. Heather Knutson and Andrés Jordán. Without their extraordinary support and continual guidance, I would never have come close to being who I am today. They both provided me with incomparable experiences that literally took me around the world.

Thanks are due to Professors Derek Richardson and Patrick Harrington for agreeing to serve on my thesis committee and for sparing their invaluable time reviewing the manuscript. They both kept my focus on the goals of my own research, while providing an amazing platform to grasp at the bigger picture.

My colleagues at the University of Maryland, California Institute of Technology, and Pontificia Universidad Católica have enriched my graduate life in many ways and deserve a special mention.

I would like to acknowledge the help and support from the staff members

at the University of Maryland, California Institute of Technology, and Pontificia Universidad Católica. There are so many people in our departments that have helped me over these many years, that I can only say: thank you all for your support, patience, and unwavering care for me and my fellow graduate students.

I owe my deepest thanks to my family and my wife. To my mother and father, who have always supported and guided me through my life, and have pulled me through against impossible odds at times. Words cannot express the gratitude I owe them. To my wife, who has emotionally and physically held my hand through this tumultuous and trying time in our lives; without her kindness and understanding, I do not know how I would have succeeded.

I would also like to thank Drs. Eve Ostriker, Casey Lisse, Joe Harrington, and Marc Kuchner who nurtured me in the infancy of my career. I have come a very long way in research, science, and life, but without you I could have never begun this journey.

It is impossible to remember all the wonderful people who have inspired and helped me over the years. I would like to take this time to thank you all for your part in bringing me to this success and happiness.

Let us all work together to inspire our world towards a greater future.

I would also like to thank my collaborators who provided code, insight, support, funding, and guidance.

Highest amongst them is my advisor, Dr. Drake Deming, who led me along my path from a graduate student into a doctor. In addition to funding, support, and guidance, Dr. Drake deming also provided code, planetary spectroscopic predictions, and stellar atmospheric modeling that contributed greatly to my publications and success.

Additionally, Drs Drake Deming, Heather Knutson, and Andres Jordan provided access to telescopes and observations. Access to such amazing and rich data sets provided me with an incredible starting position for each of my 4 papers (2 published, 2 in preparation).

Collaborators such as Michael Gillon and Emmanuel Jehin provided high level data sets from observations and analyses that they conducted using the 0.6m TRAPPIST telescope in Chile.

Drs Bjorn Benneke and Sara Seager provided critical model atmospheric spectra with to compare our observations and from which to constrain the atmospheric physics of these alien worlds. Dr Bjorn Benneke and I worked very closely together to interpret the spectra of the transiting exo-Neptune HAT-P-11b in our paper Fraine et al. 2014. Dr Benneke developed his advanced self-consistent atmospheric retrieval pipeline (SCARLET) and provided robust statistical constraints on the atmosphere of HAT-P-11b from observations that I analyzed.

Drs Nikole Lewis and Heather Knutson worked closely with me to develop my Spitzer data analysis pipeline that implemented Dr Lewis's 3-Dimensional Spitzer

systematic interpretation “Pixel Mapping” algorithm.

Dr Andres Jordan and Nestor Espinoza provided both computing resources and theoretical stellar atmospheric interpretations using their newly developed limb darkening fitting algorithm from theoretical stellar models.

Drs Drake Deming, Heather Knutson, and Andres Jordan provided substantial computing resources that I used to analyze our observational data sets and compute robust statistical boundaries on the atmospheric physics of these alien worlds.

# Table of Contents

List of Tables	xii
List of Figures	xiii
List of Abbreviations	xiv
1 Introduction	1
1.1 Transmission Spectroscopy	7
1.2 Scale Height and Observability	10
1.3 Thermochemical equilibrium and Disequilibrium Chemistry	13
1.4 Correlated Noise Sources: Astrophysical and Instrumental Noise	22
1.5 Thesis Organisation	24
2 Infrared Transmission Spectroscopy of a Super-Earth	26
2.1 Introduction	27
2.2 Observations	31
2.2.1 Spitzer	31
2.2.2 TRAPPIST	32
2.3 Spitzer Photometry	32
2.3.1 Aperture Photometry	32
2.3.2 Decorrelation	34
2.4 Model Fitting for Transit Parameters	37
2.4.1 Spitzer 4.5 $\mu\text{m}$ Transits	39
2.4.2 Spitzer 3.6 $\mu\text{m}$ Transits	42
2.4.3 TRAPPIST I+z Transits	44
2.4.4 Errors	45
2.4.5 System Parameters	48
2.5 Transit-to-Transit Variability and Star Spots	51
2.6 The Atmosphere of GJ1214b	54
2.6.1 Comparing Models to Observations	55
2.6.2 Implications from Spitzer	58
2.6.3 A $\chi^2$ Analysis	59

2.6.4	Systematic Differences Between Observers . . . . .	62
2.6.5	Summary of Implications for the Atmosphere of GJ1214b . . . . .	63
3	Water Vapor Absorption in the Clear Atmosphere of an exo-Neptune . . . . .	66
3.1	Introduction . . . . .	67
3.2	Observations . . . . .	69
3.2.1	Hubble WFC3 Spectroscopy and White Light Photometry . . . . .	71
3.2.2	Warm Spitzer IRAC . . . . .	72
3.2.3	Kepler Archival Transits . . . . .	73
3.3	Data Analysis . . . . .	73
3.3.1	Limb-Darkening Coefficients . . . . .	73
3.3.2	Hubble Wide Field Camera 3 . . . . .	75
3.3.2.1	WFC3 Exponential and Linear Instrumental Noise Profiles . . . . .	79
3.3.2.2	Deriving the HST WFC3 Exoplanet Spectrum . . . . .	81
3.3.3	Warm Spitzer IRAC . . . . .	84
3.3.4	Kepler Archival Observations . . . . .	85
3.4	Discussion . . . . .	87
3.4.1	Detection of Water Vapor Absorption in the Clear Atmo- sphere of an exo-Neptune . . . . .	87
3.4.2	The Nature of Starspots on HAT-P-11 . . . . .	89
3.4.3	Constraining the Significance of Water Vapour in Starspots . . . . .	91
3.4.4	Self-Consistent Atmospheric Retrieval for Exoplanets . . . . .	93
3.5	Conclusions . . . . .	95
4	Warm Spitzer Eclipse Photometry of HAT-P-11b . . . . .	98
4.1	Introduction . . . . .	100
4.2	Observations . . . . .	103
4.3	Analysis . . . . .	105
4.3.1	Aperture Photometry . . . . .	105
4.3.2	Decorrelation . . . . .	107
4.3.3	Binning . . . . .	112
4.3.4	Peak-up Observing Mode . . . . .	112
4.3.5	Selecting the Best Aperture Radius . . . . .	114
4.4	Discussion . . . . .	119
4.4.1	Equilibrium Temperature Eclipse Depth Predictions . . . . .	119
4.4.2	Searching for an Eclipse . . . . .	121
4.4.3	Deriving Eclipse Depth Upper Limits . . . . .	124
4.4.4	Bayesian Information Criterion . . . . .	127
4.5	Conclusions . . . . .	128
5	Ground Based Spectroscopic Surveys of Exoplanetary Atmospheres . . . . .	131
5.1	Introduction . . . . .	131

5.2	Observations . . . . .	137
5.2.1	Spectroscopic Surveys for Exoplanetary Atmospheres . . . . .	140
5.2.2	Multi-Object Spectroscopy . . . . .	143
5.2.3	ACCESS Observations of WASP-4b . . . . .	144
5.2.3.1	White Light Curve . . . . .	145
5.2.3.2	Transmission Spectrum and Chromatic Noise . . . . .	146
5.2.4	Clouds in WASP-4b . . . . .	148
5.3	Future Work . . . . .	150
5.3.1	Improving the Transmission Spectrum of WASP-4b . . . . .	150
5.3.2	ACCESS Collaboration Survey . . . . .	151
5.3.3	Planet Formation Constraints . . . . .	153
6	Looking Forward: Where Will We Go Next?	154
	Bibliography	159

## List of Tables

2.1	IRAC channel 2 list of orbital parameters and radius ratios for all . . .	40
2.2	IRAC channel 1 list of orbital parameters and radius ratios for all . . .	43
2.3	TRAPPIST list of orbital parameters and radius ratios for all . . . . .	45
2.4	Results from combined observations per channel . . . . .	49
2.5	Results after enforcing orbital solutions . . . . .	65
3.1	Summary of observations. . . . .	71
3.2	The system and planetary parameters of HAT-P-11b. . . . .	75
3.3	Transmission spectrum table . . . . .	97
4.1	Catalogue of our 9 observations . . . . .	104
4.2	List of eclipse depth upper limits and black body predicted . . . . .	125

## List of Figures

1.1	Observational geometry for transmission and emission spectroscopy . . . . .	3
1.2	Radius versus mass measurement for transiting exoplanets . . . . .	5
1.3	Geometry for transmission spectroscopy . . . . .	9
1.4	Cloud production and sedimentation curves . . . . .	15
1.5	Effect of metallicity on temperature-pressure curves . . . . .	17
1.6	Example of mixing ratios – abundances of molecules as a function of pressure/altitude – for GJ 436b . . . . .	19
2.1	2.9 days subsection of IRAC Channel 2 raw data . . . . .	35
2.2	20.2 days of decorrelated IRAC Channel 2 data . . . . .	38
2.3	2.9 days subsection of IRAC Channel 2 decorrelated data . . . . .	39
2.4	IRAC Channel 2 red noise curve for combined transits . . . . .	41
2.5	IRAC Channel 2 phased and binned transit . . . . .	42
2.6	IRAC Channel 1 phased and binned transit . . . . .	44
2.7	IRAC Channel 1 red noise curve for combined transits . . . . .	46
2.8	TRAPPIST phased and binned transit . . . . .	47
2.9	TRAPPIST red noise curve for combined transits . . . . .	48
2.10	Radius ratio variations over time . . . . .	50
2.11	IRAC Channel 2 Radius ratio MCMC posterior . . . . .	51
2.12	Spitzer IRAC transmission spectrum . . . . .	57
2.13	Optical-NIR transmission spectrum . . . . .	59
3.1	White light transit curves and starspot crossing temperature estimates. . . . .	70
3.2	HST White Light Curve with exponential ramp effects. . . . .	72
3.3	HAT-P-11 Kepler light curve for $\sim 4$ years of short cadence. . . . .	74
3.4	The distribution of Kepler starspot crossing anomalies. . . . .	76
3.5	An example of WFC3 scanning mode observation spectral images. . . . .	77
3.6	WFC3 white light curve exponential ramp parameters correlations . . . . .	81
3.7	Wavelength Dependent Transit Light Curves. . . . .	83
3.8	The transmission spectrum of HAT-P-11b. . . . .	84
3.9	Spectral retrieval results of our transmission spectrum. . . . .	88
4.1	Eight epochs of our warm Spitzer-IRAC observations. . . . .	108

4.2	Example PLD components . . . . .	111
4.3	Eight epochs of warm Spitzer-IRAC observations Root-N curves . . .	116
4.4	2D maps of $\chi^2_{RMS}$ and $\sigma^2$ vs white noise . . . . .	117
4.5	Example decorrelated photometry for 176 aperture radii . . . . .	118
4.6	Example Root-N curves for 176 aperture radii . . . . .	119
4.7	A map of $\Delta\chi^2$ over central phases for eclipse curve . . . . .	122
4.8	MCMC posterior probability distributions . . . . .	124
4.9	$\Delta BIC$ comparing 176 light curves with null hypothesis . . . . .	128
5.1	Atmospheric metallicity versus planetary mass . . . . .	133
5.2	Radius versus mass for 200 transiting exoplanets . . . . .	134
5.3	Comparison between WASP-4b, WASP-6b, HD 189733b optical spectra.	142
5.4	ACCESS collaboration region of opportunity . . . . .	152

## List of Abbreviations

$\delta$	Exoplanet eclipse depth
$\epsilon_\lambda$	Number of scale heights over which the atmosphere is opaque
$H_p$	Scale height
$D$	Planetary transit depth
$R_p$	Planetary radius
$M_p$	Planetary mass
$T_p$	Planetary temperature
$\rho_p$	Planetary density
$R_s$	Stellar radius
$M_s$	Stellar mass
$T_s$	Stellar temperature
$Z$	Planetary atmospheric metallicity
BIC	Bayesian Information Criterion
HST	Hubble Space Telescope
IR	Infrared
IRAC	Infrared Array Camera
JWST	James Webb Space Telescope
LDC	Limb Darkening Coefficient
WFC3	Wide Field Camera 3
UV	Ultraviolet

## Chapter 1: Introduction

The science of extrasolar planets provides context for our own origins. Starting from a statistical platform, the catalogue of known exoplanets provides a basis to discover if our Solar System – our origins – is unique or normal. Although we have just begun to explore the diversity of alien worlds, and have yet to observationally constrain systems like our own Solar System, we are now able to step forward and grasp at the periphery of those important questions.

Planet formation theory predicts that water abundance in the protoplanetary disk – the natal environment for planet formation – could be a key factor for the growth of giant planets [1]. We are currently unable to measure robust constraints for water abundance in the Solar System giant planets because the majority of water vapor condensed out in cloud layers beneath our observable regime [2]. Our community has detected extrasolar giant planets that are close enough to their host stars for the majority of water molecules to be sustained in the vapour phase [3]. Comparing a statistically robust distribution of water abundance as a function of planetary temperature and planetary mass could provide limits for the water abundance of all giant planets, including those in our Solar System.

Some theories that could explain planet formation also predict an inverse re-

lationship between planetary mass and mean molecular weight – the average mass of particles in the atmospheres [4]. This correlation is weakly inferred from our Solar System because Jupiter and Saturn are much more massive than Uranus and Neptune, while the average density of Uranus and Neptune is larger than that of Jupiter and Saturn. By comparing the mass and radius measurements from 200 transiting exoplanets, [5] found this same trend exists in the exoplanet population. This correlation between planetary mass and bulk density supports the “core accretion” theory of planet formation, but leaves some key questions unanswered [6]. Exoplanet science can provide key insight into all facets of planet formation theory by providing a distribution of planets to analyze over all planetary and stellar properties [5,6].

Transiting exoplanets are those planets which fortuitously pass between their host star and the Earth (see Figure 1.1) [7]. Although this opportunity is only afforded to us from a small fraction of the extrasolar planets in our galaxy –  $\sim 0.5\%$  for exo-Earths around Sun-like stars – it is technologically efficient, with distinct advantages not produced by other techniques [11]. Additionally, the transit geometry provides the most information per observation (Figure 1.1) [7,12,13]. When a planet transits its host star, there is a well understood dip in light from the star-planet system as a function of time; this is called the transit depth,  $\delta$  [14,15]. The transit depth is directly related to area ratio of the planetary disc to the stellar disc:

$$\delta = A_{planet}/A_{star} = (R_p/R_s)^2. \quad (1.1)$$

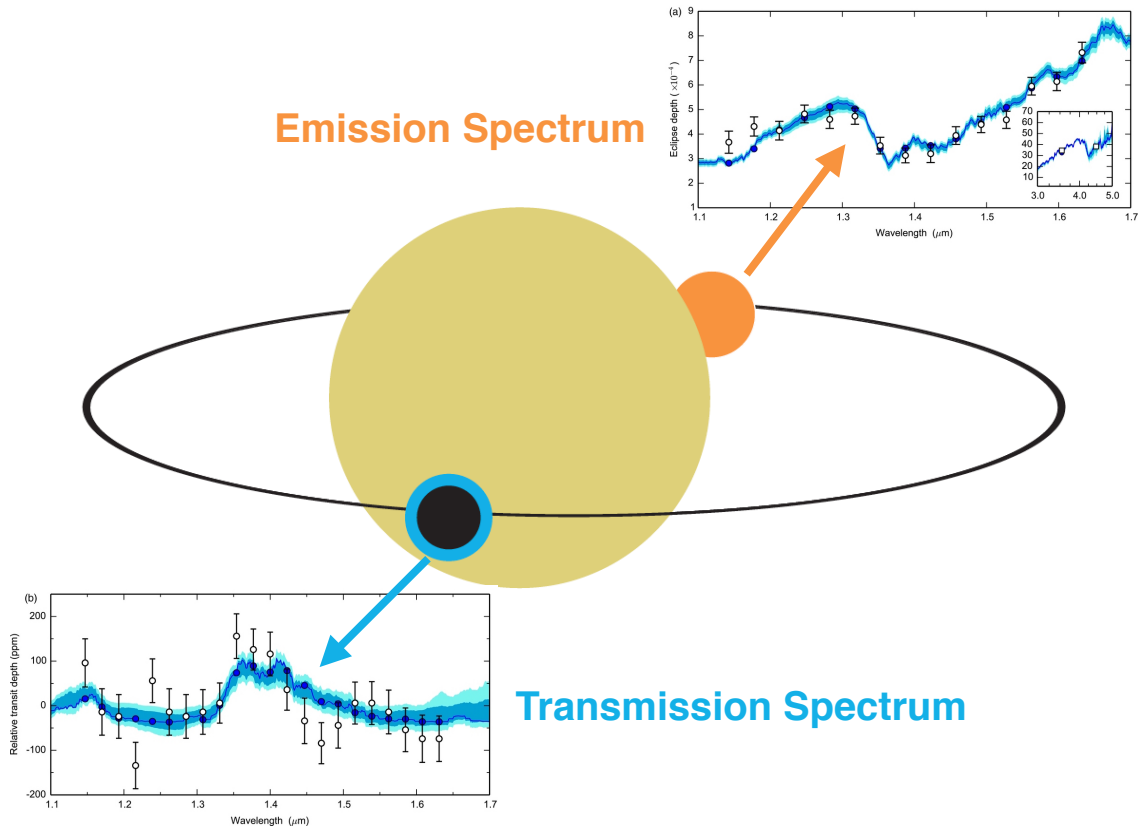


Figure 1.1: This diagram shows the observational geometry for both transmission and emission spectroscopy. The emission spectrum (upper right) is measured by spectroscopically observing the flux from the star + planet as the exoplanet passes behind its host star, constraining the planetary eclipse depth as a function of wavelength. Emission spectra probe the exoplanetary atmospheric temperature-pressure profile [7,8]. The transmission spectrum (lower left) is measured by spectroscopically observing the host star as the exoplanet passes between our detectors and the star, constraining the planetary transit depth as a function of wavelength [7]. Transmission spectra probe the molecular absorption in the upper atmosphere through the scale height [9,10]. In both sub-frames, the dark blue region highlights the  $1\sigma$  model uncertainty boundaries and the light blue region highlights the  $2\sigma$  model uncertainty boundaries. They each provide an independent constraint on the molecular abundances and atmospheric metallicities; combining them produces a significantly more robust measurement of the molecular abundances, atmospheric metallicities, and cloud-top pressures.

Because of the simplicity of this measurement, a transit can be detected orbiting much fainter stars than, for example, radial velocity (RV) detections – because RV is a spectroscopic technique and spreads the stellar light out over many pixels. This simple geometric measurement is the key to unlocking a vast heterogeneity of physical properties within exoplanetary atmospheres; including scale heights, molecular abundances, temperature profiles, kinematics, interior structure, cloud top pressures, and atmospheric metallicities (the mass fraction of elements heavier than hydrogen and helium, relative to Solar) [9, 10, 16–22].

For the brighter host stars that also have mass constraints from radial velocity measurements, as well as radius constraints from transit light curves, our community has measured the densities for hundreds of exoplanets [5, 22–24]. These measurements allow us to interpret the distribution of bulk densities across many regimes of internal and atmospheric structures. From these bulk densities alone, we can begin to understand the average properties of exoplanets. We can determine if they are hydrogen dominated, water worlds, solid cores, or a mixture [22, 25–31]. Unfortunately, there can be large degeneracies between an icy core, a water world and a rocky core hydrogen atmosphere; the mass and radius have strong overlap within these internal structure models [5, 22] (see Figure 1.2). Classifying internal structure from the distribution of bulk densities is the same technique that was used for asteroids, comets, satellites, and even planets, before technology improved enough to spectroscopically resolve more information from Solar System objects.

In analogy with planetary science – which historically observed disk integrated photometry, and later spectroscopy – our ability to gain increased quality of infor-

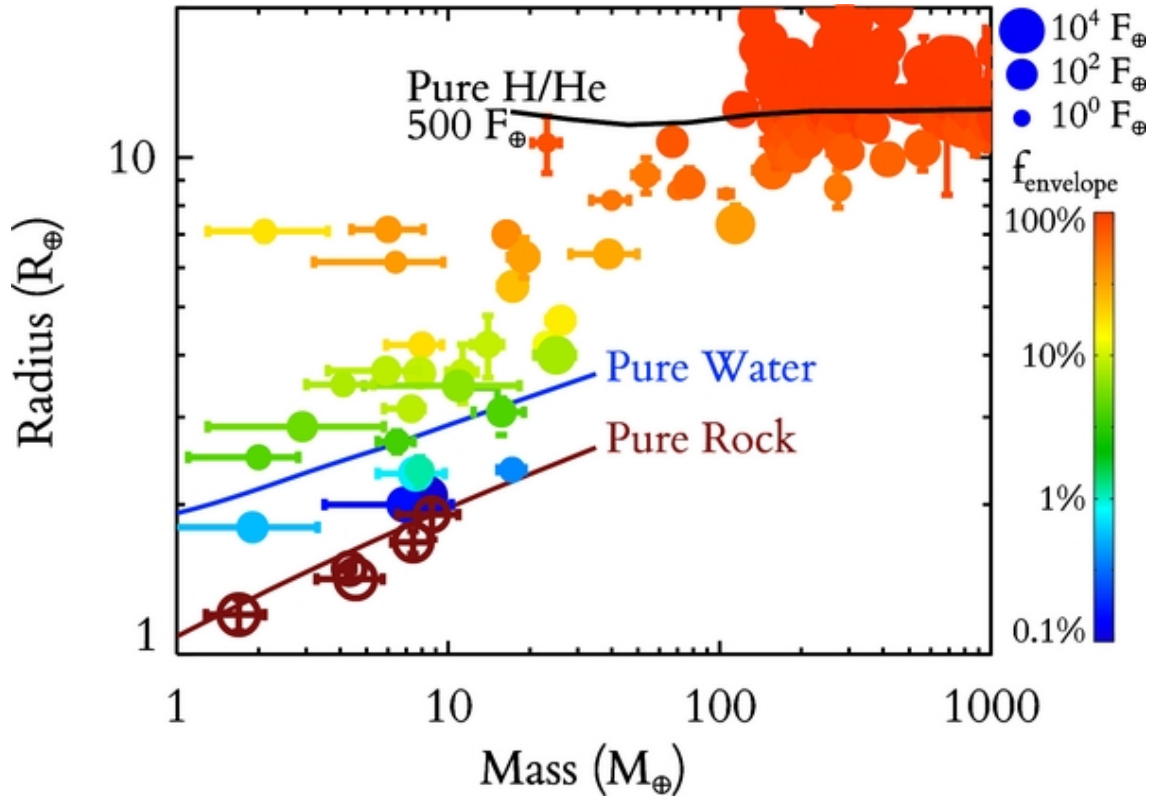


Figure 1.2: Lopez and Fortney 2014 plotted the mass and radius of 200 transiting exoplanets. The color is associated with the predicted hydrogen envelope fraction,  $f_{\text{envelope}}$  (inversely related to atmospheric metallicity), derived from internal structure models. The marker size corresponds to the stellar insolation with respect to the Earth,  $F_{\oplus}$ . They predict a strong correlation between hydrogen envelope fraction and planetary mass.

mation from the exoplanet atmospheres slowly developed with both technology and techniques. We developed observational modes starting from photometry to low resolution spectroscopy and, recently, to medium resolution spectroscopy; all of which is still disk integrated. Although modern telescopes are able to spatially resolve a large number of celestial bodies in the Solar System, the idea of spatially resolving an exoplanet is ostensibly well outside any expectations for future technology. That leaves our field on a necessary path to improve our ability to spectroscopically resolve disk-integrated spectra, known as emission and transmission spectroscopy (discussed below).

Four themes run through this thesis: spectroscopy, scale height, observability, and mitigating correlated noise sources. I will introduce each of these in the following subsections. Transmission spectroscopy is a technique to spectroscopically probe the atmospheres of exoplanets by measuring variations in the transmitted light as a function of wavelength,  $\frac{\delta D}{\delta \lambda}$ . Scale height is a key physical property that we study to characterise exoplanetary atmospheres, such as in transmission spectroscopy. The observability of a spectrum is strongly dependent on the scale height of the atmosphere, as well as its composition. Instrumental and other correlated noise sources interfere with our ability to interpret any signals from exoplanetary atmospheres. First in the next sections, then in the chapters to follow, I will detail both my work with each of these facets of exoplanet observations, as well as develop perspective for where and how my projects provide insight into exoplanet atmospheric science.

## 1.1 Transmission Spectroscopy

Transmission spectroscopy is a technique that observes the host star with a spectrometer as the exoplanet passes between our detectors and the star; we measure the planetary transit depth as a function of wavelength,  $\frac{\delta D}{\delta \lambda}$ . The transit depth varies with wavelength – in the case of a clear atmosphere – because the amount of light transmitted through the atmosphere depends on the molecules in the atmosphere absorbing or scattering that light; at the core molecular bands, the transmission spectrum peaks where the molecular line strength is largest because the transit depth (per wavelength) is a function of the optical depth (per wavelength; see below). This technique probes the absorption cross sections of molecules in the observed height range (usually within the upper atmosphere near the 1 mbar regime), as well as the scattering properties of molecules and particles that scatter the light away from our detectors.

The physics of transmission spectroscopy is to measure perturbations in the stellar radiation field as it passes through the optically thin portion of the exoplanetary atmosphere. The radiation field interacts with the molecules and particles suspended in the gas phase – integrated over its temperature and pressure profile –, resulting in absorption features in the transmitted spectrum. Neglecting the self-emission of the atmosphere, the equations of radiative transfer reduce to the Beer-Lambert Law, where the transit depth – the amount of light blocked from view,  $(\Delta I/I_o)$  – is related to the absorption cross section,  $\kappa_{i,\lambda}$ , times the gas density,  $\rho_i$ , per type of molecule, such that

$$\tau_\lambda = \sum_i \int_x \rho_i \kappa_{i,\lambda} dx \quad (1.2)$$

is the optical depth;  $x$  is the optical path length through the atmosphere. The transit depth, at a wavelength  $\lambda$ , can be shown to be  $(\Delta I/I_o)_\lambda = e^{-\tau_\lambda}$ . During a transit, the optical depth is enhanced – relative to radial emission – by a factor related to the square root of the planetary radius in scale heights (see Figure 1.3), which is the integrated path length of the chord through the terminator.

When the optical depth along the chord becomes  $\tau_\lambda \gg 1$ , the atmosphere is considered to be opaque; this occurs quickly for low to moderate impact parameters through the planetary atmosphere (see Figure 1.3), resulting in the measured transit depth. The impact parameter is the distance between the center of the planet and the chord that light travels through the atmosphere. The measured transit depth is the average amount of light blocked by the optically thick region of the planet. This regime is column density dominated, in that, even for a small absorption cross section,  $\kappa$ , the atmosphere would still appear opaque in the visible and infrared – where our detectors are tuned and the stellar signal is strong. But in the upper atmosphere, the column densities along the chord through the terminator of the planet are lower (see Figure 1.3). If the optical depth is small enough to allow some of the stellar light to pass through, then we consider the gas to be optically thin, and can measure spectral features in the signal. The specific amount of light absorbed by the atmosphere through this regime is dependent on both the column density and the molecular absorption cross section. The interplay between molecular absorption

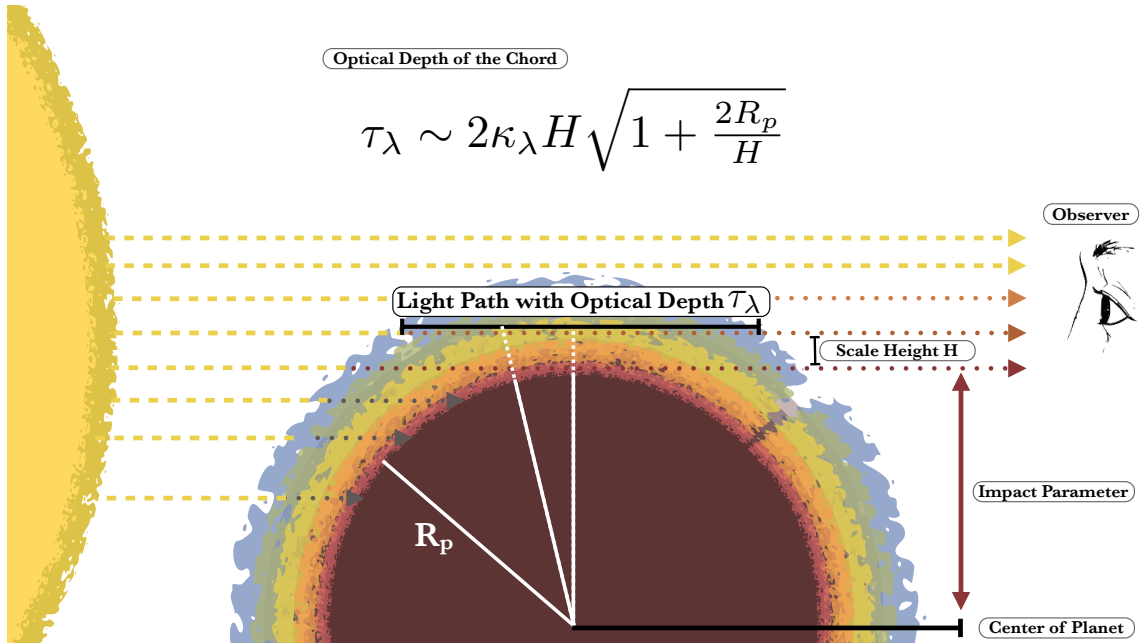


Figure 1.3: In the transit geometry, the optical depth is enhanced, relative to a radial (or emission) geometry, because the stellar light is passing through the exoplanetary atmosphere on a tangential chord. A transmission spectrum measures variations in the transit depth as a function of wavelength. The amount of stellar light absorbed by the exoplanet – as it passes through the planet’s atmosphere – is related to the optical depth – a function of the column density and absorption cross sections; most of the light is absorbed by the bulk mass of the planet, which defines the column density dominated regime (dark red). The “surface” of an exoplanet (light red) is interpreted as either the rock-atmosphere boundary (where one exists), the 1 mbar level (in the case of a clear atmosphere), or the cloud top pressure (in the case of a cloudy atmosphere). In the upper atmosphere, above the surface, the optical depth is more sensitive to the absorption cross section. At wavelengths near the cores of molecular features (e.g.  $1.41 \mu\text{m}$  for  $H_2O$ ) the transit depth is larger because more light is absorbed (blue), relative to wavelengths near the wings of molecular features (e.g.  $1.2 \text{ \& } 1.6 \mu\text{m}$  for  $H_2O$ ; light red).

bands and column density produces a spectroscopic signal that directly corresponds to the abundance of each type of molecule. Our detectors on Earth absorb the light from the host star and measure what light was transmitted through the planetary atmosphere.

## 1.2 Scale Height and Observability

Scale height is the dominant physical property that determines the significance of transmission spectra because it gives an estimate of the transit depth (or apparent “radius”) of the exoplanet. We can imagine the optically thin, upper atmosphere as consecutive slabs of gas, such that the higher pressures (lower altitudes) have larger column densities, absorbing more light (see above). For a strong absorber, such as methane at  $3.3\mu m$ , the atmosphere does not require a significant column density for the gas to become optically thick, resulting in an opaque atmosphere at lower pressures (higher altitudes) than in the wings of this methane feature; the transit depth would then be measured larger at the core of the  $3.3\mu m$  feature than at the wings. The amount of light absorbed increases for wavelengths near the centers of molecular features and decreases at the wings of these features. This effect causes the planetary transit depth to vary with wavelength, on the order of a few scale heights.

Scale height is the distance over which the pressure and density in the atmosphere are reduced by one e-folding: in the case of hydrostatic equilibrium,  $P(z) = P_0 e^{-(z-z_0)/H}$  and  $\rho(z) = \rho_0 e^{-(z-z_0)/H}$ , where  $H$  is the scale height,  $P$  is the

pressure, and  $\rho$  is the density; the latter of which are functions of the altitude,  $z - z_o$ . It can be shown that the scale height is a function of the mean molecular weight,  $\mu$ , the temperature,  $T$ , and local gravity,  $g(r)$  (where  $r$  is the radial distance from the center of mass);

$$H_p = \frac{k_b T}{\mu m_p g(r)}. \quad (1.3)$$

The physical constants  $k_b$  and  $m_p$  are the ‘‘Boltzmann constant’’ – which relates temperature to energy – and the mass of the proton – which normalizes the local atmospheric mass to units of atomic mass –, respectively.  $\mu$  is the mean molecular weight. And,  $g(r)$ , the local gravity field, can be measured as  $g(r) = \frac{GM(r)}{r^2}$ . If we assume that the upper atmosphere constitutes a small fraction of both the radius and mass of the planet, then we can simplify this expression into the following,

$$g_p = \frac{GM_p}{R_p^2}. \quad (1.4)$$

On the surface of the Earth,  $g_{\oplus} \sim 9.8 \text{ m/s}^2$  on average. In the upper atmosphere of Jupiter,  $g_{J_4} \sim 24.78 \text{ m/s}^2$ . Note that the scale height of the Earth is  $H_{\oplus} \sim 8.5 \text{ km}$ , while the scale height of Jupiter is  $H_{J_4} \sim 27 \text{ km}$ . For hot Jupiters – which have the most readily accessible atmospheres yet measured –, their scale heights are 100s of  $\text{km}$ . In the case of HD189733b and HD209458b – the two most studied hot Jupiters –, their scale heights are  $H_{189b} \sim 190 \text{ km}$  and  $H_{209b} \sim 534 \text{ km}$ , respectively. Therefore, the most accessibly exoplanet atmospheres are  $\sim 15 - 20$  times larger than our Jupiter and  $\sim 20 - 70x$  harder to observe our Earth, if they

were exoplanets. This shows the technological hurdle that we must overcome, to first order.

HST-WFC3, with scanning mode, is able to reach a precision on the order of  $\frac{1}{2}$  scale height. For example, the scale height for the atmosphere of HAT-P-11b is  $H_{\text{H11}} \sim 260$  km – with  $R_p \sim 28,000$  km and  $R_s \sim 478,100$  km –, this scale height produces a change in the transit depth of  $\sim 63$  ppm (see below); Fraine et al. (2014) [30] measured the spectroscopic signature for HAT-P-11b to a precision of  $\sim 45$  ppm with HST-WFC3, corresponding to a precision of 0.71 scale heights for HAT-P-11b. In the case of GJ 436 b, Knutson et al. (2014a) [19] also used HST-WFC3 to produce a precision of  $\sim 40$  ppm. Because GJ 436b has a scale height of  $H_{\text{GJ436b}} \sim 180$  km, the predicted significance of the transmission spectrum is  $\sim 101$  ppm; therefore, the 40 ppm precision is therefore 0.37 scale heights. In contrast, for hot Jupiters like HD189 and HD209, the precisions from McCullough et al. (2014) [32] and Deming et al. (2013) [33], respectively, is therefore 0.63 and 0.20 scale heights, respectively. I will show later that atmospheric, molecular features are being detected on the order of 2 - 4 scale heights. This is to say, our current technology is able to achieve 2 -  $5\sigma$  detections of molecules in the atmospheres of hot Jupiters. The precision in the transit depth measurements is dominated by the stellar flux (the more photons during transit, the better), as well as our ability to understand both stellar and detector effects throughout our observations; this will be covered in the sections below.

### 1.3 Thermochemical equilibrium and Disequilibrium Chemistry

Various modes of atmospheric physics in exoplanets can be explained as both thermochemical equilibrium and disequilibrium processes, which we constrain with our observations both directly and indirectly. For example, hot Jupiter atmospheres in thermochemical equilibrium, similar to Jupiter but much hotter, are expected to have significant scale heights, exhibiting prominent molecular absorption features that span up to  $\frac{\Delta D}{\Delta \lambda} \sim 5$  scale heights. This regime can be well understood by theoretical models that are extrapolated from our Solar System.

With many exoplanets, disequilibrium processes seem to significantly affect their atmospheres in ways that were unexpected with previous observational and theoretical understanding. From the first multi-wavelength observations of exoplanet atmospheres [28, 34–36], we began to uncover a lack of significant spectroscopic features, and even flat spectra, implying a completely opaque atmosphere [28, 36–38]. Theoretical models began to include disequilibrium chemistry in the interpretation of these results [16–18, 39]. Disequilibrium chemistry can be derived from many pathways, such as photochemistry, vertical mixing, or extreme atmospheric metallicities – relative to the Solar System.

If the atmosphere is in thermochemical equilibrium, then the many species of molecules can be sourced in situ – alongside other, non-traceable molecules, and also lighter (e.g. molecular hydrogen) molecules –, through collisions and chemical reactions. These are modeled by minimizing the Gibbs free energy and observationally constraining the temperature-pressure profile. To first order, we still expect

thermochemical equilibrium and compare our results to these models [9,10]. In several cases, “disequilibrium chemistry” is believed to play a significant role shaping the transmission and emission spectra of exoplanets [8,18,39]. In most spectroscopically resolved transmission spectra to date, the significance of the spectroscopic detections are on the order of fractions of scale heights, and smaller than thermochemical equilibrium predictions [30,33,34,40].

In all three major signatures of disequilibrium chemistry – clouds, haze, high mean molecular weight – , the observational result is to flatten the transmission and emission spectra – resulting in the suppression of absorption features. In the case of photochemical production of haze particles in the upper atmosphere, the transmission spectrum is flattened because haze scatters light away from the line of sight to the observer, removing the lower portions of the spectrum, and possibly creating an opaque atmosphere [26,27,36,40,42,43]. With vertical mixing, molecules from deeper in the atmosphere are lifted to pressures much lower than where they are being created. This process catalyses extra chains of chemical reactions in the upper atmosphere that can produce both molecular signatures from molecules out of equilibrium [18,44], as well as cloud layers that make the atmosphere opaque, similar to the haze models [17,18]. When atmospheric metallicities are orders of magnitude larger than Solar, the reactions rates and collisional probabilities are enhanced. This could produce cloud layers that would obscure the atmosphere [18,19,39] because the condensation curves for each molecule are shifted to higher altitudes. The primary effect of increasing the atmospheric metallicity is to decrease the scale height and increase the column density. Both situations – a cloud layer or small scale height –

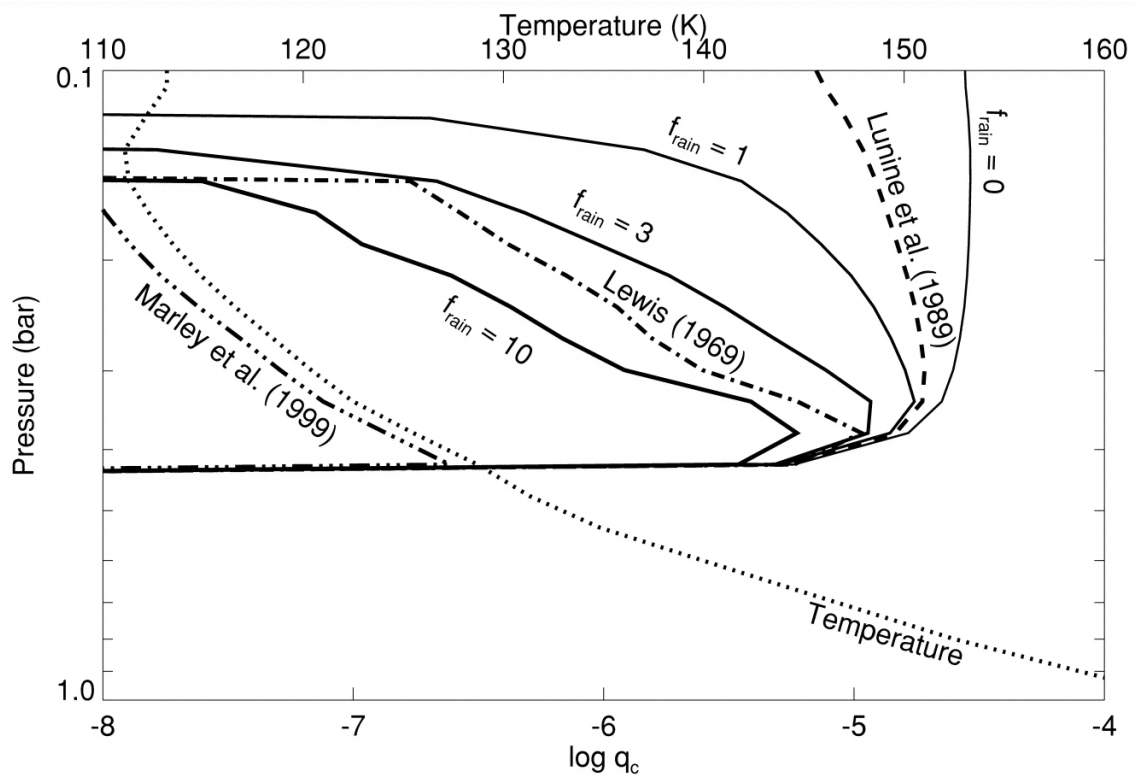


Figure 1.4: Ackerman et al. (2001) [41] show the vertical profiles of mixing ratio by volume of condensed ammonia from their model of Jupiter's ammonia cloud with different values  $f_{sed}$  ( $f_{rain}$  in this figure) and from their adaptations of other models as labeled. The y-axis shows the pressure levels and the x-axis shows the mixing ratio of ammonia. The dotted line is the temperature profile. The kinks in the condensate profiles are caused by ripples in the temperature profile. The cloud bottom pressure is calculated as the intersection of the temperature-pressure profile and the condensation curve for ammonia. For all values of  $f_{rain}$ , the cloud bottom pressure remains the same; but if  $f_{rain}$  is larger, then the cloud top pressure is also larger (lower altitude); this implies puffier clouds for lighter particles. (Adapted from Ackerman et al. (2001) [41])

increase the optical depth of the atmosphere in the observational regime.

This means that disequilibrium chemistry can sustain observable molecules in the detectable regime – outside of the abundance predicted by thermochemical equilibrium – but it can also sustain opaque clouds and haze layers that minimize any possible signals for us to measure from these atmospheres [17, 19, 39]. In recent studies, it was found that high altitude clouds are very likely the cause of an opaque atmosphere, out to  $5 \mu m$ , on the transiting exoplanet GJ 1214 b [17, 28, 36–38, 45]. The observational signature in the infrared for clouds or hazes – a flat spectrum – is indistinguishable within the measured uncertainties. As such, we largely refer to all flat spectra as “cloudy”, but it should be understood that this is a semantic simplification because hazes or clouds are equally likely to explain the IR observations. These models diverge in the optical regime; however the results are less robust because the data are less precise [17, 36, 46].

When observing spectroscopic signatures of molecules in the atmospheres of exoplanets, we expect to find large variations in the transit depth as a function of wavelength, with  $\frac{\delta D}{\delta \lambda} \sim 5$  scale heights. In practice, we attain  $\frac{\delta D}{\delta \lambda} \sim 2$  scale heights; in the case of the flat spectrum  $\frac{\delta D}{\delta \lambda} \sim 0$  scale heights. The change in the transit depth is directly related to the scale height through the observable annulus as

$$\frac{\delta D}{\delta \lambda} = 2 \left( \frac{H_p}{R_s} \right) \left( \frac{R_p}{R_s} \right) e^{-\tau_\lambda}. \quad (1.5)$$

Theoretical explanations for observing less significant spectral features than we were expecting take place on two fronts. The first is to compare the observations

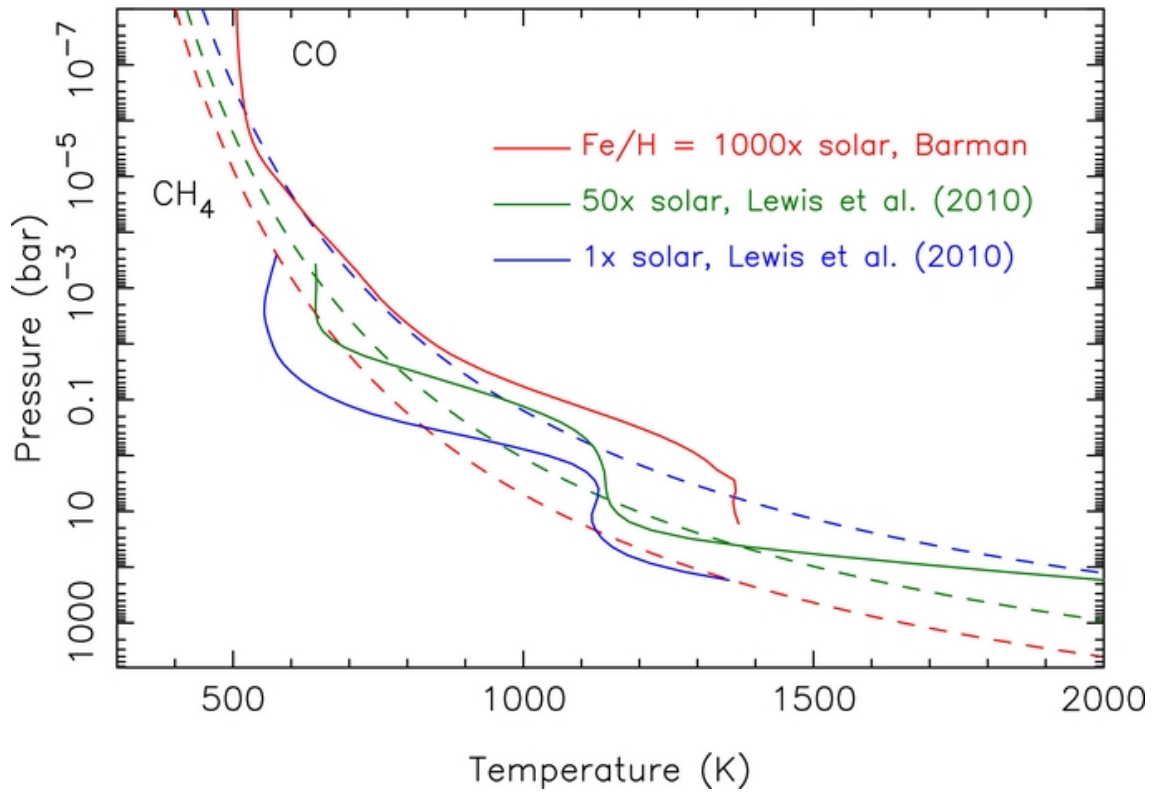


Figure 1.5: Moses et al. (2013) [18] illustrated how an increase in atmospheric metallicity would effect the temperature-pressure profiles of the exoplanet GJ 436 b. The solid colored curves represent the theoretical temperature-pressure profiles as a function of atmospheric metallicity. The dashed curves represent the boundaries where  $CO$  and  $CH_4$  have equal abundances in thermochemical equilibrium. As the metallicity is increased, the temperature becomes higher at smaller pressures (moves to the right), while the  $CO$ - $CH_4$  equilibrium curves move to the left, which would allow more  $CO$  than  $CH_4$  in the large and extreme metallicity examples. (Adapted from Moses et al. (2013) [18])

to theoretical models that include high mean molecular weights, high altitude clouds layers, or high altitude haze layers. The second is to computationally simulate either 1D chemistry models (see Figure 1.4) or 2D/3D fluid models of an atmosphere to understand the effects of extreme conditions on the atmospheric kinematics and radiative transfer; both of these model categories tend to parameterize cloud physics – introduce nominal values derived from experiments or other simulations [47]. Some simulations focus on cloud formation by generating models to explain the observations using micro-physics cloud / haze generation models (see Figure 1.5); these models tend to parameterize the fluid dynamics [17].

In the case of fitting the data – which we call “retrievals” –, the models are tuned to match the data because they iteratively achieve that goal using several techniques rooted in Bayesian analysis (i.e. Markov Chain Monte Carlo and nested sampling). This is very similar to generalized model fitting, but with the specialized setting of Gibbs minimization (for thermochemical equilibrium) and a vast lookup table of reaction rates (see Figure 1.6). To invoke disequilibrium processes, these models add observational effects – instead of modeling them directly –, such as a flattening of the bottom of the transmission spectrum to mimic a cloud top pressure within the observational regime that truncates the molecular features by forcing the cloud layer to be opaque. Similarly, retrievals introduce haze layers by enforcing a power law increase in the transit depth that is inversely correlated with wavelength – for either Mie ( $\sim \lambda^{-1}$ ) or Rayleigh ( $\sim \lambda^{-4}$ ) scattering.

To enhance the atmospheric metallicity, transmission spectral retrievals reduce the molecular features. The reduction in scale height reduces the overall span be-

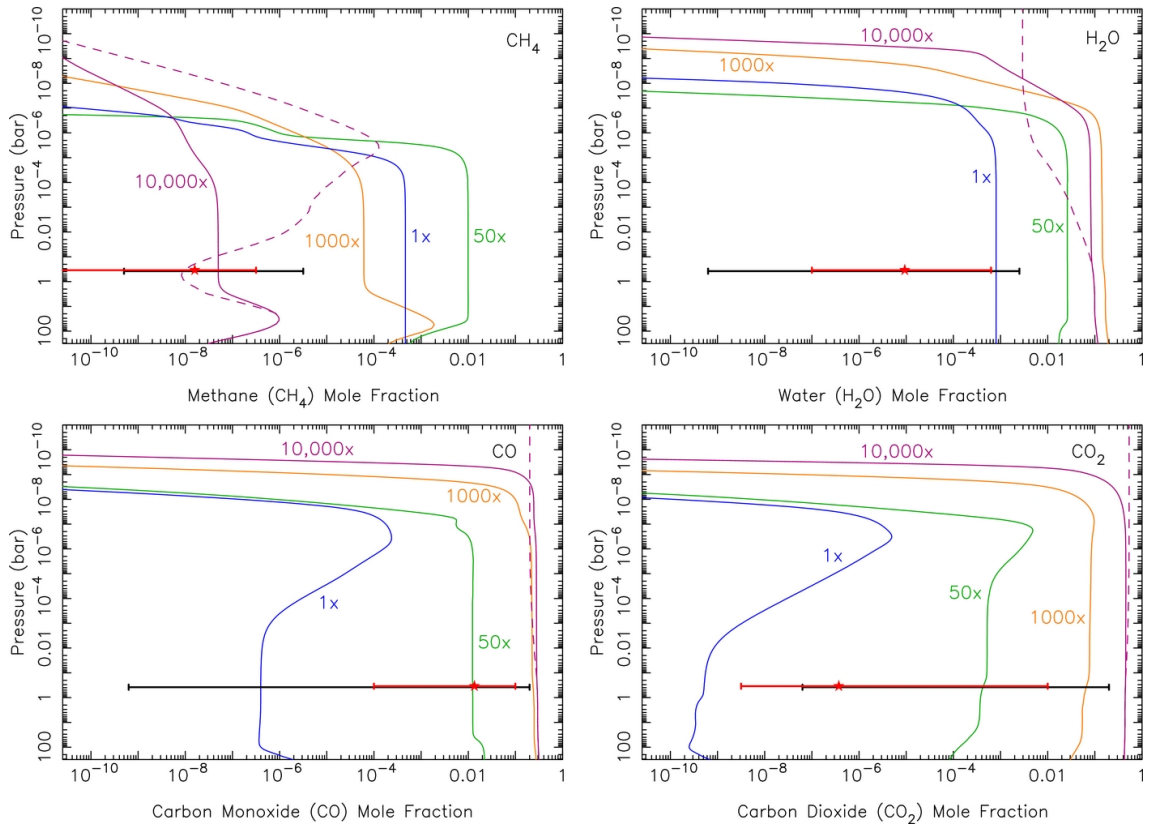


Figure 1.6: A comparison from Moses et al. (2013) [18] of the mixing ratios for significant molecular species as a function of atmospheric metallicity, using their kinetics/transport models to study GJ 436 b – a well studied warm Neptune at  $4.3 R_{\oplus}$  and  $22 M_{\oplus}$ . The y-axis shows the pressure; the x-axis shows the mixing ratios. With an assumed temperature-pressure profile and a Solar C/O ratio, Moses et al. (2013) [18] show how an increase in atmospheric metallicity will remove methane from the atmosphere, but add water, carbon monoxide, and carbon dioxide well above Solar metallicity predicted levels. This is a definitive illustration of how exoplanet atmospheric studies push atmospheric physics into new regimes to explain the extreme solar systems that we are discovering and characterising. (Adapted from Moses et al. (2013) [18])

tween the minimum to maximum of the absorption feature in the spectrum, which acts to “weigh down” the atmosphere. From the above physical interpretation, an increased atmospheric metallicity directly increases the column density, and thus increases the optical depth throughout the observable regime. Equation 1.2 shows that increasing the atmospheric metallicity (increasing the mean molecular weight) reduces scale height, which reduces the observational signature.

In the forward modeling case – either through fluid dynamical models or physically driven cloud / haze production –, we must invoke a set of reaction rates in the atmosphere corresponding to the thermochemical condensation or photochemical particulate production. The former is similar to parameterizing moist convection in an atmosphere by adding sedimentation terms to the calculation of temperature-pressure profiles [8, 17], which then produce self-consistent models for cloud formation as the intersection of the Clausius-Clapeyron relation for condensation in a hydrostatic atmosphere with the temperature-pressure profiles [17, 48, 49]. At the intersection of these curves, cloud bottoms are predicted to occur. The cloud tops are then determined by the sedimentation factor,  $f_{sed}$ , which is a relationship between the atmospheric upwelling and the relative atmospheric weight of the particles.  $f_{sed}$  becomes a driving force in the cloud top pressure because light particles are driven further upwards than heavier particles, producing a smaller or larger cloud top pressure spanning our observational regime above 1 mbar [8, 10, 17, 43, 50].

Forward modeling has a long and important history with both Solar System bodies and exoplanets [8, 51, 52]. Its use for both predicting atmospheric physics and interpreting observational results encourages strong collaborations between theoret-

ical and observational teams [5]. Observations of exoplanets have always pushed the envelope of expected physical parameters for what we expect to discover. From the first days of hot Jupiter radial velocity detections, to the thousands of super Earths and mini-Neptunes in the Kepler data, exoplanet discoveries have revealed the true diversity of planet formation [14, 25, 34, 53–56]. Similarly, exoplanet spectroscopy has revealed the diversity of atmospheric physics and improved our understanding of thermochemical evolution, extreme metallicity regimes, metal-rich cloud production, and the efficiency of photochemical processes [19, 30, 45].

Particularly in the case of metallicities and cloud production, the recent discovery of several significantly flat spectra on small exoplanets has provided a testbed for conditions resulting in extreme solar systems. In the case of GJ 1214 b, the observations conclude in favor of a cloud layer above 1 mbar, possibly 1  $\mu\text{bar}$  [17, 28, 36–38, 45], that is opaque to all wavelengths of light from 0.4 – 5.0  $\mu\text{m}$  [36, 45]. Forward models of cloud production show that the constituents of such a cloud – in thermochemical equilibrium – may be metal rich, such as *ZnS* or *KCl* [17, 49, 50]. In Chapter 2, I will show that these models are ruled out by our team’s results with  $\sim 40$  ppm uncertainty at 4.5  $\mu\text{m}$  [30]. On the other hand, the observational results for GJ 436 b concluded in favor of either high altitude cloud layers or atmospheric metallicities as large as 2000x Solar composition [10, 19]; the latter provide simultaneous explanations for both the flat transmission spectrum and CO rich emission spectrum observed from this planet [16, 18, 39, 57].

## 1.4 Correlated Noise Sources: Astrophysical and Instrumental Noise

Almost all exoplanet observations are differential measurements. This means that we compare the light from the system during the transit or eclipse with the light from the system before and after the transit or eclipse. This allows us to characterize and remove the variations in the stellar flux, and instrumental response, in detail. We investigate correlations in the measured flux with stellar and instrumental effects to remove them from the star + instrument + planet system observations [36–38, 58–60]. With photometric observations, as is done with all transiting planet detection methods, the time dependent flux from the star is modeled using a variety of polynomials or similar analytic functions. On the time scale of the planetary orbit, these signals are usually small perturbations. If a star has short period oscillations, it is not likely to be a high-quality target for follow-up characterisations, especially with spectroscopic measurements. As a result, we include baseline models with long period perturbations (i.e. polynomials) to account for stellar variations during our transit observations. In the case of the Kepler mission [30, 61], we isolated only the phase range in the 4-year light curve that was associated with the planetary transit and applied individual, long period perturbation models (straight lines) to the baseline.

For instrumental effects, there are several different modes that must be accounted for in each telescope-instrument-wavelength coupling. The four primary instruments that I have used are Spitzer-IRAC (3.6 & 4.5  $\mu m$ ), Hubble-WFC3 (1.1 - 1.7  $\mu m$ ), Kepler (0.6  $\mu m$ ), Magellan-IMACS (0.4 - 0.8  $\mu m$ ). Each instrument has

very different behaviour. Spitzer-IRAC has the most well known, and diverse, instrumental noise sources, called the “intrapixel effect”. The flux varies as a function of position on the detector [36,54,58,62,63], parameterized by the (y,x)-positions derived from various centering techniques. Physically, the photons are being absorbed by the InSb (indium antimonide) crystalline structure inside the pixel at a variable efficiency depending on the precise position of the photon across the pixel. This induces both short ( $< 1$  hour) and long ( $> 1$  hour) period oscillations in the flux, which we call the “sawtooth pattern” [58,62–64]. It is essential to model these perturbations with a systematic and mathematically well-defined method, because our signal – the transit or eclipse – has the same or less order of magnitude to both the white and red noise sources. Especially in the case of eclipse observations, the signal can usually only be seen in the cleaned and binned data. As I will demonstrate in Chapter 4, there is a definite lower limit to the detectability of eclipse observations with Spitzer data, as a function of stellar flux received.

With the HST-WFC3, the main source of correlated noise is related to excess electrons left on the detector after subsequent readouts. The detector is meant to have the voltages reset and excess electrons removed from the detector between each observation. But, because of small amounts of charge left on the detector, there is an exponential increase,  $1 - ae^{-bt}$ , in the flux read out from successive integrations [30,33,38,65]. For each transit, the buffer must be fully dumped when the satellite orbits behind the Earth, as seen from the target. This allows the detector to be “reset to zero” such that we can model the effect of this buffer excess both before, during, and after the transit. Modeling the rise in flux read

out by the detector is necessary to properly estimate the average, physical transit depth, but not to ascertain the spectroscopic features [30, 32, 33, 38]. Spectroscopic measurements are made by comparing individual wavelengths to the integral over the entire bandpass, so they are less sensitive to the detector anomalies [19, 33, 48].

Each instrument has its own unique set of instrumental effects that have varying degrees of significance to decorrelate. The baseline technique for all of these instruments is to use a Markov-Chain Monte Carlo (MCMC) [11, 36, 54, 60, 66–68], with a set of model parameters or non-parameterized models with hyper-parameters [60, 68]; examples include the intrapixel effect with the Spitzer-IRAC observations [58], the bounded exponential for HST-WFC3 data [33], a three-month long rise and fall with temperature in Kepler time-series [56, 69], or a wavelength-dependent variation with atmospheric mass as a function of time over the Magellan-IMACS observations. I will discuss the significance, influence, and characterization techniques used for each of these systematic effects in the relevant section along side data that I have used in the pursuit of exoplanet science.

## 1.5 Thesis Organisation

Chapter 2 will discuss the use of the Spitzer Space Telescope and the IRAC instrument, focusing on the 3.6 & 4.5  $\mu m$  wavelengths for GJ 1214 b. It will conclude with a discussion on the scientific interpretation of flat spectra in the Super-Earth regime. This topic will lead naturally into the expansion of theoretical models for opaque exoplanet atmospheres that may be able to explain these flat spectra.

Chapter 3 will discuss the application of Hubble Space Telescope Wide Field

Camera 3 to measure the transmission spectrum of a Neptune-sized exoplanet, HAT-P-11b. I will also include a discussion on the use of Kepler data for orbital constraints and stellar atmospheric characterisation. Chapter 3 will also include a discussion about the difficulties in combining observations and interpreting planet formation metrics – such as metallicity and C/O trends over a range of planetary mass – from those combined measurements.

Chapter 4 will discuss non-detections of eclipse measurements using Spitzer-IRAC to measure the temperature of HAT-P-11b. Our goal was to characterise the exoplanet’s energy budget – for the temperature-pressure profile –, to more robustly interpret the spectroscopic data from Chapter 3. Chapter 4 will conclude with a discussion about the current techniques used to mitigate instrumental noise from Spitzer-IRAC. This discussion about the limitations of using the Spitzer-IRAC instrument to constrain emission spectra will lead to how future technology (i.e. James Webb Space Telescope-NIRCam) should greatly improve our understanding of exoplanet emission spectroscopy.

Chapter 5 will examine our ground based campaign using Magellan to characterise exoplanets using optical transmission spectra. We will look closely at the preliminary results for WASP-4b using Magellan from 400 - 800 nm. In Chapter 6, I will discuss the current technologies and techniques for ground-based, spectroscopic measurements, laying a framework for the importance of spectroscopic surveys at both optical and IR wavelengths. Finally, I will conclude by discussing how exoplanet atmospheres provide increased knowledge of planet formation and the discovery of the unknown.

## Chapter 2: Infrared Transmission Spectroscopy of a Super-Earth

### Abstract

We observed the transiting super-Earth exoplanet GJ1214b using Warm Spitzer at 4.5  $\mu\text{m}$  wavelength during a 20-day quasi-continuous sequence in May 2011. The goals of our long observation were to accurately define the infrared transit radius of this nearby super-Earth, to search for the secondary eclipse, and to search for other transiting planets in the habitable zone of GJ1214. We here report results from the transit monitoring of GJ1214b, including a re-analysis of previous transit observations by Désert et al (2011) [37]. In total, we analyse 14 transits of GJ1214b at 4.5  $\mu\text{m}$ , 3 transits at 3.6  $\mu\text{m}$ , and 7 new ground-based transits in the I+z band. Our new Spitzer data by themselves eliminate cloudless solar composition atmospheres for GJ1214b, and methane-rich models from Howe & Burrows (2012) [70]. Using our new Spitzer measurements to anchor the observed transit radii of GJ1214b at long wavelengths, and adding new measurements in I+z, we evaluate models from Benneek & Seager (2012) [9] and Howe & Burrows (2012) [70] using a  $\chi^2$  analysis. We find that the best-fit model exhibits an increase in transit radius at short wavelengths due to Rayleigh scattering. Pure water atmospheres are also possible. However, a flat line (no atmosphere detected) remains among the best of the statis-

tically acceptable models, and better than pure water atmospheres. We explore the effect of systematic differences among results from different observational groups, and we find that the Howe & Burrows (2012) [70] tholin-haze model remains the best fit, even when systematic differences among observers are considered.

## 2.1 Introduction

Detecting molecular abundances, temperature pressure profiles, and atmospheric metallicity from a population of super-Earths would provide constraints on the bulk distribution of planet formation in our galaxy. The Kepler mission provided robust constraints on the distribution of planets that formed nearby our own Solar System [55, 56]. Kepler revealed that small planets ( $R_p < 4R_\oplus$ ) comprise  $\sim 80\%$  of the debiased planetary population [60, 71–73]. To understand the end results of planet formation, we must constrain the physical properties of this population of planets. Unfortunately, the bulk densities of small planets are strongly degenerate between internal structure models that can produce hydrogen dominated planets with rocky cores, or hydrogen poor planets with volatile rich cores [22]. To distinguish between these models, we must spectroscopically detect molecules in the exoplanetary atmospheres, which can constrain the mean molecular weight,  $\mu$  [42]. The mean molecular weight,  $\mu$ , is directly related to the transmission spectrum,  $\Delta D_\lambda$ , through the scale height [42]:

$$\Delta D_\lambda = \epsilon_\lambda \frac{2HR_p}{R_s^2} = \alpha_\lambda H = \alpha_\lambda \frac{kT}{\mu g} \quad (2.1)$$

$$\mu = \alpha_\lambda \frac{kT}{g} (\Delta D_\lambda)^{-1}$$

(i.e. if  $\mu$  is small, then the atmosphere is likely to be hydrogen-rich). Here  $\epsilon_\lambda$  is directly proportional to the molecular absorption strength over wavelength. If we can estimate or constrain the atmospheric temperature profile and spectroscopically detect a molecular feature, then we are able to constrain the mean molecular weight from the atmospheric scale height.

$\epsilon_\lambda$  represents the number of scale heights over which the atmosphere is opaque because the atmospheric absorption cross sections peak at that wavelength. [74] theoretically predicted that the average extent of the spectral feature is  $\langle \epsilon_\lambda \rangle \sim 5$  for a hydrogen dominated, clear atmosphere. Empirically, we have measured  $\langle \epsilon_\lambda \rangle \sim 2$  for most exoplanet atmospheres [33, 75].

It is important to detect molecules on small planets, but not many small planets are amenable to our observations with our current technology. The mass, radius, temperature, and scale height of the exoplanet, as well as the apparent magnitude and radius of its host star, are critical in determining if an exoplanetary atmosphere can be spectroscopically probed. Because super-Earths are small planets, we look for them around small stars, such that their  $\Delta D$  is amenable to the sensitivity of our detectors.

The mass and radius of the nearby transiting super-Earth GJ1214b [25] imply that it must have a significant atmosphere [22]. That inference motivated an extensive effort to detect the atmosphere, by seeking wavelength variations of the

transit depth. A wide variety of compositions are possible for super-Earth atmospheres [9, 70, 76], from hydrogen-dominated to heavy-element-rich. Most current observations of the transits [28, 37, 38, 77–80] have rejected hydrogen-dominated atmospheres for GJ1214b, but Croll et al. (2011) [81] concluded in favor of a low molecular weight atmosphere. The infrared (IR) spectral region is particularly important for such studies, because strong water vapor bands increase the transit depth in the IR significantly as compared to the optical. This is especially true for hydrogen-dominated atmospheres, because of the increased atmospheric scale height. The intrinsically strong IR water vapor opacity makes hydrogen-dominated atmospheres opaque in the IR over several scale heights, in spite of their relative paucity of heavy elements. Also, strong bands of methane and carbon monoxide fall within the Warm Spitzer bandpasses at 3.6- and 4.5  $\mu\text{m}$ , respectively. Considering that GJ1214b’s M-dwarf host star is bright in the IR, transit observations of GJ1214b using Warm Spitzer become particularly relevant to the characterization of its atmosphere.

In May 2011, we observed the GJ1214 system quasi-continuously for 20 days, using Spitzer’s IRAC instrument at 4.5  $\mu\text{m}$ . Our investigation had three goals: 1) to improve the transit parameters of the system and constrain the properties of the planet’s transmission spectrum, 2) to search for the secondary eclipse, and 3) to search for other transiting planets in this system, to the outer edge of the habitable zone.

Our observations included minor interruptions for data downloads. But, an unplanned 42-hour data loss also occurred during the 20-day sequence, caused by a

combination of spacecraft and Deep Space Network (DSN) downlink anomalies. We therefore re-observed GJ1214 for an additional 42-hours in November, 2011, using the IRAC 3.6  $\mu\text{m}$  band. Consequently, we have multiple transits at both Warm Spitzer wavelengths, and these data provide a particularly powerful constraint on the IR transit depth. Moreover, since our 4.5  $\mu\text{m}$  transits were observed nearly consecutively, we have an excellent basis for evaluating the degree to which stellar activity (e.g., star spots) affect the inferred transit depth.

In this chapter, we focus on the implications of our observations for understanding the nature of GJ1214b's atmosphere, and we investigate the wavelength-dependent transit radius of GJ1214b in detail. Our analysis includes the degree to which star spots - even those not occulted by the planet - contribute to possible bias in the measured radius of the planet. Anchored by our improved precision for these infrared transits of GJ1214b, we add 7 new ground-based transits in the I+z band, and we re-analyze the totality of published wavelength-dependent transit depths for GJ1214b, exploiting recent advances in super-Earth model atmospheres [9, 70].

Sec. 2 describes the details of our observations, and Sec. 3 explains our procedure to extract precise photometry from the data. In Sec. 4 we fit to the photometry, extracting the transit radius for the planet in the warm Spitzer and I+z bands, and we derive improved system parameters. Sec. 5 considers the possible effect of star spots on our results. Sec. 6 discusses implications for the atmosphere of GJ1214b.

## 2.2 Observations

### 2.2.1 Spitzer

We observed GJ1214 for 20 consecutive days using Warm Spitzer at  $4.5\ \mu\text{m}$ , beginning on April 29, 2011 at 03-46 UTC. We used subarray mode with an exposure time of 2 seconds per frame. The observations contain several  $\sim 3$ -hour interruptions for data download, and one unanticipated 42-hour gap where data were irretrievably lost. The data loss occurred because the DSN incurred anomalous delays in downloading data at that time. When the Spitzer observatory was designed, long observing campaigns of exoplanet photometry were not envisioned. Spitzer's onboard flight software was designed to automatically delete data after a certain period of time, to make room in memory for new observations. The DSN anomaly consequently caused the onboard software to delete data before downlink (the flight software has now been corrected so that this will not recur).

To compensate for the data loss, we were awarded 42 hours of continuous observations that began on November 6, 2011, at 11-54 UTC. We elected to acquire these data in Spitzer's  $3.6\ \mu\text{m}$  bandpass, to complement the  $4.5\ \mu\text{m}$  data from May 2011. We again used 2-second exposure times in subarray mode. In total, our data comprise 791,808 exposures at  $4.5\ \mu\text{m}$ , and 74,624 exposures at  $3.6\ \mu\text{m}$ .

## 2.2.2 TRAPPIST

In order to help define the possible effects of stellar activity on the Spitzer transits, to further cross-check our analysis versus Gillon et al. (2012) [82], and to add additional information relevant to the atmosphere of GJ1214b, we observed 7 transits using the TRAPPIST facility [83,84], over the period 2011 March 11 - May 18. The TRAPPIST observations and photometry are described by Gillon et al. (2012) [82], but we summarize the data here. The observations were made using the 60-cm robotic telescope in a slightly defocused mode. An I+z filter gave transmission from 750 to 1100 nm. Differential photometry on the 25-sec exposure images was done (by M.G.) using IRAF/DAOPHOT. In our analysis, we use the same version of the photometry as Gillon et al. (2012) [82], but we perform an independent analysis and transit fitting.

## 2.3 Spitzer Photometry

### 2.3.1 Aperture Photometry

Our analysis utilizes the Basic Calibrated Data (BCD) files produced by version S18.18.0 of the Spitzer pipeline. Two dimensional (2D) Gaussian centering produces the least scatter in our final photometry [44,85]. Knutson et al. (2012) [86] found that flux-weighted centering gives superior results for Spitzer data in studies of exoplanetary phase curves over long time scales. We tried flux-weighted centering for our transit analysis, but it did not result in significant improvement over our 2D

Gaussian centering.

In the case of the 4.5  $\mu\text{m}$  photometry we center a circular aperture of constant radius on the star. We calculate the stellar flux within the aperture, including analytic approximations for the partial coverage of pixels at the boundary of the aperture. We vary the radius of the aperture from 2.0 to 5.0 pixels, in 0.5-pixel increments, and thereby produce seven versions of the photometry at each wavelength. After decorrelation (see below), we chose to use an aperture radius of 2.5 pixels for 4.5  $\mu\text{m}$ , based on the global scatter in the decorrelated photometry.

In the case of the 3.6  $\mu\text{m}$  photometry, we examined constant radius photometry— for the same seven radii as in the 4.5  $\mu\text{m}$  section— and variable radius aperture photometry. The variable radius photometry improves the precision by 41% over constant aperture photometry by varying the aperture radius as a function of the ‘noise-pixel’ calculations per frame [63, 86, 87]. Therefore we adopt the noise pixel method for our 3.6  $\mu\text{m}$  photometry, and subsequent intra-pixel decorrelation (see below).

The noise pixel method estimates the effective width of the pixel response function, accounting for undersampling, by calculating the variance of the flux per frame, weighted by the square of the mean flux:

$$\tilde{\beta}_i = \frac{(\sum I_j)^2}{\sum (I_j)^2}, \quad (2.2)$$

where  $\tilde{\beta}_i$  is the noise pixel parameter for the stellar image in frame  $i$ ,  $I_j$  is the intensity of pixel  $j$ , and the summations extend over all pixels wherein the

stellar intensity is significant. Using the  $\sqrt{\tilde{\beta}_i}$  as the aperture radius collects an optimum amount of light for photometry. The average aperture radius from using this formulation on our 3.6  $\mu\text{m}$  data is 2.60 pixels.

### 2.3.2 Decorrelation

Upon producing photometry, we immediately see Spitzer’s well-known intra-pixel sensitivity effect, that must be decorrelated and removed from the data. A portion of the raw 4.5  $\mu\text{m}$  photometry (before decorrelation) is illustrated in Figure 2.1. Because the transits of GJ1214b are substantially larger than the intra-pixel signature, we first mask off the transits from the first stage of decorrelation. Our 4.5  $\mu\text{m}$  data comprise seven distinct re-acquisitions of GJ1214, with interruptions for data download. Therefore our first stage of decorrelation is done separately for each of the seven re-acquisitions. That initial decorrelation fits two polynomials to the data for each re-acquisition. (There are seven sections of the data defined by the data downloads and re-acquisitions.) One polynomial fit is applied to those data points wherein the image centroid lies at Y-coordinate greater than the center of the pixel, and another polynomial fit is applied to those data wherein the image lies at Y-coordinate less than the center of the pixel. Our rationale for this two-parameter fit is based on visual inspection of the photometry, that shows different behavior above the center-of-pixel than below center (see lower panel of Figure 2.1). The polynomials are fourth order in Y and second order in X, because the photometric variations as a function of Y are more pronounced than with X. Also, visual

examination of the variation with Y indicated that lower order polynomials (e.g., quadratic) would not represent the variations optimally. After finding the best fit polynomials, we divide them into the data, including the in-transit data. We only used this step to determine initial conditions for an iterative weighting function method (see below).

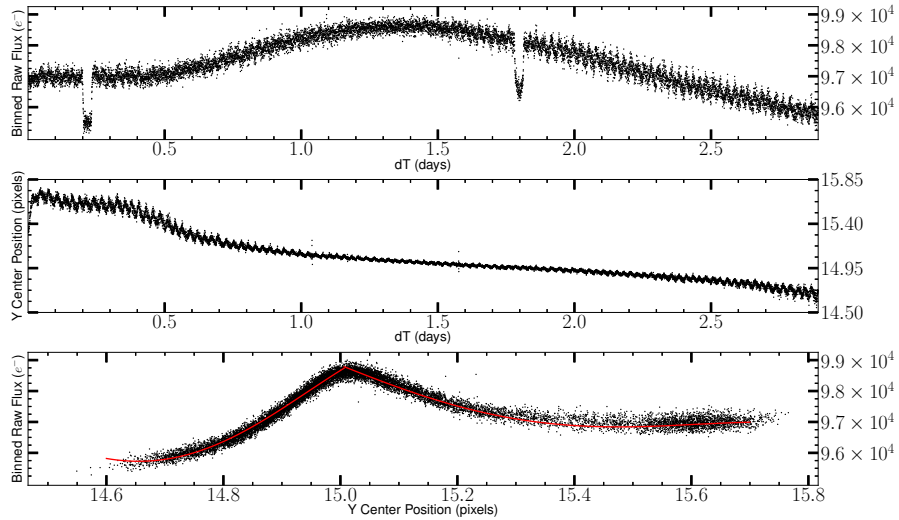


Figure 2.1: The top panel illustrates raw data for the first 2.9-day portion of our  $4.5 \mu\text{m}$  photometry, containing two transits. Each data point is aperture photometry before decorrelation, binned by every 10 data points. The middle panel shows the Y-center position as a function time; that which we correlate with the flux to remove the intra-pixel effect, and related systematic noise sources. The lower panel shows the same photometric values, except with the transit regions excluded, plotted versus the Y-pixel position of the stellar image. Note the different spatial dependence of the photometry on each side of pixel center. The red curves are the 4th order polynomial fits that we use to initiate the decorrelation process (see text).

We follow the polynomial decorrelation with a second procedure that is itself a two-pass iterative process. We first remove a preliminary transit model from the

polynomial-decorrelated data, and apply a Gaussian weighting function [62, 63, 86] to correct the intra-pixel signatures.

The kernel of the Gaussian weighting uses a  $\sigma$  of 0.005 pixels in Y, and 0.01 pixels in X for the 4.5  $\mu\text{m}$  data, that we determined by trial and error - evaluating the noise level of the final decorrelated photometry. A separate Gaussian weighting was applied to each section of the data between downloads, but the same kernel size was used for all data sections at 4.5  $\mu\text{m}$ .

For the 3.6  $\mu\text{m}$  data, we applied a noise-pixel, Gaussian weighting function that uses a variable  $\sigma$  in Y, X, and  $\tilde{\beta}$  (noise-pixel value). This varied the weights in the Gaussian kernel to accommodate the necessary number of neighboring points that influence the strength of the correlation between center position and flux, as discussed in Lewist et al. (2013) [63] and Knutson et al (2012) [86].

Because of effects near the pixel boundary, we chose to subdivide the 3.6  $\mu\text{m}$  data into 2 sections, encompassing the 2 transits in the data. The pixel boundary effects occurred well out of phase of both transits. After examining the global scatter and  $\sigma$  vs.  $N^{-0.5}$  (bin size) slope residuals, we found that decorrelating after subdividing the 3.6  $\mu\text{m}$  data set to within  $\pm 0.05$  of each transit produced the best noise levels, and resulted in more conservative uncertainty estimates on the transit parameters, by  $\sim 10\%$ . Moreover, this phase range coincides with similar subdivisions in the 4.5  $\mu\text{m}$  data.

After dividing by the results of the Gaussian weighting, we solve for and subtract an improved transit model, and again apply a second stage weighting function decorrelation. We experimented with a third iteration of this process, but it did not

produce significant improvement. Unlike the first (polynomial) stage of decorrelation, the Gaussian weighting function was applied to the totality of the data (i.e., all re-acquisitions) using a single Gaussian kernel. The initial polynomial stage of the decorrelation process may seem unnecessary, since the weighting function alone could remove structure in the data on both large and small spatial scales. However, we find that the polynomials speed up the iterative process by providing a fast start to the iteration. Our final photometry has a standard deviation of  $3.7 \times 10^{-3}$ , which is only 15% greater than the photon noise. Moreover, red noise is minimal and the precision for binned data improves nearly as the square-root of the bin size, as we demonstrate below.

Figure 2.2 shows an overview of our  $4.5 \mu\text{m}$  photometry, after decorrelation; more detailed depictions are discussed and shown below.

## 2.4 Model Fitting for Transit Parameters

We analyze all available Spitzer transits, including a re-analysis of the transits reported by Désert et al. (2011) [37], and TRAPPIST transits using the I+z filter [82]. We use three methodologies to determine the best-fit transit parameters for each dataset and wavelength. All three methods use only the data within a phase interval of  $\pm 0.05$  around the center of each transit— except for the TRAPPIST transits, which used all of the available data from Gillon et al. (2012) [82].

The first method solves for the best-fit transit parameters of all transits simultaneously at each wavelength. The second method fits each transit individually

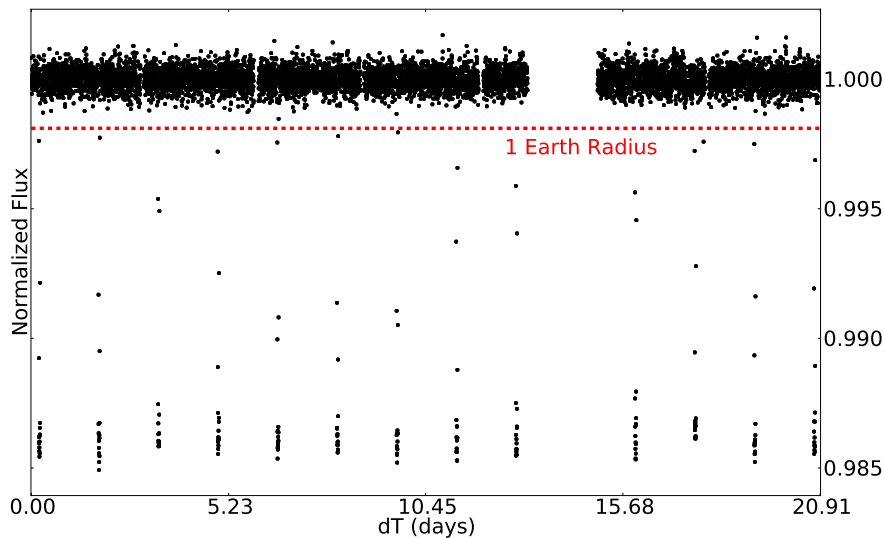


Figure 2.2: Overview of our  $4.5 \mu\text{m}$  photometry, after decorrelation and binned in 100 two-second exposures per plotted point. The dashed line shows the transit depth that corresponds to one Earth radius. The 13 transits of GJ1214b are apparent. See Gillon et al. (2012) [82] for an analysis of other possible transiting planets in this system.

and independently, then calculates the average of the transit parameters at each wavelength, weighting the individual results by the inverse of their variance. The third method phases and bins all of the transits at each wavelength into a single transit, and fits to those phased & binned data. All 3 methods included a total of 3 transits at  $3.6 \mu\text{m}$ , 14 transits at  $4.5 \mu\text{m}$ , and 7 transits in the I+z band. Comparing these three methods gives an indication of the consistency of our results, and we do indeed find good consistency, as noted below.

We now describe the details of those fitting procedures.

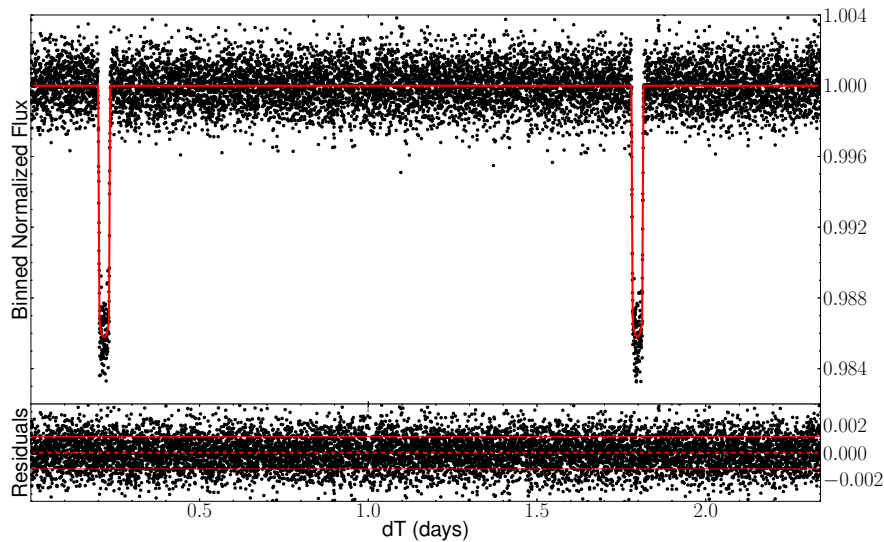


Figure 2.3: Expansion of a two-transit portion of the  $4.5 \mu\text{m}$  photometry (Figure 2.2), with the best-fit transit curves overlaid, binned by every 10 data points. The red lines in the lower panel show a  $\pm 1\sigma$  envelope.

#### 2.4.1 Spitzer $4.5 \mu\text{m}$ Transits

We use the formulation of Mandel et al. (2002) [88] to generate transit curves and fit them to the observed data, thereby extracting the essential parameters of the transit. The 14 Spitzer transits at  $4.5 \mu\text{m}$  comprise our most extensive and highest quality data. Our simultaneous fit holds the orbital period fixed at the value measured by Bean et al. (2011) [77] ( $1.58040481 \pm 1.210^{-7}$ ), and uses a Levenberg-Marquardt algorithm to minimize the  $\chi^2$  for each transit. Although we are minimizing  $\chi^2$ , we do not accept that particular set of transit parameters as our best-fit values. Instead, we explore parameter space using a Markov Chain Monte Carlo (MCMC) method, and also using a residual-permutation (‘prayer-bead’) method.

Table 2.1: Results of fitting to 13 individual transits of GJ1214b at 4.5  $\mu\text{m}$ , plus the transit observed by Désert et al. 2011a [37].

Epoch	$T_c - 2450000(BJD_{\text{TDB}})$	$i$	$a/R_*$	$R_p/R_*$	$c_0$
211	$5314.214114 \pm 0.000085$	$88.81 \pm 0.39$	$14.92 \pm 0.40$	$0.11726 \pm 0.00105$	$0.133 \pm 0.074$
443	$5680.867846 \pm 0.000059$	$89.30 \pm 0.33$	$15.51 \pm 0.28$	$0.11735 \pm 0.00064$	$0.097 \pm 0.046$
444	$5682.448272 \pm 0.000067$	$88.89 \pm 0.37$	$14.98 \pm 0.39$	$0.11692 \pm 0.00077$	$0.208 \pm 0.047$
445	$5684.028698 \pm 0.000056$	$89.88 \pm 0.36$	$15.72 \pm 0.27$	$0.11681 \pm 0.00057$	$0.126 \pm 0.041$
446	$5685.609139 \pm 0.000048$	$89.11 \pm 0.23$	$15.24 \pm 0.24$	$0.11625 \pm 0.00034$	$0.118 \pm 0.029$
447	$5687.189632 \pm 0.000065$	$88.23 \pm 0.26$	$14.11 \pm 0.41$	$0.11796 \pm 0.00054$	$0.059 \pm 0.051$
448	$5688.769880 \pm 0.000094$	$89.42 \pm 0.36$	$15.38 \pm 0.30$	$0.11586 \pm 0.00100$	$0.170 \pm 0.067$
449	$5690.350385 \pm 0.000052$	$88.34 \pm 0.23$	$14.33 \pm 0.36$	$0.11803 \pm 0.00052$	$0.098 \pm 0.050$
450	$5691.930794 \pm 0.000067$	$88.22 \pm 0.25$	$14.24 \pm 0.43$	$0.11865 \pm 0.00049$	$0.033 \pm 0.033$
451	$5693.511181 \pm 0.000058$	$88.81 \pm 0.25$	$14.95 \pm 0.29$	$0.11737 \pm 0.00053$	$0.130 \pm 0.046$
453	$5696.671937 \pm 0.000073$	$88.68 \pm 0.37$	$14.75 \pm 0.41$	$0.11606 \pm 0.00075$	$0.189 \pm 0.047$
454	$5698.252258 \pm 0.000047$	$88.93 \pm 0.28$	$15.14 \pm 0.30$	$0.11567 \pm 0.00047$	$0.056 \pm 0.029$
455	$5699.832550 \pm 0.000068$	$88.24 \pm 0.28$	$14.17 \pm 0.43$	$0.11802 \pm 0.00062$	$0.070 \pm 0.058$
456	$5701.413161 \pm 0.000059$	$89.61 \pm 0.30$	$15.41 \pm 0.23$	$0.11549 \pm 0.00066$	$0.205 \pm 0.042$

Our best-fit values are taken from the medians of the posterior distributions generated in this exploration of parameter space (see Sec. 4.4).

Our fit extracts a correction to the transit center time (as might be caused by ephemeris error), as well as  $a/R_*$ ,  $i$ ,  $R_p/R_*$ , and a linear limb-darkening coefficient. We hold the quadratic limb darkening coefficient at zero because Bayesian Information Criterion [89] analysis supports a linear law, which gives an adequate account of the minimal limb darkening that is characteristic of infrared transits. Moreover, our derived linear limb darkening coefficients at 3.6 and 4.5 microns ( $c_0 = 0.158$  and  $0.128$  respectively, see Table 4) are reasonably consistent with the values predicted by Claret et al. (2011) [90] ( $c_0 = 0.147$  and  $0.155$ ) for a model atmosphere having  $T = 3500\text{K}$  (that temperature being their closest match to GJ1214).

Figure 2.3 zooms in on a portion of the simultaneous fit for the first two 4.5  $\mu\text{m}$  transits, and Figure 2.4 shows the standard deviation of residuals (data minus simultaneous fit) when binned over different time intervals. Note that we find very little red noise in these data, indicating the success of our multi-stage intra-pixel

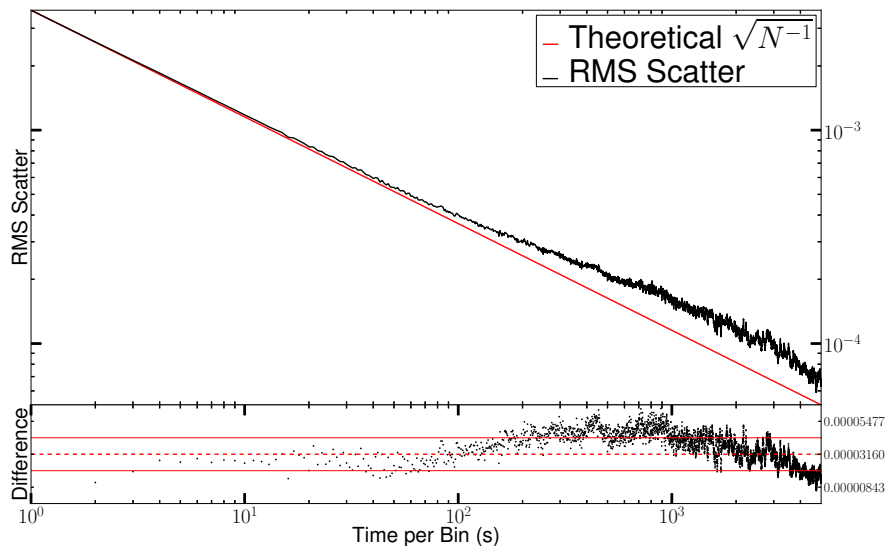


Figure 2.4: Standard deviation of the residuals (data minus the ‘simultaneous’ fit, in units of the stellar flux) for all 14 transits at  $4.5 \mu\text{m}$ , versus bin size. The red lines in the lower panel show a  $\pm 1\sigma$  envelope.

decorrelation. Note also that our decorrelation process will tend to remove slow variations in the stellar brightness. Hence the apparently constant flux seen in Figure 2.2 should not be interpreted as evidence for stellar quiescence. (The possible effects of stellar activity on our results are discussed in Sec. 5).

In addition, we bin all 14  $4.5 \mu\text{m}$  transits, including that of Désert et al. (2011) [37], into bins of width 0.001 in phase, using a running standard deviation for the weights in a weighted mean— phasing them all to a common epoch determined from the simultaneous fit. As before, we include only data within a phase range  $\pm 0.05$  of transit center, and we fit to the phased & binned transit using the same Levenberg-Marquardt algorithm described above. Figure 2.5 shows the resulting fit in comparison to the phased & binned data.

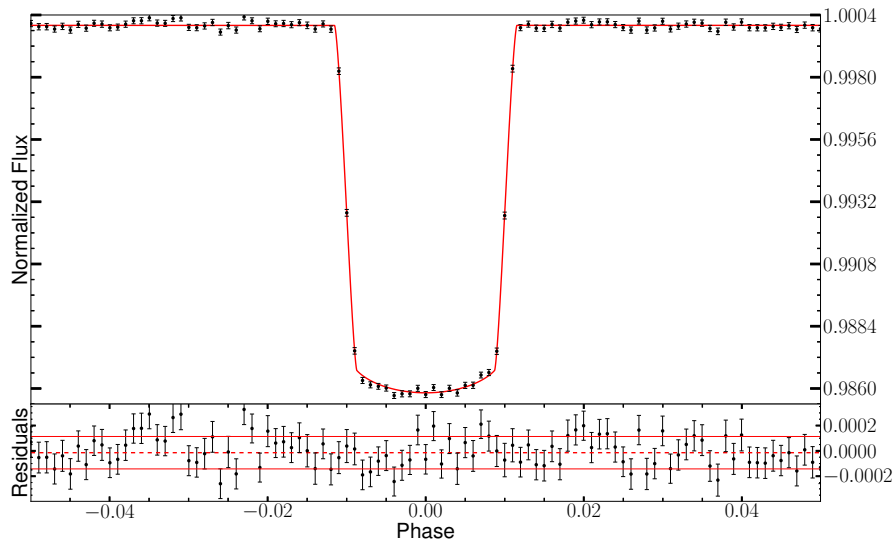


Figure 2.5: Phased & binned transit of GJ1214b at  $4.5 \mu\text{m}$  from our 13 Spitzer transits, plus the transit observed by Désert et al. (2011) [37].

The best-fit Spitzer transit parameters for each  $4.5 \mu\text{m}$  transit fitted individually are given in Table 2.1; the individual  $3.6 \mu\text{m}$  transits (Sec. 4.2) are given in Table 2.2, and the individual TRAPPIST results (Sec. 4.3) are given in Table 2.3. Results using the combining methods are summarized in Sec. 4.5.

## 2.4.2 Spitzer $3.6 \mu\text{m}$ Transits

Our 42-hour ‘replacement’ observations contain two transits at  $3.6 \mu\text{m}$ , one near the beginning of these data and one near the end. The photometry for these transits was decorrelated using the same methodology described above for  $4.5 \mu\text{m}$ . In contrast to the  $4.5 \mu\text{m}$  case, our  $3.6 \mu\text{m}$  photometry exhibits noticeable red noise. Fortunately, this red noise is most significant in the long interval between the two transits. We limited the effect of this red noise by limiting the range of the data

included in our decorrelations and fits. The omitted data did not occur near the transits, nevertheless we tried to develop objective criteria for the range of data that were used.

After comparing the  $\sigma$  vs.  $N^{-0.5}$  and global  $\sigma$ , or RMS scatter, of various sized data slices, we determined that trimming the 3.6  $\mu\text{m}$  data set into a phase range of  $\pm 0.05$  around the center of each transit minimized the RMS scatter and the residual of the  $\sigma$  vs.  $N^{-0.5}$  slope, which minimized the red noise for these transits; and was fortuitously the same range as the  $\pm 0.05$  in phase that we adopted for our 4.5  $\mu\text{m}$  fits.

We repeated all of the methodology described in this section on the Désert et al. (2011) [37] 3.6  $\mu\text{m}$  transit data, and we found that the slope of  $\sigma$  vs.  $N^{-0.5}$  was insensitive to the range of data analyzed. As a result, we use the entire Désert et al. (2011) [37] 3.6  $\mu\text{m}$  data set.

Table 2.2: Results of fitting to two individual transits of GJ1214b at 3.6  $\mu\text{m}$ , plus the transit observed by Désert et al. (2011) [37].

Epoch	$T_c - 2450000(BJD_{\text{TDB}})$	$i$	$a/R_*$	$R_p/R_*$	$c_0$
210	$5312.633724 \pm 0.000072$	$89.998 \pm 0.324$	$15.659 \pm 0.160$	$0.11665 \pm 0.00082$	$0.200 \pm 0.061$
564	$5872.096721 \pm 0.000094$	$89.144 \pm 0.383$	$15.331 \pm 0.354$	$0.11619 \pm 0.00121$	$0.114 \pm 0.065$
565	$5873.677187 \pm 0.000062$	$89.221 \pm 0.296$	$15.418 \pm 0.281$	$0.11584 \pm 0.00066$	$0.135 \pm 0.049$

As in the 4.5  $\mu\text{m}$  case, we fit to all 3 of the 3.6  $\mu\text{m}$  transits using 3 methods: simultaneously, individually, and phased & binned. Figure 2.6 shows all 3 of the 3.6  $\mu\text{m}$  transits phased & binned, overlaid with a best-fit curve. Figure 2.7 illustrates the standard deviation of the 3.6  $\mu\text{m}$  residuals as a function of bin size for our fits to the simultaneous transit parameters.

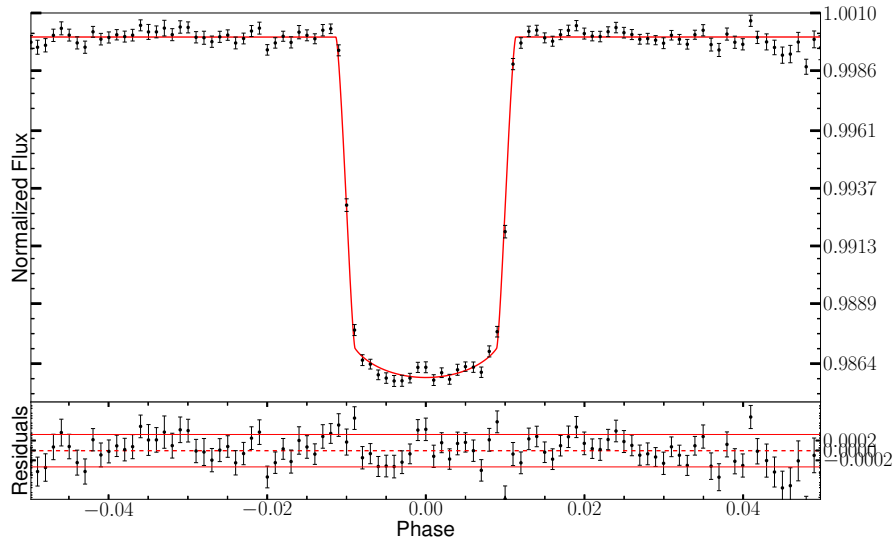


Figure 2.6: Phased & binned transit of GJ1214b at  $3.6 \mu\text{m}$  from our two Spitzer transits, plus the transit observed by Désert et al. (2011) [37].

### 2.4.3 TRAPPIST I+z Transits

For the TRAPPIST data set, we used all 7 distinct epochs of the GJ1214b transiting system provided by Gillon et al. (2012) [82]. Three of these epochs overlapped with the Spitzer  $4.5 \mu\text{m}$  data set. Gillon et al. (2012) [82] used the I+z filter on the TRAPPIST telescope because it supplied a near uniform filter profile from  $0.7 - 1.0 \mu\text{m}$ .

We determined the physical parameters using all three methods discussed above: a simultaneous fit, individual fits, and a fit to phased & binned data. Similar to the Spitzer data sets, we fit a Mandel et al. (2002) [88] transit model using a Levenberg-Marquardt routine. In contrast to the Spitzer data sets, we fit the TRAPPIST data using a Mandel et al. (2002) [88] model that included quadratic

Table 2.3: Results of fitting to 7 individual transits of GJ1214b in the I+z-band, observed by TRAPPIST [82].

Epoch	$T_c - 2450000(BJD_{\text{TDB}})$	$i$	$a/R_*$	$R_p/R_*$	$c_0$	$c_1$
412	$5631.875656 \pm 0.000092$	$88.035 \pm 0.365$	$13.743 \pm 0.443$	$0.11680 \pm 0.00135$	$0.237 \pm 0.094$	$0.073 \pm 0.177$
424	$5650.840034 \pm 0.000152$	$87.805 \pm 0.384$	$13.215 \pm 0.515$	$0.12389 \pm 0.00216$	$0.331 \pm 0.176$	$0.110 \pm 0.220$
436	$5669.805222 \pm 0.000110$	$88.990 \pm 0.436$	$14.945 \pm 0.562$	$0.11389 \pm 0.00275$	$0.422 \pm 0.170$	$0.267 \pm 0.345$
441	$5677.706878 \pm 0.000170$	$88.965 \pm 0.412$	$14.923 \pm 0.550$	$0.11573 \pm 0.00331$	$0.428 \pm 0.198$	$0.008 \pm 0.370$
443	$5680.867699 \pm 0.000131$	$88.336 \pm 0.397$	$14.049 \pm 0.486$	$0.12138 \pm 0.00182$	$0.012 \pm 0.153$	$0.602 \pm 0.298$
453	$5696.672075 \pm 0.000135$	$89.873 \pm 0.671$	$14.932 \pm 0.741$	$0.10802 \pm 0.00296$	$0.646 \pm 0.142$	$0.141 \pm 0.242$
455	$5699.832535 \pm 0.000143$	$88.360 \pm 0.460$	$14.516 \pm 0.641$	$0.11877 \pm 0.00228$	$0.343 \pm 0.138$	$0.005 \pm 0.268$

limb darkening, which accounted for the excess stellar limb-darkening observed in the shorter wavelength transit data. The fit to the phased & binned TRAPPIST data is shown as Figure 2.8. To analyze the quality of the fit, Figure 2.9 shows the  $\sigma$  vs.  $N^{-0.5}$  for the simultaneous fit of the TRAPPIST data set.

The results for the planet-to-star radius ratios, and related error bars, in the I+z band are plotted on Figure 2.10 for comparison to our 13 Spitzer transits at  $4.5 \mu\text{m}$ , and listed in Table 2.3 & Table 2.4. Further information about the data reduction process for the TRAPPIST data set is included in Gillon et al. (2012) [82].

#### 2.4.4 Errors

We used two methods to estimate uncertainties for our derived transit parameters: MCMC and prayer-bead. In both methods the errors - as well as the best-fit values - follow from the posterior distributions. We adopted the prayer-bead method for our quoted results because it explicitly includes the effect of red noise [91]. Figure 2.11 shows the distributions for  $R_p/R_*$  for one of our  $4.5 \mu\text{m}$  individual fits, showing a broader distribution for the prayer-bead method.

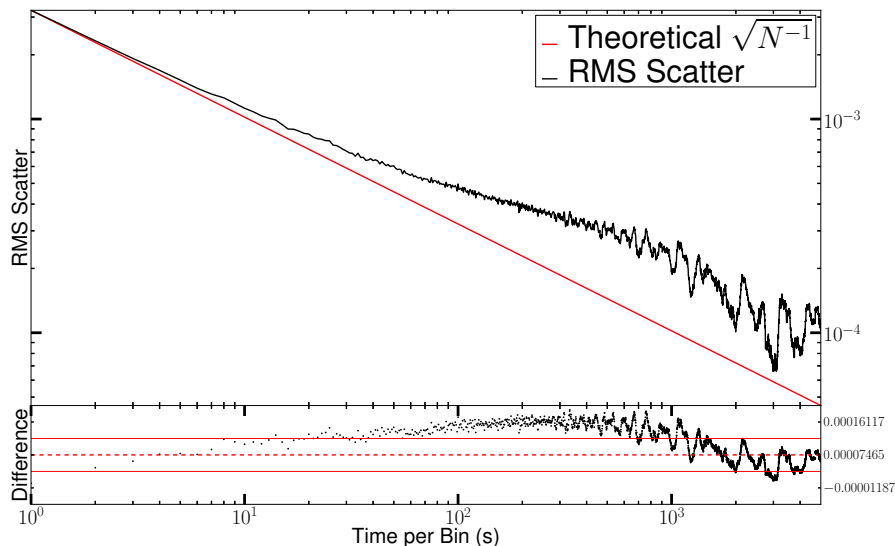


Figure 2.7: Standard deviation of the residuals (data minus the ‘simultaneous’ fit, in units of the stellar flux) for our two transits at  $3.6 \mu\text{m}$  plus the Désert et al. (2011) [37] transit, versus bin size. The extra scatter in this figure, compared to Figure 4 above, is related to the number of data points binned overall. There are almost an order of magnitude less points at  $3.6 \mu\text{m}$  than  $4.5 \mu\text{m}$ .

In implementing the prayer-bead method, we permute the residuals only within the adopted phase range of the fit ( $\pm 0.05$  in phase). At each permutation, we find the best-fit transit parameters using the Levenberg-Marquardt method, and we add those best-fit values to the posterior distributions of each parameter. We adopt the median of the posterior distribution as the best fit value, following Désert et al. (2011b) [91].

A potential additional source of error is associated with the decorrelation, that is not explicitly propagated into the stage of fitting the photometry. However, we are not concerned about this for two reasons. First, the  $4.5 \mu\text{m}$  data are so extensive,

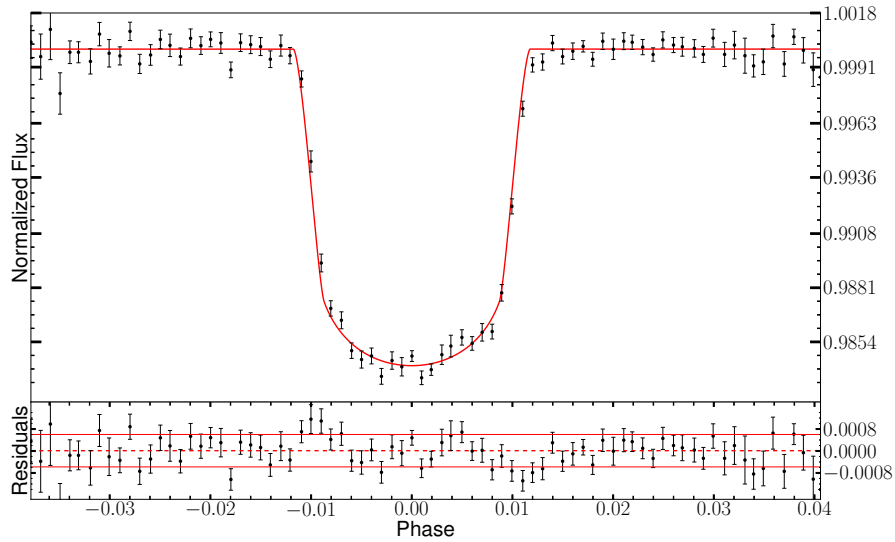


Figure 2.8: Phased & binned transit of GJ1214b in the I+z band, from TRAPPIST, observed by Gillon et al. (2012) [82].

and the intra-pixel effect is so modest at that wavelength, that we believe those errors in decorrelation have negligible effect. Second, our procedure accounts for imperfect decorrelation at both Spitzer wavelengths, in an *implicit* fashion. Imperfections in decorrelation create red noise, and that red noise contributes to errors on the derived transit parameters using the prayer-bead method.

In addition to random error, systematic differences may exist between our results and other investigators. We discuss one source of possible systematic difference in Sec. 4.5; the implications of these differences for the nature of GJ1214b’s atmosphere is discussed in Sec. 6.

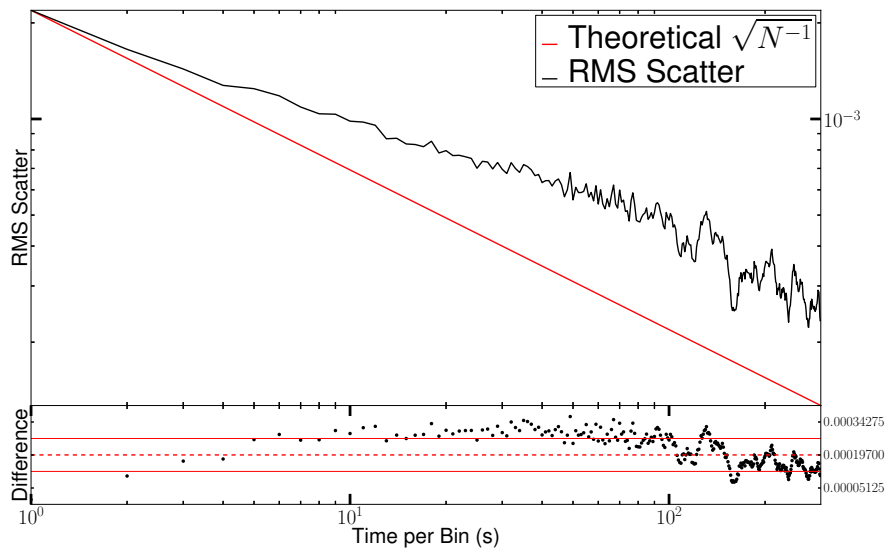


Figure 2.9: Standard deviation of the residuals (data minus the ‘simultaneous’ fit, in units of the stellar flux) for our seven transits in the I+z band on TRAPPIST. The extra scatter in this figure, compared to Figure 4 & 7 above, is related to the number of data points binned overall. We were only able to bin out to 300 data points per bin because the most extensive TRAPPIST transit comprised 300 data points.

## 2.4.5 System Parameters

As noted above, we estimated the system parameters using three methods: 1) simultaneous fitting of all transits at a given wavelength, 2) averaging system parameters from the individual fits to each transit at a given wavelength, and 3) fitting to phased & binned combinations of transits at a given wavelength. We included the transits observed by Désert et al. (2011) [37] in all three methods. We also fit the TRAPPIST transits using all three methods (see Table 2.4). Table 2.1 lists the individual fits to the 4.5  $\mu\text{m}$  data; Table 2.2 gives the individual fit results at 3.6  $\mu\text{m}$  and Table 2.3 lists the individual fit results for the TRAPPIST transits

Table 2.4: Results of fitting to composite transits, i.e.: simultaneous fits, averaging individual transits, and fitting to phased & binned transits.

Method/Channel	$T_c - 2450000(BJD_{\text{TDB}})$	$i$	$a/R_*$	$R_p/R_*$	$c_0$	$c_1$
Simultaneous 3.6 $\mu\text{m}$	$4966.524895 \pm 0.000047$	$89.566 \pm 0.139$	$15.607 \pm 0.104$	$0.11607 \pm 0.00030$	$0.156 \pm 0.022$	fixed at 0.0
Simultaneous 4.5 $\mu\text{m}$	$4966.524918 \pm 0.000030$	$88.794 \pm 0.061$	$15.049 \pm 0.095$	$0.11710 \pm 0.00017$	$0.110 \pm 0.014$	fixed at 0.0
Simultaneous TRAPPIST I+z	$4966.524881 \pm 0.000063$	$88.240 \pm 0.230$	$14.011 \pm 0.288$	$0.11873 \pm 0.00111$	$0.320 \pm 0.097$	$0.187 \pm 0.176$
Averaged individual 3.6 $\mu\text{m}$	$4966.524898 \pm 0.000076$	$89.469 \pm 0.221$	$15.564 \pm 0.080$	$0.11616 \pm 0.00019$	$0.148 \pm 0.021$	fixed at 0.0
Averaged individual 4.5 $\mu\text{m}$	$4966.524925 \pm 0.000027$	$88.803 \pm 0.127$	$15.090 \pm 0.137$	$0.11699 \pm 0.00026$	$0.110 \pm 0.015$	fixed at 0.0
Averaged individual TRAPPIST I+z	$4966.524968 \pm 0.000077$	$88.437 \pm 0.057$	$14.207 \pm 0.239$	$0.11793 \pm 0.00182$	$0.324 \pm 0.068$	$0.146 \pm 0.073$
Phased & binned 3.6 $\mu\text{m}$	$4966.524156 \pm 0.000043$	$89.469 \pm 0.143$	$15.547 \pm 0.091$	$0.11602 \pm 0.00055$	$0.158 \pm 0.035$	fixed at 0.0
Phased & binned 4.5 $\mu\text{m}$	$4966.524297 \pm 0.000016$	$88.439 \pm 0.061$	$14.442 \pm 0.093$	$0.11709 \pm 0.00022$	$0.128 \pm 0.018$	fixed at 0.0
Phased & binned TRAPPIST I+z	$4966.524122 \pm 0.000079$	$88.314 \pm 0.177$	$14.053 \pm 0.259$	$0.11803 \pm 0.00079$	$0.263 \pm 0.107$	$0.316 \pm 0.149$

in the I+z band.

Since our different fitting methods (summarized in Table 2.4) are simply different ways of accounting for the same data, they should give consistent results as far as the best-fit parameters are concerned. Beyond best-fit consistency, we find that comparison of these methods can provide a basis for caution concerning the errors on the derived parameters. For example, our 4.5  $\mu\text{m}$  results from the simultaneous fit give  $R_p/R_* = 0.11710 \pm 0.00017$ , whereas averaging the individual fits, weighted by the inverse of their variances, gives  $R_p/R_* = 0.11699 \pm 0.00026$ . Although the best-fit values agree well, the larger error from averaging the individual fits may indicate potential variations from transit-to-transit.

Table 2.5 summarizes our results for the  $R_p/R_*$  parameter that potentially reveals information about the atmosphere of GJ1214b into one concise Table. For the discussion that follows, we adopt the results from the phased & binned method, because we feel that the high precision of these combined transit curves allows the most reliable solution.

We explored further comparison with two other precise measurements of  $R_p/R_*$ : Bean et al. (2011) [77] and Berta et al. (2012) [38]. We choose these investigations for



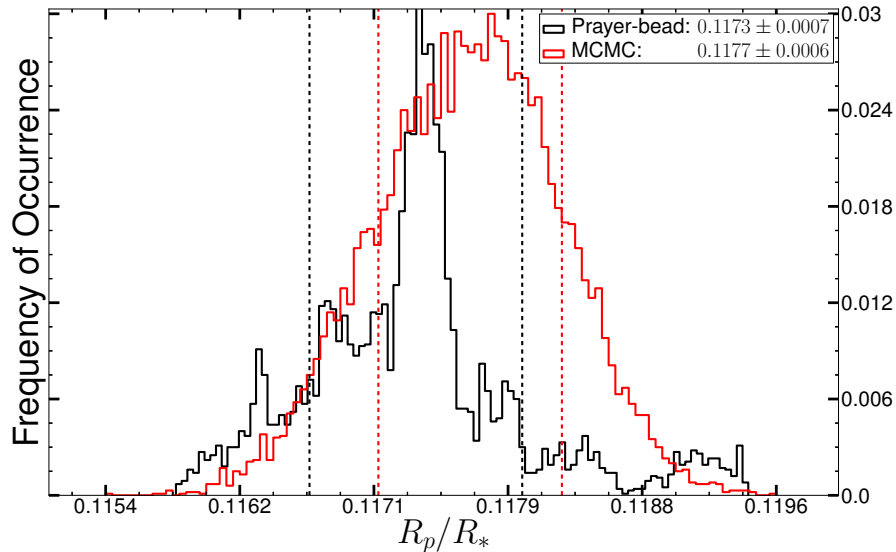


Figure 2.11: Histograms (posterior distributions) of  $R_p/R_*$  for the individual fit to the first of our  $4.5 \mu\text{m}$  transits, showing results from both the MCMC and prayer-bead methods; with dashed lines for the  $1\sigma$  threshold of each distribution.

However, the low limb darkening that prevails at Spitzer wavelengths, in combination with the high precision we achieve from our large dataset, motivates us to rely primarily on our own orbital parameters. Nevertheless, we explore the implications of adopting the Bean et al. (2011) [77] and Berta et al. (2012) [38] orbital parameters in Sec. 6.

## 2.5 Transit-to-Transit Variability and Star Spots

A star spot crossing during transit appears as an anomalous spike or bump in the transit light curve (e.g., [61]). Our photometry shows no evidence that the planet crossed even one significant star spot during our thirteen  $4.5 \mu\text{m}$  transits. Nevertheless, spots are common on M-dwarf stars, and uncrossed star spots could

still affect the transit [42, 91].

TRAPPIST photometry of GJ1214 out of transit, but over the same time period as our 4.5  $\mu\text{m}$  Spitzer observations, shows essentially no variation in the I-band [82], to a limit of about 0.2%. Nevertheless, other investigations have found that GJ1214 exhibits rotationally-modulated signatures of star spots, so we consider the potential impact of such variation on our results. As we will demonstrate below, even allowing for more photometric variation than Gillon et al. (2012) [82] observed, star spots have negligible effect on our results.

Berta et al. (2011) [79] found that GJ1214 shows a photometric variation of 1% amplitude (2% peak-to-peak) in the I-band (0.715-1.0  $\mu\text{m}$ ) with a rotation period of  $\sim 53$  days, based on MEarth data [92], spanning three years of observations. Using PHOENIX model atmospheres [93], we calculate that the Berta et al. (2011) [79] amplitude of variation could be produced by two star spots, each covering as much as 2% of the sky-projected stellar disk, separated in longitude by  $180^\circ$ . Based on Doppler imaging studies of active dwarf stars [94], we adopt a temperature contrast (spot vs. photosphere)  $\Delta T/T = 0.1$ , thus  $T_{spot} \sim 2700K$ . Note that this is the same as adopted by Berta et al. (2011) [79]. We use limb darkening coefficients for both the photosphere and the star spot, calculated from our transit fitting at 4.5  $\mu\text{m}$  ( $c_0 = 0.11$ ,  $c_1 = 0.0$ ). On this basis, we determined that a 1% variation of the stellar light curve in the I-band translates to 0.42% variation in Spitzer photometry at 4.5  $\mu\text{m}$ .

We developed a numerical tile-the-star model to calculate the effect of unocculted star spots on the transit depth. We created a synthetic time-series of 2D

images of GJ1214, at 4.5  $\mu\text{m}$ , and projected two circular star spots on its surface at the equator, separated by 180° of longitude. This arrangement of spots in opposite hemispheres produces an appropriate quasi-sinusoidal effect in the total stellar light.

We accounted for variation in the spots projected area as the star rotates, but we ignored the Wilson depression effect. The PHOENIX model with  $T = 3000\text{K}$ ,  $[M/H] = +0.3$ ,  $\log(g) = 5.0$  and  $\alpha = 0.0$  represented GJ1214; and, the PHOENIX model with  $T = 2700\text{K}$ ,  $[M/H] = +0.3$ ,  $\log(g) = 5.0$ ,  $\alpha = 0.0$  represented the star spot. We multiplied Spitzer’s 4.5  $\mu\text{m}$  filter profile by the spectral models and integrated over wavelength to calculate the expected 4.5  $\mu\text{m}$  flux variations due to stellar rotation with the spots fixed in longitude. Both the star and spots are affected by limb darkening as determined by our fitted transit model parameters [88].

It is easy to show that the effect of unocculted star spots on the planetary radius derived from the transit is given as:

$$\left(\frac{R_p}{R_*}\right)_{spotted}^2 = \frac{F_{ot} - F_{it}}{F_{ot}} = \frac{\left(\frac{R_p}{R_*}\right)_{spotless}^2 I_{ph}}{(1 - \epsilon)I_{ph} + \epsilon I_{spot}} \quad (2.3)$$

with  $\epsilon = \frac{A_{spot}}{\pi R_*^2}$ , and where *ot* indexes out of transit, *it* indexes in transit.  $I$  indicates the intensity of the stellar disk,  $I_{ph}$  being the intensity of the photosphere, and  $I_{spot}$  being the intensity of the spot.

Using this equation together with flux variations from our tile-the-star model, we calculated the potential variation in transit depth as a function of time. This quasi-sinusoidal variation has an unknown phase because we do not know the longi-

tudes of any real star spots on GJ1214. Nevertheless, the amplitude of variation in  $R_p/R_*$  from this model is  $9.6 \times 10^{-5}$ , which is negligible compared to the observed scatter in our measurements (see Figure 2.11). Moreover, as noted above, the photometric variations of GJ1214, observed concurrently with our transit data [82], were much less than from Berta et al. (2011) [79]. We therefore conclude that star spots play a negligible role on the observed variations and/or possible bias of our inferred radii for GJ1214b. However, we cannot exclude the possibility that increased star spots during Bean et al. (2011) [77] and Berta et al. (2011) [38] observations are responsible for some of the differences between our results.

## 2.6 The Atmosphere of GJ1214b

There are numerous transit observations in the literature that bear on the nature of the atmosphere of GJ1214b [25, 28, 37, 38, 77, 79–81, 95–99]. Nevertheless, the improved precision we have been able to achieve in the Spitzer bands, together with the new TRAPPIST results in the I+z-band, and recent advances in modeling the atmosphere of GJ1214b [9, 70], motivate us to re-examine the nature of GJ1214b’s atmosphere.

In the following sub-sections we review the methodology for comparing observations and models (Sec. 6.1), we briefly preview what our Spitzer observations alone can reveal concerning the atmosphere of GJ1214b (Sec. 6.2), and we then compare the totality of all published observations to existing models, using a  $\chi^2$  analysis (Sec. 6.3). Since planetary radii derived by different observational groups

can differ systematically, we discuss the effect of one particular systematic difference in Sec. 6.4, and we summarize our conclusions concerning the atmosphere of GJ1214b in Sec. 6.5.

### 2.6.1 Comparing Models to Observations

To compare transmission models for GJ1214b with the observations, we need to integrate the models—multiplied by the filter profiles—over the observed bandpasses. Let  $F_{ot}(\lambda)$  be the out of transit flux measured from the star as a function of wavelength. Similarly let  $F_{it}(\lambda)$  be the in-transit flux as a function of wavelength. Consider the simplified case where limb darkening can be neglected (arguably applicable in the infrared), and include the fact that there is a wavelength-dependent observational sensitivity,  $S(\lambda)$ . In that case:

$$F_{it}(\lambda) = S(\lambda)I_*(\lambda)(\pi R_*^2 - \pi R_p(\lambda)^2), \quad (2.4)$$

where  $I_*(\lambda)$  is the intensity emergent from the stellar atmosphere at wavelength  $\lambda$ . The out of transit flux is:

$$F_{ot}(\lambda) = S(\lambda)I_*(\lambda)\pi R_*^2. \quad (2.5)$$

With realistic spectral resolution, the observed quantities are integrals over the observational bandpass, and the transit depth  $d$  is:

$$d = \int [F_{ot}(\lambda) - F_{it}(\lambda)]d\lambda / \int F_{ot}(\lambda)d\lambda, \quad (2.6)$$

Thus:

$$d = \int S(\lambda)I_*(\lambda)R_p(\lambda)^2 d\lambda / \int S(\lambda)I_*(\lambda)R_*^2 d\lambda. \quad (2.7)$$

When we seek to evaluate a model of the planet’s transit radius as a function of wavelength ( $R_p(\lambda)$ ), it is necessary to include the wavelength dependence of the stellar intensity as well as the observational sensitivity. The latter is commonly incorporated in numerous studies of both transits and secondary eclipses, but the necessity of including the stellar intensity is less widely appreciated, especially the possible effect of line structure in the stellar spectrum. For example, if the stellar spectrum contains water vapor absorption that overlaps to some degree with planetary water vapor features, then the apparent transit depth will be reduced compared to the case where the star is purely a continuum source. Stellar intensity weighting is particularly important for M-dwarf host stars like GJ1214, because their spectrum varies strongly with wavelength in the optical and near-IR. Unfortunately, that weighting is also considerably uncertain for M-dwarf stars, particularly at the very interesting blue wavelengths where the planet may exhibit scattering from haze [9, 70].

To compare models of  $R_p(\lambda)/R_*$  to observations, we calculate the value of  $d$  using Eq. (6), and infer  $R_p/R_*$  as  $\sqrt{d}$ . This procedure is valid even at wavelengths where appreciable limb darkening prevails.

Although we use a PHOENIX model atmosphere to perform the weighting over the observed bandpass, this model is not ultimately satisfactory for this purpose.

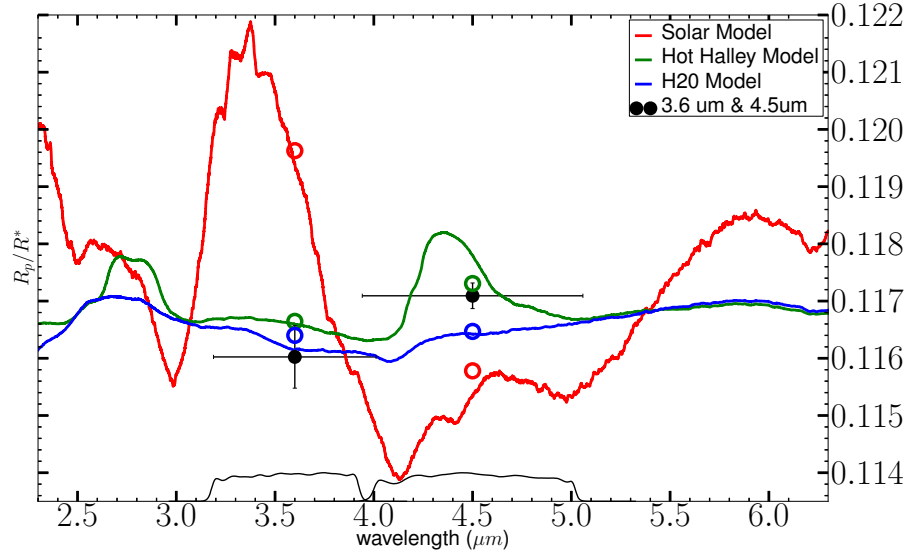


Figure 2.12: Comparison between our Spitzer results and three recent models for the atmosphere of GJ1214b, from Benneek & Seager (2012) [9]: a cloudless solar model, a comet-like model, and a water vapor model.

For example, in the green bandpass ( $0.46 \mu\text{m}$ ) where a transit was observed by de Mooij et al. (2012) [80], the PHOENIX model has essentially no flux (many orders of magnitude below the peak flux), whereas the real star has sufficient flux to produce a transit having good signal-to-noise [80]. The reason is that the model includes only LTE thermal emission from the star, and does not incorporate the various emission signatures of magnetic activity. Therefore we can use the PHOENIX model only in the red-optical and infrared. Our default procedure is to hold the stellar intensity constant for wavelengths shortward of  $1000 \text{ nm}$  (i.e., we set  $I_*(\lambda) = I_*(1000)$  for  $\lambda \leq 1000 \text{ nm}$ ), but we verified that using other prescriptions shortward of this limit (e.g., blackbody spectra) do not greatly influence our present results. However, as the precision of observations improves, it will eventually be necessary to have an

accurate spectrum for the host star at all wavelengths.

## 2.6.2 Implications from Spitzer

Prior to an exhaustive analysis of all data versus all models, we mention what our new Spitzer data alone immediately reveal and/or constrain concerning the atmosphere of GJ1214b. We (BB & SS) generated three new model atmospheres for GJ1214b at an equilibrium temperature of 546 K, based on the methodology of Benneek & Seager (2012) [9]. The models are: 1) a H-rich solar abundance model, 2) a ‘Hot-Halley’ composition model which begins with solar composition and adds minor molecular constituents from accreted icy material [9], and 3) a pure water vapor atmosphere. Figure 2.12 shows the result of integrating these three models over the Spitzer observational bandpasses, and including the stellar intensity using a PHOENIX model having  $T_{\text{eff}}/\log(g)/[M/H] = 3000 \text{ K}/5.0/0.3$ . Based on this comparison, the solar composition model is eliminated based on the Spitzer data alone. The water vapor model is preferred over the hot Halley model, based on the  $\chi^2$  analysis described below. Moreover, we expect that methane-rich models having large scale heights (not illustrated) will be rejected by the Spitzer data, due to the relative lack of an enhanced radius in the  $3.6 \mu\text{m}$  band - that contains the strong  $\nu_3$  band of methane.

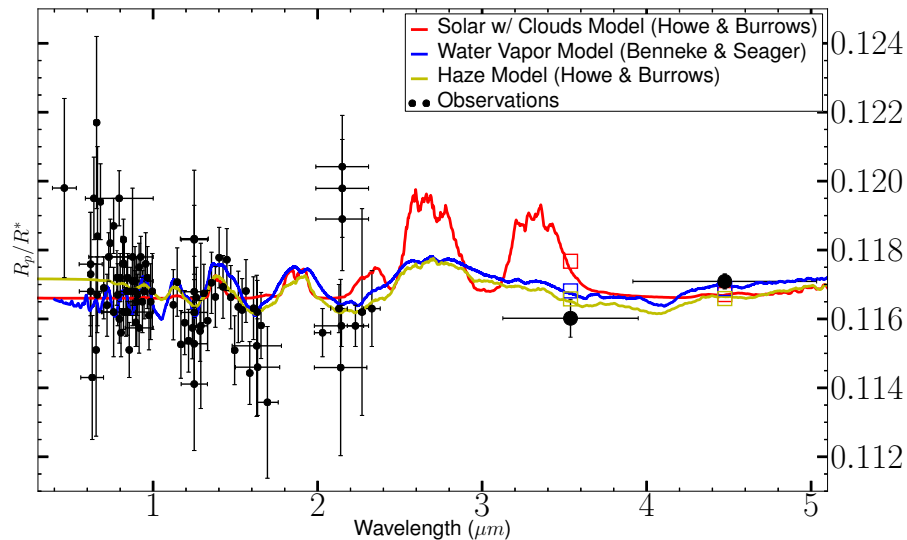


Figure 2.13: Comparison between all published observations of GJ1214b, including our Spitzer and TRAPPIST transits, and recent models. Three models having the lowest  $\chi^2$  are illustrated: a water vapor model from Benneke & Seager (2012) [9] (blue curve), a solar abundance model with very high cloud tops (at 0.1 mbars, red curve), and a model with 1-percent water vapor, and a thick tholin haze of  $0.1 \mu\text{m}$  particles extending to very high altitude (1  $\mu\text{bar}$ , yellow curve). The latter two models are from Howe & Burrows (2012) [70].

### 2.6.3 A $\chi^2$ Analysis

To gain further quantitative insight, we weighted the three models from Benneke & Seager (2012) [9] discussed above, as well as all of the models given by Howe & Burrows (2012) [70] over the observed bandpasses of all extant transit observations of GJ1214, including the TRAPPIST and warm Spitzer data reported here. We fit the models to the data using a  $\chi^2$  analysis, as described below. Berta et al. (2012) [38] applied a similar  $\chi^2$  analysis to data from Hubble/WFC3, but not to the complete set of data that we do here, and in particular not including our

new and precise results in the warm Spitzer bands. The utility of  $\chi^2$  is well known to be problematic when combining data from different observational groups. However,  $\chi^2$  is at least an objective way to compare different models, and we explicitly consider one cause of observer-to-observer systematic differences in Sec. 6.4.

To evaluate and compare possible models of the planetary atmosphere, we fit each model to the data by adding an adjustable constant (i.e., wavelength-independent offset) to the modeled values of  $R_p/R_*$ . We choose the constant to minimize the  $\chi^2$  of the difference between the adjusted model and the data. Adding this constant is equivalent to increasing (or decreasing) the size of the opaque (i.e., solid) portion of the planet by a small amount. That effectively varies the surface gravity of the planet, and would strictly speaking be inconsistent with the model that is being adjusted. However, the planetary radius at a given atmospheric pressure level is not known at a level of accuracy comparable to the adjustments we are making. Moreover, the requisite adjustments in the model output (typically, 0.0005 in  $R_p/R_*$ ), correspond to less than 1% differences in surface gravity. We therefore find this procedure to be a valid and useful tool for testing models versus the observations, and we note that a similar procedure was used by Berta et al. (2012) [38]. We fit the three models shown in Figure 2.12 [9], together with all of the models from Howe & Burrows (2012) [70], and we calculate  $\chi^2$  values for each fit. We also fit a flat line to the data, i.e., a planetary radius that does not vary with wavelength - indicating no signature of the atmosphere.

Several of the best fitting models are shown in Figure 2.13, compared to the entirety of published radii for this planet. In total, there are 97 observations of

$R_p/R_*$  versus wavelength on Figure 2.13. The water atmosphere from Figure 2.12, and two models from Howe & Burrows (2012) [70], are also included on Figure 2.13. For the Figure, the models are overplotted monochromatically, without integrating over the bandpass. However, the  $\chi^2$  values are calculated by integrating the model over the bandpass of each observation as described above, and adopting the observed errors from each source. In the case of multi-band analyses [97], we use the total bandpass from multiple filters. For the three overplotted models we also show the values for the integrals over the Spitzer bandpasses, as open symbols.

With 96 degrees of freedom, models can only be rejected at the 99.9% confidence level if they have a  $\chi^2$  exceeding 144.6. Among the possible models, The pure water atmosphere from Benneek & Seager (2012) [9] yields  $\chi^2 = 142.7$  for 96 degrees of freedom. The hot Halley and solar composition models from Benneek & Seager (2012) [9] have  $\chi^2$  values of 167.9 and 1054.7 respectively, and are unlikely descriptions of GJ1214b’s atmosphere. The solar composition model in particular is strongly rejected unless high clouds are included (see below). In this respect, we note that some discussion of a solar composition atmosphere has occurred with respect to transit observations near  $2 \mu\text{m}$  [77, 81]. We here emphasize that a cloudless solar composition model is incompatible with the Spitzer data alone, as well as with the totality of the observations over all wavelengths. The issue of the transit depth near  $2 \mu\text{m}$  - while an important datum - is not crucial to rejecting a solar composition atmosphere.

Our improvement in the observed Spitzer precision at  $3.6 \mu\text{m}$  - overlapping the strong  $\nu_3$  band of methane, prompts us to investigate the methane-composition

models of Howe & Burrows (2012) [70]. All of their methane compositions have  $\chi^2$  above 184.6 (the value for 1% methane). However, a solar composition model having high clouds (down to pressures of 0.1 mbars) produces an acceptable  $\chi^2 = 145.5$ . This model is plotted as the red line on Figure 2.13; it predicts an increase in radius in the difficult-to-observe regions near 2.7 and 3.3  $\mu\text{m}$ . The best fit to the data is the yellow line on Figure 2.13, having  $\chi^2 = 119.8$ . This model, from Howe & Burrows (2012) [70], contains a dense haze of small (0.1  $\mu\text{m}$ ) tholin particles, extending to very high altitudes (1  $\mu\text{bar}$ ). It was disfavored by Howe & Burrows (2012) [70], but our methodology is different in that we incorporate a marginally additive constant when fitting the models. However, we point out that also among the acceptable models is a flat line (not illustrated on Figure 2.13). This null hypothesis (no atmosphere detected) yields  $\chi^2 = 137.0$ .

#### 2.6.4 Systematic Differences Between Observers

One further check on the acceptable models is to focus on the difference between our precise Spitzer radii and very precise radii derived at other wavelengths, i.e., by Bean et al. (2011) [77] and Berta et al. (2012) [38]. As noted at the end of Sec. 4.5, we fix the variable orbital parameters ( $a/R_*$  and  $i$ ) at the values derived by Bean et al. (2011) [77] and Berta et al. (2012) [38] and derive a lower value of  $R_p/R_*$  at 4.5  $\mu\text{m}$  by about 0.001 (Table 2.5). Using that alternative value in our  $\chi^2$  analysis is one way of evaluating the possible effect of observer-to-observer differences in radii. This procedure increases the  $\chi^2$  values of most models, but

by varying amounts. Interestingly, the two least affected models are the flat line, whose  $\chi^2$  increases by  $\delta\chi^2 = +1.6$ , and the tholin-haze model. The water model from Benneek & Seager (2012) [9] has  $\delta\chi^2 = +8.4$ , and their hot Halley model has  $\delta\chi^2 = +19.8$ . The scattering tholin-haze model from Howe & Burrows (2012) [70] remains as the lowest absolute  $\chi^2$ , and has  $\delta\chi^2 = -2.3$ , i.e. it becomes more likely, not less likely. We conclude that, even when systematic differences among observational groups are considered, a scattering atmosphere is currently the best estimate for GJ1214b. However, we are unable to explore the vast phase space of other possible sources of systematic error. Hence we also conclude that the null hypothesis (no atmosphere detected) remains among the most favored models, especially when systematic errors are considered.

### 2.6.5 Summary of Implications for the Atmosphere of GJ1214b

We have obtained new radii for GJ1214b in the I+z band using TRAPPIST, and very precise radii at 3.6- and 4.5  $\mu\text{m}$  using Warm Spitzer in a long series of new observations. Our  $\chi^2$  analysis indicates that the best-fit model for the atmosphere of GJ1214b contains a haze of small particles extending to high altitudes, although pure water vapor models remain a possibility. However, a flat line is among the best-fitting models, particularly when observer-to-observer systematic differences are considered. Therefore we extend the conclusion of Berta et al. (2012) [38] concerning the flatness of the transmission spectrum from 1.1- to 1.7  $\mu\text{m}$  to include our new high-precision Spitzer measurements at 3.6- and 4.5  $\mu\text{m}$ . The atmosphere of

GJ1214b is not unequivocally detected at this point in time.

This work is based on observations made with the Spitzer Space Telescope, which is operated by the Jet Propulsion Laboratory, California Institute of Technology under a contract with NASA. Support for this work was provided by NASA through an award issued by JPL/Caltech. We thank the Spitzer staff for their hard work and dedication in implementing these difficult observations, and the anonymous referee for a careful review of this paper.

Table 2.5: Summary of results for  $R_p/R_*$  derived at different wavelengths using different methods. The phased & binned transit results for  $R_p/R_*$  are given for several cases: our best-fit orbital parameters ( $a/R_*$ ,  $i$ ), as well as  $R_p/R_*$  when we force the orbital parameters to have the values determined by Bean et al. (2011) [77] (14.97, 88.94) and Berta et al. (2012) [38] (15.31, 89.30), respectively.

Method	$R_p/R_*$
Spitzer 4.5 $\mu\text{m}$	
Simultaneous	$0.1171 \pm 0.0002$
Averaged Individual	$0.1170 \pm 0.0003$
Phased & binned Best-fit orbital	$0.1171 \pm 0.0002$
Bean orbital	$0.1161 \pm 0.0003$
Berta orbital	$0.1160 \pm 0.0003$
Spitzer 3.6 $\mu\text{m}$	
Simultaneous	$0.1161 \pm 0.0003$
Averaged Individual	$0.1162 \pm 0.0001$
Phased & binned	
Best-fit orbital	$0.1160 \pm 0.0006$
Bean orbital	$0.1163 \pm 0.0002$
Berta orbital	$0.1161 \pm 0.0002$
TRAPPIST I+z band	
Simultaneous	$0.1187 \pm 0.0011$
Averaged Individual	$0.1179 \pm 0.0018$
Phased & binned	
Best-fit orbital	$0.1180 \pm 0.0005$
Bean orbital	$0.1177 \pm 0.0005$
Berta orbital	$0.1172 \pm 0.0005$

## Chapter 3: Water Vapor Absorption in the Clear Atmosphere of an exo-Neptune

### Abstract

We used the Kepler, Hubble, and Spitzer Space Telescopes to probe the atmosphere of the warm Neptune HAT-P-11b ( $M_p = 25.8 \pm 2.9M_{\oplus}$ ;  $R_p = 4.37 \pm 0.08R_{\oplus}$ ;  $T_{eq} = 878 \pm 50$  K) with transmission spectroscopy, constraining molecular absorption from water vapour. The detections, and non-detections, of molecular species such as water, methane, and carbon monoxide can lead to greater understanding of planet formation and evolution. Recent significant advances in both theoretical and observational discoveries from planets like HD189733b, HD209458b, GJ436b, and GJ1214b have shown that the range of measurable atmospheric properties spans from clear, molecular absorption dominated worlds to opaque worlds, with cloudy, hazy, or high mean molecular weight atmospheres. Planet formation models predict an inverse trend between planetary mass and density. This trend has been confirmed for medium and large planets; but there remains a degeneracy between the atmospheric density and core mass with small planets ( $R < 4R_{\oplus}$ ). This degeneracy can only be constrained with spectroscopic observations of these exoplanetary atmospheres. Exoplanetary clouds and hazes reduced the significance of these predicted

molecular detections from most of the small exoplanets with high-precision, spectroscopic observations. Our detection of molecular absorption from water vapour in the atmosphere of HAT-P-11b provides constraints on the atmospheric scale height, atmospheric metallicity, and water abundance that has evaded detection from most other small exoplanets to date. Understanding the source and prevalence of clouds or hazes in exoplanetary atmospheres, as well as detecting molecular features, is a necessary step forward for predicting the significance of future observations with the next generation of telescopes soon to become active.

### 3.1 Introduction

Transmission spectroscopy has thus far detected atomic and molecular absorption in Jupiter-sized exoplanets, but intense efforts to measure molecular absorption in the atmospheres of smaller (Neptune-sized) planets during transits have revealed only featureless spectra [19, 45, 48, 100]. From this it was concluded that the majority of small, warm planets evolve to sustain atmospheres with high mean molecular weights (little hydrogen), opaque clouds, or scattering hazes, reducing our ability to observe the composition of these atmospheres [18, 19, 45, 48, 100]. Here we report observations of the transmission spectrum of the exoplanet HAT-P-11b (which has a radius about four times that of Earth) from the optical wavelength range to the infrared. We detected water vapour absorption at a wavelength of  $1.4 \mu\text{m}$ . The amplitude of the water absorption (approximately 250 parts per million) indicates that the planetary atmosphere is predominantly clear down to an altitude corre-

sponding to about 1 mbar, and sufficiently rich in hydrogen to have a large scale height. The spectrum is indicative of a planetary atmosphere in which the abundance of heavy elements is no greater than about 700 times the solar value. This is in good agreement with the core-accretion theory of planet formation, in which a gas giant planet acquires its atmosphere by accreting hydrogen-rich gas directly from the protoplanetary nebula onto a large rocky or icy core [101].

Planet formation models predict an inverse trend between planetary mass and density, for planets with  $M_p < M_{Jup}$  [52]. It implies that larger core mass protoplanets are able to accrete larger fractions of hydrogen, which would decrease atmospheric mean molecular weights and increase scale heights. Inversely, small core mass protoplanets should only be able to accrete small fractions of hydrogen, increasing the atmospheric mean molecular weights and decreasing scale heights [5,52]. This trend has been confirmed for medium and large planets [22]; but there remains a degeneracy between the atmospheric density and core mass with small planets ( $R < 4R_{\oplus}$ ). This implies that for a given radius and mass, comparing observations to a set of bulk density models, we cannot uniquely define the internal structure of small exoplanets. This degeneracy can only be resolved with spectroscopic observations of these exoplanetary atmospheres to measure scale heights and constrain atmospheric mean molecular weights. Exoplanetary conditions – such as clouds, hazes, or a high mean molecular weight atmospheres – reduce the significance of these predicted molecular detections from most of the small exoplanets with robust, high-precision, spectroscopic observations. Our detection of water vapour from HAT-P-11b provided the first constraint of scale height and mean molecular

weight for an exoplanet with a radius and mass less than Saturn.

## 3.2 Observations

We observed transits of HAT-P-11b [102] ( $M_p = 25.8 \pm 2.9M_\oplus$ ;  $R_p = 4.37 \pm 0.08R_\oplus$ ;  $T_{eq} = 878 \pm 50$  K) in a joint programme involving NASA’s Hubble and Spitzer space telescopes. Our Hubble observations comprised 1.1-1.7  $\mu m$  grism spectroscopy using the Wide Field Camera 3 (WFC3) in spatial scanning mode. We also integrated these data over wavelength to produce WFC3 photometry [19,33,45,48,100]. Our Spitzer observations comprised photometry during two transits in each of the 3.6 and 4.5  $\mu m$  bands of the Infrared Array Camera (IRAC) [103]. Because the planet lies in the field of view of NASA’s Kepler spacecraft [55], precision optical photometry ( $\sim 642$  nm) was obtained simultaneously with our Spitzer observations, although not simultaneously with our Hubble observations. Table 3.1 summarizes specific details of our observations, and Figure 3.1a shows our transit photometry and model fits.

Because HAT-P-11 is an active planet-hosting star [61,106,107], we show that starspots on the stellar surface are not sufficiently cool, nor sufficiently prevalent, to mimic the effect of water vapour absorption in the planet (see below) [105]. Our simultaneous Spitzer and Kepler photometry were critical to defining the temperature of the starspots that could otherwise, potentially mimic the effect of water vapour absorption in the planetary atmosphere.

We observed two transits of HAT-P-11b using Hubble Space Telescope (HST)

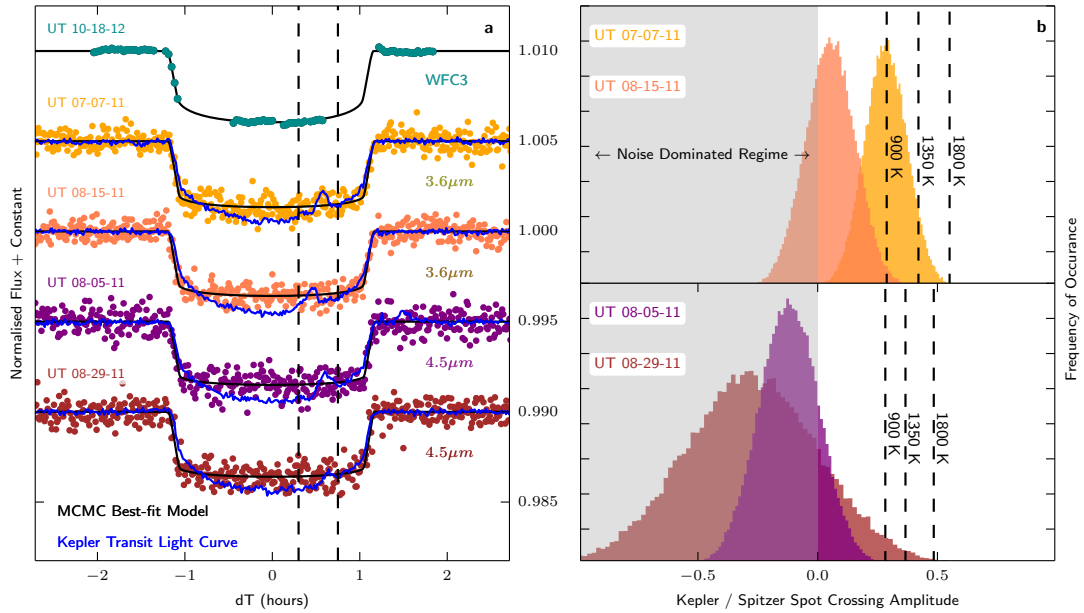


Figure 3.1: White light transit curves and starspot crossing temperature estimates. a, Transit curves from HST-WFC3 and warm Spitzer, aligned in phase and shifted in flux for clarity. The four warm Spitzer transits at both  $3.6 \mu\text{m}$  and  $4.5 \mu\text{m}$  [103] are binned for illustration. Starspot crossings are seen as deviations near  $+0.5$  hours in the Kepler photometry (dark blue). b, We estimated the starspot temperatures by dividing the Spitzer transit residuals by the Kepler transit residuals. The dashed lines represent the photosphere-to-starspot temperatures for three stellar model atmospheres [104]. Water vapour was detected in sunspots as cool as 3000 K, corresponding to a contrast of  $\sim 1800$  K here [105]. There is essentially no starspot temperature that can produce sufficiently strong water absorption to mimic our result.

spectroscopy near  $1.4 \mu\text{m}$ , and we obtained photometry for two transits at  $3.6 \mu\text{m}$  and two at  $4.5 \mu\text{m}$  using warm Spitzer. We also analysed 208 archival Kepler transits to assess the effect of starspots and update the optical transit depth [61]; Kepler observed HAT-P-11 during our Spitzer, but not HST, observations.

Date (ut)	Start time	End time	Observatory (instrument)	Band pass ( $\mu\text{m}$ )	Spectral resolution	Cadence (s)	Number of observations
7 Jul. 2011	23:11:42	06:37:52	Warm Spitzer (IRAC Channel 1)	3.6	$\sim 4$	0.4	62,592
5 Aug. 2011	07:02:48	14:28:58	Warm Spitzer (IRAC Channel 2)	4.5	$\sim 4$	0.4	58,112
15 Aug. 2011	01:49:20	09:15:30	Warm Spitzer (IRAC Channel 1)	3.6	$\sim 4$	0.4	52,633
29 Aug. 2011	17:37:18	01:03:28	Warm Spitzer (IRAC Channel 2)	4.5	$\sim 4$	0.4	62,592
18 Oct. 2012	17:37:18	01:03:28	Hubble (WFC3 G141)	1.13–1.64	$\sim 60\text{--}89$	123	113
24 Dec. 2012	23:56:56	03:05:58	Hubble (WFC3 G141)	1.13–1.64	$\sim 60\text{--}89$	123	99

Table 3.1: **Summary of observations.** We observed HAT-P-11b during four warm Spitzer observations, two transits at both 3.6 and 4.5  $\mu\text{m}$ s with the IRAC instrument [103], and two observations using HST WFC3 G141 grism spectrometer, spanning 1.1-1.7  $\mu\text{m}$ . Concurrent Kepler observations were retrieved for comparison with our warm Spitzer observations, but were unavailable for our Hubble spectroscopic observations.

### 3.2.1 Hubble WFC3 Spectroscopy and White Light Photometry

We observed HAT-P-11 using the HST Wide Field Camera 3 (WFC3) in spatial scan mode (Table 3.1). We used the G141 grism, with a binned, four-column spectral resolution from  $R = 60 - 89$  over the wavelength range 1.1-1.7  $\mu\text{m}$ . Gaps in the HST observations (Figure 3.2) occur every  $\sim 45$  min during occultations of the Earth.

We scanned the spectrum in the cross-dispersion direction to maximize efficiency [33, 108]. Each scan covered 135 pixels in 44 seconds ( $\sim 0.3981'' s^{-1}$ ), yielding  $\sim 45,000$  electrons per pixel ( $\sim 70\%$  of saturation). The average, photon-limited signal-to-noise ratio is  $\sim 220$  per pixel, integrating to a signal-to-noise ratio of  $\sim 2,500$  per column, for 113 spectral images in transit 1. We were unable to use the second transit because HST’s fine guidance sensors lost positional stability, which is not uncommon in this observing mode [33, 45]. This also occurred eight times during

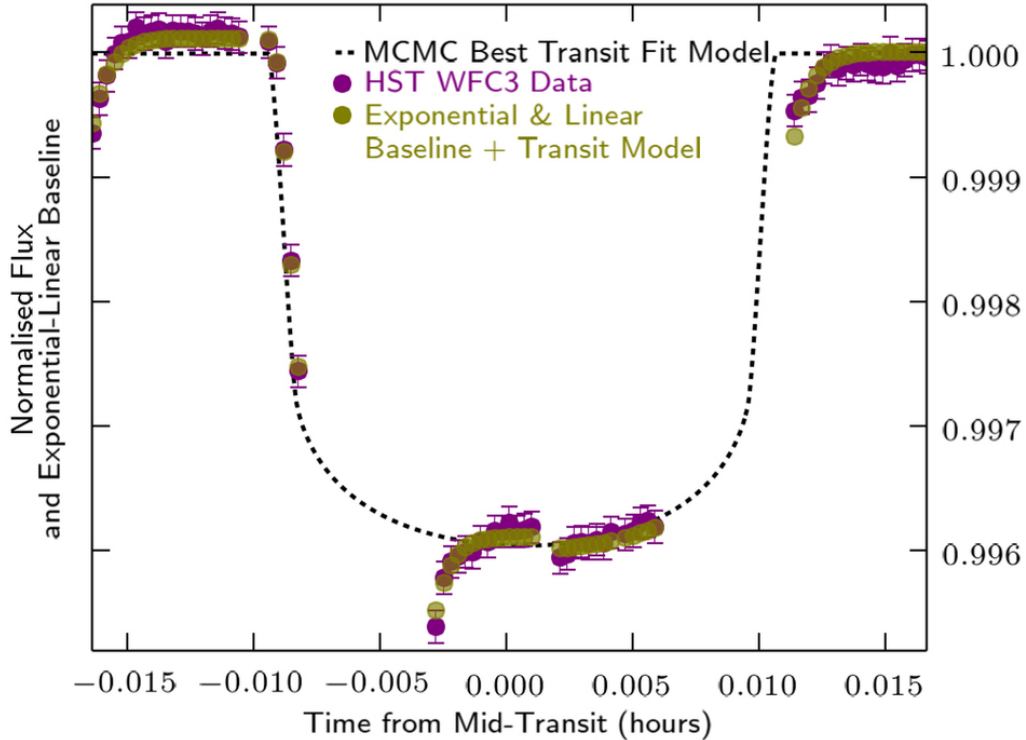


Figure 3.2: HST White Light Curve with exponential ramp effects. The gaps resulted when HAT-P-11 was occulted by the Earth during Hubble’s  $\sim 96$  minute orbit. We decorrelated the exponential ramp effect by fitting an average, 2-parameter (scale and amplitude) exponential profile as a function of HST’s orbital phase.

transit 1. We further removed the entire first orbit and the first image of each orbit – a common practice to ameliorate instrumental effects [33, 38, 65] – yielding 72 images for photometric and spectroscopic measurement.

### 3.2.2 Warm Spitzer IRAC

Spitzer transits were critical to establish that starspots on HAT-P-11 are not sufficiently cool to exhibit stellar water absorption masquerading as planetary atmospheric absorption. Spitzer also provided a long-wavelength baseline for the plane-

tary radius, minimizing the effect of Rayleigh scattering while remaining sensitive to absorption from carbon-containing molecules such as methane and carbon monoxide.

### 3.2.3 Kepler Archival Transits

We used all 208 archival transits of HAT-P-11 that Kepler observed at  $\sim 0.6 \mu\text{m}$ . The out-of-transit photometry yielded constraints on the disk-integrated activity of the host star (Figure 3.3). We re-fitted the phased and binned Kepler light curve that was analysed previously [61,107], using fourth-order limb-darkening coefficients from [109] to improve the optical radius and geometric parameters of the system (see Table 3.2). The occurrence of the 298 starspot crossings allowed us to characterise the amplitude distribution of spots crossed by HAT-P-11b during transit (see Figure 3.4).

## 3.3 Data Analysis

### 3.3.1 Limb-Darkening Coefficients

We used a single set of planetary orbital parameters for all observations – derived from our Kepler analysis – with wavelength-dependent, four-parameter, non-linear limb-darkening coefficients (LDCs) [90,112]. For the Kepler photometry, the WFC3 band-integrated photometry, and the Spitzer photometry, we computed the LDCs by integrating stellar model intensities [113] over each instrument’s response function. For the 128 individual wavelength channels (columns) from the WFC3

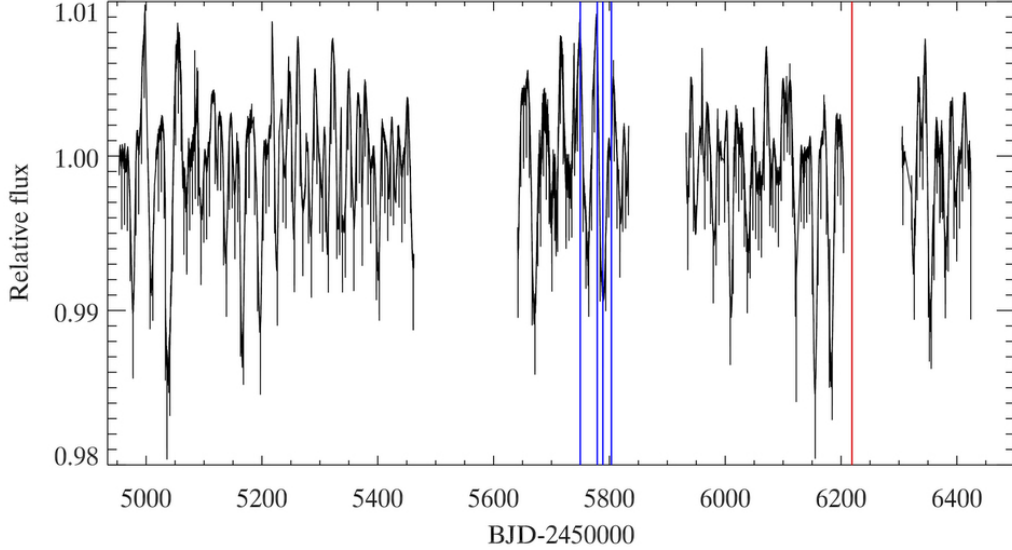


Figure 3.3: HAT-P-11 Kepler light curve for  $\sim 4$  years of short cadence. The variation in flux has a  $\sim 2\%$  peak-to-peak modulation, consistent with the spot coverage inferred from the previous Kepler study [61]. The times of our Spitzer observations are marked with vertical blue lines. The time of our HST WFC3 observation, included in this analysis, are marked with vertical red lines.

grism, we used the intersection of the WFC3 response function and a one-column (4.71 nm) square window centered at each wavelength channel (column). We held the computed LDCs constant during subsequent analyses.

We represented HAT-P-11 using an ATLAS model [113] with a stellar effective temperature of  $T_{eff} = 4,750$  K,  $[M/H] = +0.3$  and  $\log g = 4.5$  [102]. To ensure that our exoplanetary spectrum is not sensitive to the stellar parameters, we also derived it using LDCs with  $T_{eff} = 4,500$  K and  $T_{eff} = 5,000$  K. Both the exoplanetary spectrum and the white light (band-integrated) transit depth varied negligibly ( $\sim 1$  and  $\sim 5$  ppm, respectively) between the three stellar models. Repeating our analysis

	Kepler	HST WFC3	Spitzer IRAC1 UT 07-07-11	Spitzer IRAC1 UT 08-15-11	Spitzer IRAC2 UT 08-05-11	Spitzer IRAC2 UT 08-29-11
Wavelength ( $\mu\text{m}$ )	0.641	1.419	3.521	3.521	4.471	4.471
Period (days) <sup>*</sup>	4.8878018 $\pm 7.1 \times 10^{-6}$	--	--	--	--	--
$T_{\text{center}}$ (HJD <sub>UTC</sub> ) <sup>†</sup>	54811.1786727 $\pm 0.0000082$	54811.1785254 $\pm 0.0000663$	54811.1791713 $\pm 0.0001272$	54811.1788248 $\pm 0.0001239$	54811.1790119 $\pm 0.0001541$	54811.1789256 $\pm 0.0001591$
Inclination ( $^{\circ}$ ) <sup>‡</sup>	89.549 $\pm$ 0.114	--	--	--	--	--
$b^{\text{c}}$ (impact parameter)	0.135 $\pm$ 0.034	--	--	--	--	--
$a / R_s^{\ddagger}$	17.125 $\pm$ 0.060	--	--	--	--	--
$R_p / R_s^{\S}$	0.05852 $\pm 0.00007$	0.05887 $\pm 0.00025$	0.05849 $\pm 0.00025$	0.05785 $\pm 0.00033$	0.05762 $\pm 0.00033$	0.05837 $\pm 0.00032$
Transit Depth <sup>‡</sup> (ppm)	3424 $\pm$ 8	3466 $\pm$ 29	3421 $\pm$ 29	3347 $\pm$ 29	3321 $\pm$ 38	3407 $\pm$ 37
$c1^{\parallel}$	0.7547 $\pm$ --	0.6718 $\pm$ --	0.5750 $\pm$ --	0.5750 $\pm$ --	0.6094 $\pm$ --	0.6094 $\pm$ --
$c2^{\parallel}$	-0.9164 $\pm$ --	-0.1618 $\pm$ --	-0.3825 $\pm$ --	-0.3825 $\pm$ --	-0.7325 $\pm$ --	-0.7325 $\pm$ --
$c3^{\parallel}$	1.6411 $\pm$ --	0.2855 $\pm$ --	0.3112 $\pm$ --	0.3112 $\pm$ --	0.7237 $\pm$ --	0.7237 $\pm$ --
$c4^{\parallel}$	-0.6328 $\pm$ --	-0.1551 $\pm$ --	-0.1099 $\pm$ --	-0.1099 $\pm$ --	-0.2666 $\pm$ --	-0.2666 $\pm$ --
Eccentricity <sup>¶</sup>	0.232 $\pm$ 0.054	--	--	--	--	--
Longitude of Periastron <sup>¶</sup>	7 $^{\circ}$ $\pm$ 25 $^{\circ}$	--	--	--	--	--

Table 3.2: The system and planetary parameters of HAT-P-11b.

-- Value held constant for all MCMC chains

<sup>a</sup>Deming et al. 2011 [61]

<sup>b</sup>Eastman et al. 2010 [110]

<sup>c</sup>Derived from MCMC posteriors over our phased and binned Kepler transit.

<sup>d</sup>Transit depths are uncorrected for stellar activity.

<sup>e</sup>Derived from ATLAS models

<sup>f</sup>Knutson et al 2014c [111]

with both quadratic and three-parameter limb-darkening laws, we found similarly negligible effects:  $\sim 1$  ppm (differential) and  $\sim 10$  ppm (absolute).

(<http://kurucz.harvard.edu/grids.html>)

### 3.3.2 Hubble Wide Field Camera 3

Each WFC3 spatial scan comprised six nondestructive reads, with 7.35 seconds of exposure per read. We combined them by subtracting each read from the

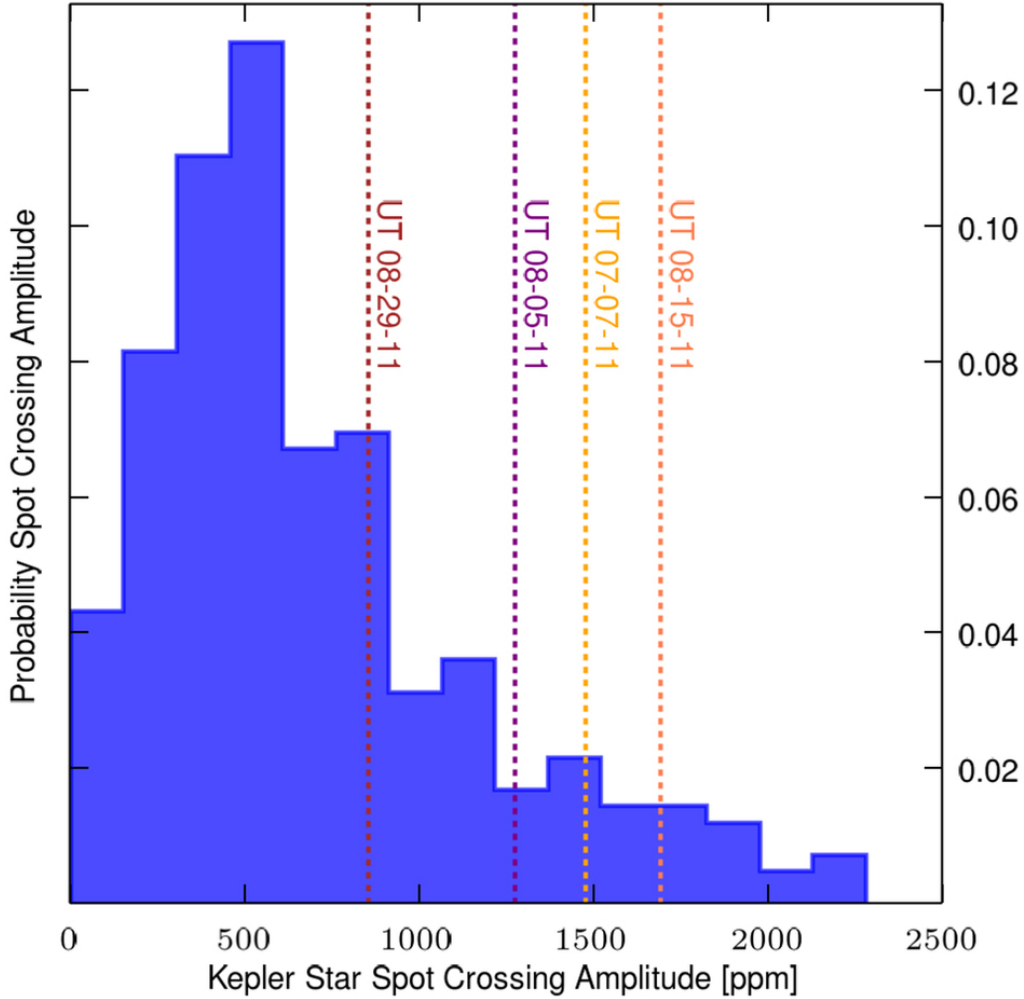


Figure 3.4: The distribution of Kepler starspot crossing anomalies. We fit a Gaussian profile to each of the 298 spot crossings observed during the 208 transits observed by Kepler. Here we show the distribution of starspot amplitudes, calculated as the height - baseline of the fitted Gaussian profile in parts-per-million. The dashed lines represent the starspot crossing amplitudes observed during our 4 concurrent Spitzer observations. In particular, note that all 4 spot crossings with concurrent Spitzer observations are on the larger end of the distribution. In addition, the spot crossing on UT 07-07-11 – the largest temperature contrast detected during our concurrent Spitzer observations– crossed a spot with  $\Delta T \sim 900$  K.

previous read, applying a spatial mask to the difference and adding all of the masked differences to an initially blank image to create the spectral frame [33, 48, 61]. We

used edge detection algorithms [114] to determine the edges of each combined image in the scanning direction and masked all pixels within 20 pixels of these edges in the scanning direction, to keep sky background and other noise from accumulating in the final spectral image. We identified bad pixels in the spectral images using a median filter with a  $4\sigma$  threshold, over a seven-pixel temporal window, and assigned bad pixel values to the median of the window. Figure 3.5 shows a spectral frame from the first Hubble transit observational epoch, displaying the spectral (dispersion) and spatial (cross dispersion) dimensions. The curves in Figure 3.5b show the averaged, column-integrated spectral template (red), before (top) and after (bottom) being fitted to the example spectrum (blue), to measure both the wavelength solution and the white light photometry as a function of time.

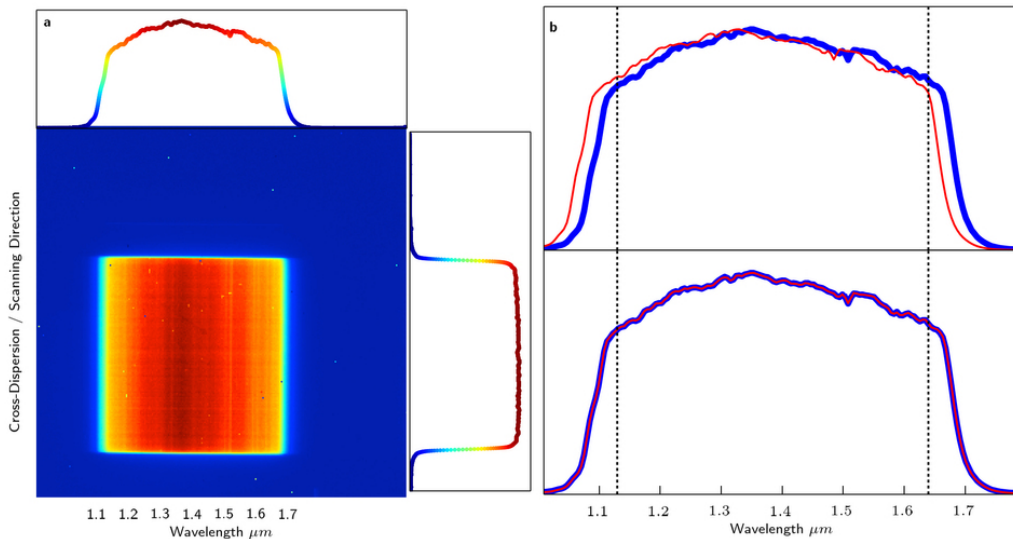


Figure 3.5: An example of WFC3 scanning mode observation spectral images. a, Example spatial scan spectral image with the normalised summations in the dispersion (upper) and cross-dispersion (scanning; right) directions. b, Integrated spectrum (blue) and spectral template (red) before (top) and after (bottom) fitting; the amplitudes and colors are normalised to 1.0.

We calculated the wavelength flat-field calibration using standard procedures [115]. We fitted a two-dimensional Gaussian to the spectral images, and found that the spectra shifted by at most 1.12 pixels in the wavelength direction; we corrected this shift during the template fitting described below. The final, column-integrated spectra were derived by dividing each raw spectral image by its corresponding flat field and subtracting the per-column background values. We then integrated the spectra in the cross-dispersion direction (down the columns).

The sky background was calculated per-column as the median of the portion of the spectral image not scanned by the instrument. In Figure 3.5a, this corresponds to the blue regions above and below the red/orange spectral information. The background values varied by  $< 3\%$  from 1.1 to 1.7  $\mu m$ , but were uncorrelated with the resultant planetary spectrum [114].

To derive the WFC3 spectrum for HAT-P-11b, we used the established technique of spectral template fitting [19, 33, 48, 65]. We formed the spectral template by averaging the out-of-transit spectra, and fitted it to individual grism spectra in both wavelength and amplitude [114], using both LevenbergMarquardt and spline interpolation algorithms [114]. The fitted amplitudes as functions of time yield the band-integrated white light curve (WLC) (Figure 3.2). The WLC defines the average transit depth over the total WFC3 spectroscopic band pass.

### 3.3.2.1 WFC3 Exponential and Linear Instrumental Noise Profiles

The raw HST-WFC3 WLC contained both the transit and instrumental noise profile, which took the form of exponential ramps throughout each orbit, as well as a linear trend throughout each visit [19, 33, 38, 45]. We simultaneously fitted for exponential parameters as a function of HST’s orbital phase,  $E_R(\theta; A, S)$ , a linear trend as a function of time,  $L(t; m, b)$ , and an additive offset for the second half of the in-transit data,  $O(t_i; \theta, O_o)$  ( $i \in \{0, 1, \dots, 113\}$ ) (see below), with an analytic transit light curve [88],  $MA(t; p, T_c, P, b, a, u_1, u_2, u_4, u_4)$ :

$$E_R(\theta; A, S) = 1 + A e^{S \cdot (\theta_i - \theta_{min})} \quad (3.1a)$$

$$O(t_i; \theta, O_o) = O_o \delta(\theta_i - \theta'_{\frac{1}{2}}) \chi(t_i) \quad (3.1b)$$

$$L(t; m, b) = m (t_i - t_o) + b \quad (3.1c)$$

$$Model = MA(t; p, T_c, P, b, a, u_1, u_2, u_4, u_4) E_R(\theta; A_o, S_o) L(t; m, b) + O(t_i; \theta, O_o) \quad (3.1d)$$

Here  $\theta$  represents HST’s orbital phase,  $\{A, S\}$  are the exponential amplitude and scale factor, and  $\{m, b\}$  are the slope and intercept of the linear function.  $O(t_i; \theta, O_o)$  is a small ( $\sim 100 \pm 50$  ppm) step function,  $\chi(t_i)$ , correcting an unexplained offset in the band-integrated photometry, starting at  $\theta'_{\frac{1}{2}} \sim 0.2$  (see Figure 3.2 between phases 0.2 and 0.7). The offset is likely related to a small shift in the position of the spectrum that does not occur in the other HST orbits. Including the offset in our model improved the WLC fits significantly, without degrading the Bayesian

information criterion (BIC) or altering the significance of the water detection. The BIC is a metric to statistically compare multiple models by penalizing the addition of parameters, which would otherwise reduce  $\chi^2$  intrinsically. If  $\Delta BIC < 2$ , then the model with more parameters is permissible to utilize as our instrument noise model [75, 116].

$$BIC = \chi^2 + k \ln N \quad (3.2)$$

We tested four different models for WFC3’s WLC exponential baseline [33, 38, 75], and selected among them on the basis of the BIC. The BIC for our adopted model differed only slightly from optimum ( $\Delta BIC \ll 2$ ) [75, 116], but the transit depth was more physically realistic when compared to atmospheric models. WFC3 WLCs are known to have noticeable red noise [19, 33, 65]; to constrain this effect, we implemented an additional wavelet analysis to include both the white noise ( $\sigma_w = 12.81$  ppm) and the red noise ( $\sigma_r = 61.89$  ppm) components of the residuals into our final uncertainties [117].

We used a MCMC procedure [118] to fit the transit and instrument parameters simultaneously, thereby incorporating correlations between parameters into our reported uncertainties. Figure 3.6 compares the posteriors graphically. The Pearson correlation coefficient over each parameter showed the correlations to be insignificant ( $-0.10 < \max_{i,j}(P) < 0.10 \forall i, j \in \{\text{fitted parameters}\}$ ).

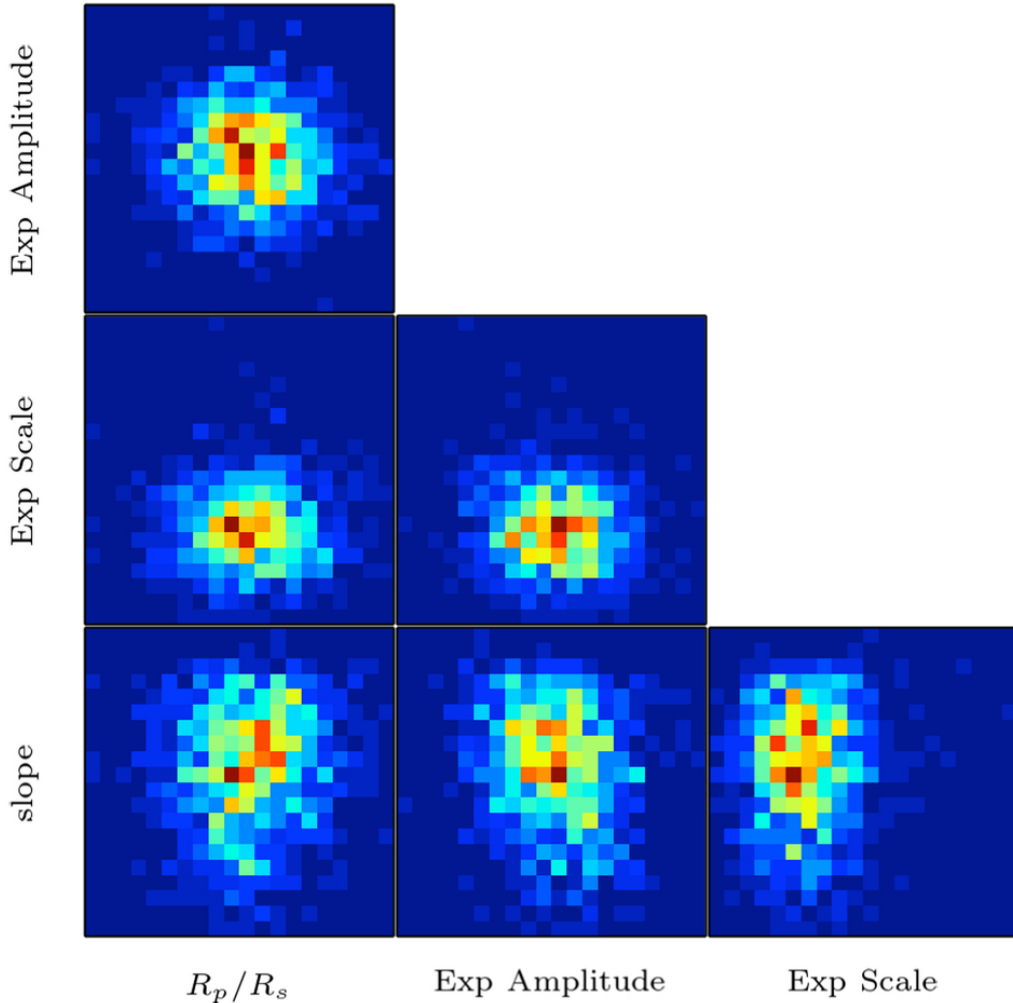


Figure 3.6: Correlations between all exponential ramp parameters for our HST WFC3 White Light Curve. We calculated the Pearson correlation coefficient over the posteriors of each parameter, and found the correlations to be small ( $< \pm 0.10$ ), or in most cases negligible ( $|P| < \pm 0.01$ ). Blue represents regions of lesser posterior density and the Red represents regions of greater posterior density, with green and yellow in the middle.

### 3.3.2.2 Deriving the HST WFC3 Exoplanet Spectrum

We calculated the planetary spectrum differentially relative to the WLC, by dividing the spectral template,  $S_{\lambda,T}$ , into each individual spectrum  $S_{\lambda}(t)$  (calculating

$S_\lambda(t)/S_{\lambda,T}$ ), allowing for small wavelength shifts ( $< 1.12$  pixels). The planetary spectrum,  $P_\lambda$ , is derived from the normalized residuals, or differential light curves:

$$DLC_\lambda(t_i) = (S_\lambda(t_i) - S_{\lambda,T}(t_i))/S_{\lambda,T}(t_i) \quad (3.3)$$

We fitted the  $DLC_\lambda(t_i)$ , with differential analytic light curves,  $DALC(t_i)$ , by renormalising the analytic WLCs [88],  $MA(t_i)$ , as

$$DALC(t_i) = \frac{(MA(t_i) - \max_t MA(t_i))}{(\max_t MA(t_i) - \min_t MA(t_i)) + \max_t MA(t_i)} \quad (3.4)$$

(where the minima and maxima are taken over the time domain.)

We fitted for the normalisation amplitude,  $P_\lambda$ , of the DALCs, simultaneously with wavelength-dependent linear trends, using linear matrix inversion

$$DLC_\lambda(t_i) = P_\lambda DALC(t_i) + m_\lambda (t_i - t_o) + b_\lambda = \begin{pmatrix} DALC(t_i) \\ t_i - t_o \\ 1 \end{pmatrix}^T \begin{pmatrix} P_\lambda \\ m_\lambda \\ b_\lambda \end{pmatrix} \quad (3.5)$$

Figure 3.7 shows all 32 wavelength dependent light curves (blue to red) and corresponding analytic light curves (black) ranging from 1.167 to 1.675  $\mu m$  with 18 nm spacing in wavelength. We used the linear matrix fits as initial conditions for MCMC chains to probe posterior distributions for each wavelength, forming the final planetary spectrum  $P_\lambda$  shown in Figure 3.8b and detailed in Table 3.3. The DALCs were modified to include wavelength-dependent limb darkening profiles described above. Our analysis also included smoothing in wavelength with a triangle function

to reduce the effect of known spectral undersampling from the WFC3 detector [19, 33, 48]. The full-width at half-maximum of the smoothing triangle was four columns, resulting in 32 DLCs at a spectral resolution of  $R \approx 75$  (see Figure 3.7).

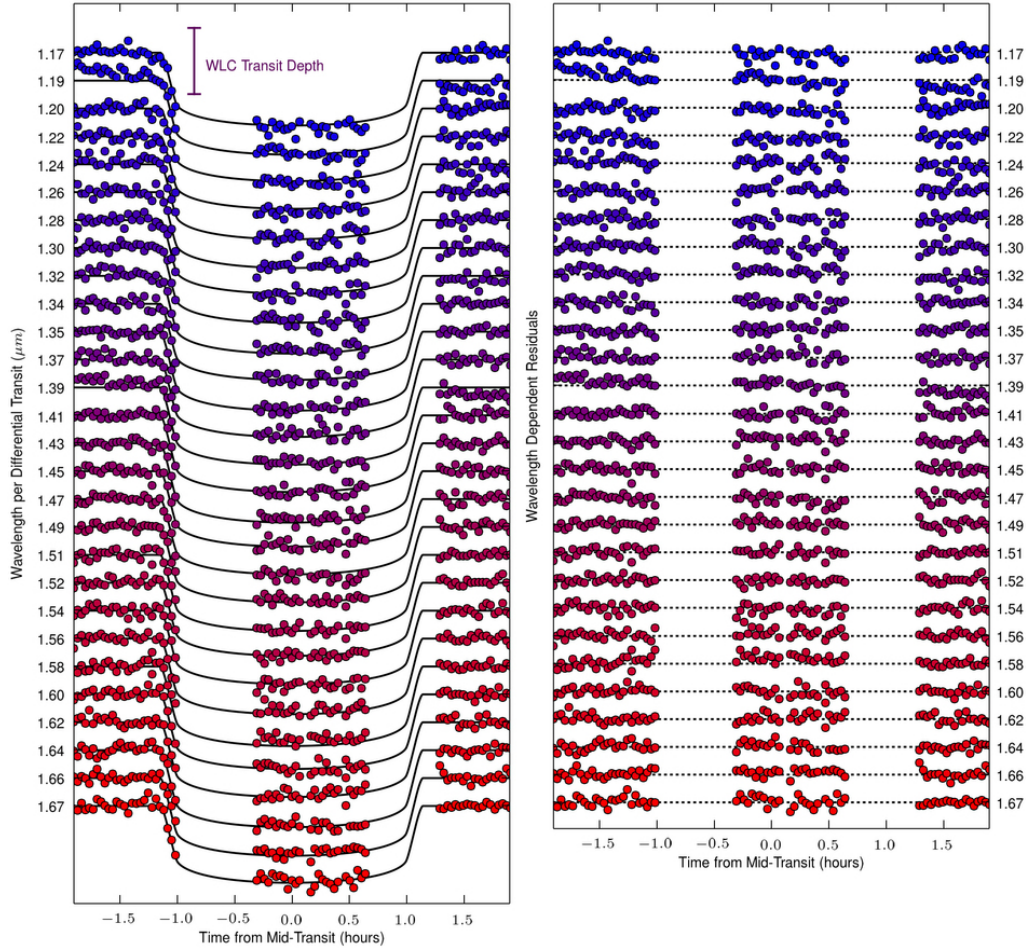


Figure 3.7: Wavelength Dependent Transit Light Curves. The coloured points are the wavelength light curves, ranging from blue ( $1.17 \mu m$ ) to red ( $1.67 \mu m$ ) with 18 nm spacing. The black lines represent the best-fit transit light curves over the wavelength range from 1.1 to  $1.7 \mu m$ . The curves are shifted for display purposes only. The differential light curves were fit with differential analytic transit curves to derive the planetary spectrum seen in Figure 3.1. We added the white light curve into the differential light curves to derive the data above.

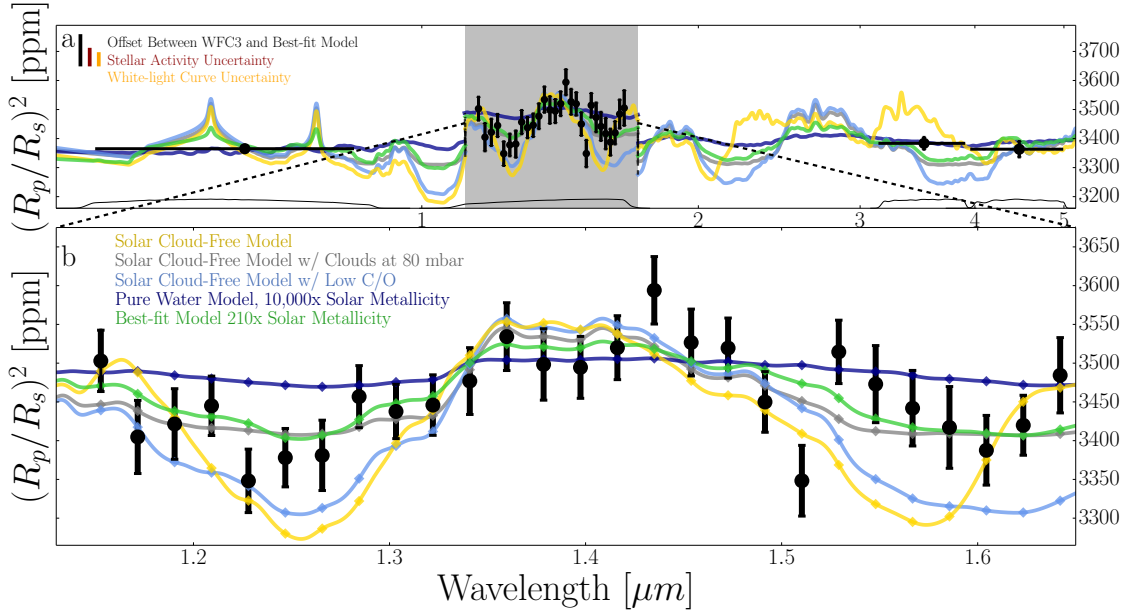


Figure 3.8: The transmission spectrum of HAT-P-11b. a, Our WFC3 observations show a transit depth variations in agreement with a hydrogen-dominated atmosphere. The coloured, solid lines [9, 10] correspond to matching markers displayed in Figure 3.8. The error bars represent the standard deviations over the uncertainty distributions. High mean molecular mass atmospheres (dark blue line) are ruled out by our observations by  $> 3\sigma$ . The WFC3 spectrum was allowed to shift within the WFC3 regime (grey region), as a unit, over these uncertainties induced by unconstrained stellar activity. b, Detailed view of our WFC3 spectrum. For the purposes of visually comparing the spectral significance, we shifted all of the models by 93ppm in the grey region and bottom panel.

### 3.3.3 Warm Spitzer IRAC

We performed aperture photometry on the Spitzer images (Table 3.1), after subtracting a background value determined as a median of the pixel values well away from the stellar image. We applied Pixel Level Decorrelation (PLD; [64]) – a basis

vector analysis to decorrelate Spitzer photometry – to the subsequent photometry to decorrelate the well-known Spitzer intrapixel effect [36, 58, 62, 63, 86, 119]. We tested this decorrelation method on both published and unpublished Spitzer exoplanet eclipses, and found that it consistently reduced both the BIC and red-noise by comparison with previous methods [58, 62–64, 86, 119]. Our basis vector algorithm fits linear coefficients to the nine pixel values centered at and surrounding the stellar point spread function over time [36, 64]:

$$Flux(t) = a^{-1}(t) \sum_n a_n pixel_n(t); n = 1, \dots, 9 \quad (3.6)$$

where  $a(t)$  is the normalisation for each  $3 \times 3$ -pixel box as a function of time. Our Spitzer fitting simultaneously solved for the transit depth and amplitudes of starspot crossings, by scaling the more precise (and strictly simultaneous) Kepler spot crossings as described below.

### 3.3.4 Kepler Archival Observations

We used the Kepler data for two completely independent purposes [55]. We first derived an improved optical transit depth and geometric parameters (see Table 3.2). Then we characterised the behaviour of starspots on HAT-P-11 (see discussion below).

To improve the optical transit depth derived in [61], we used all four years of Kepler data Q0-Q16, incorporating fourth-order limb darkening in the analysis. We detrended the stellar variations by fitting linear trends to the normalized fluxes

within one transit duration of first and fourth contacts ( $T_1$  &  $T_4$ ). After dividing by linear baselines centered at each transit, we phase-folded all 208 short-cadence Kepler archival transits into a single, very high precision transit having 60 second time resolution. We fitted an analytic transit model [88] to this phase-folded light curve, including the LDCs described above, and to orbital parameters from radial-velocity measurements [110]. This determined both the transit depth and the geometric parameters (i.e. impact parameter) to high precision. All of the values were within  $1\sigma$  of the original analysis [61], but now followed the same limb-darkening model as all of our observations.

Figure 3.1a shows the binned and normalized light curves of our four simultaneous Kepler-Spitzer transits and our WFC3 (band-integrated) transits. We fitted analytic transit light curves to our light curves with PyMC [118] to generate Markov chain Monte Carlo (MCMC) distributions and estimate the planetary parameters [66, 67]. We reanalysed the phased and binned Kepler data using improved limb-darkening coefficients derived from stellar model atmospheres [113]. To fit the Spitzer and WFC3 transits, we held the orbital distance and inclination constant at our Kepler derived values. Although the uncertainties in the Kepler derived parameters were smaller than in previous studies [61, 107], our purpose was to implement the updated limb-darkening law and derive orbital parameters for all of our observations.

## 3.4 Discussion

### 3.4.1 Detection of Water Vapor Absorption in the Clear Atmosphere of an exo-Neptune

Figure 3.8 shows our HAT-P-11b transmission spectrum with Kepler, WFC3 and Spitzer transits combined. We constrain the atmospheric composition using the SCARLET tool (discussed below), which is a new version of the Bayesian retrieval framework described in previous studies [9, 10]. Our primary results are a robust  $5.1\sigma$  detection of water absorption in the WFC3 data and a  $3\sigma$  upper limit on HAT-P-11b’s atmospheric metallicity (the proportion by mass of elements heavier than hydrogen and helium) of  $\sim 700$  times the solar metallicity [18], corresponding to a mean molecular weight of  $\sim 10.2$  g/mol at the 10 mbar level (Figure 3.9). Transmission spectra of selected atmospheric models [2, 9, 10, 120] are plotted for a comparison with the observations in Figure 3.8, with colour-matched symbols in Figure 3.9. Although the significance of the water vapour detection is unaffected by uncertainties in the stellar activity because all wavelengths in the water band are measured simultaneously, this uncertainty made it prohibitively difficult to place robust constraints on the methane and carbon dioxide abundances and, therefore, the C/O ratio of HAT-P-11b’s atmosphere [120].

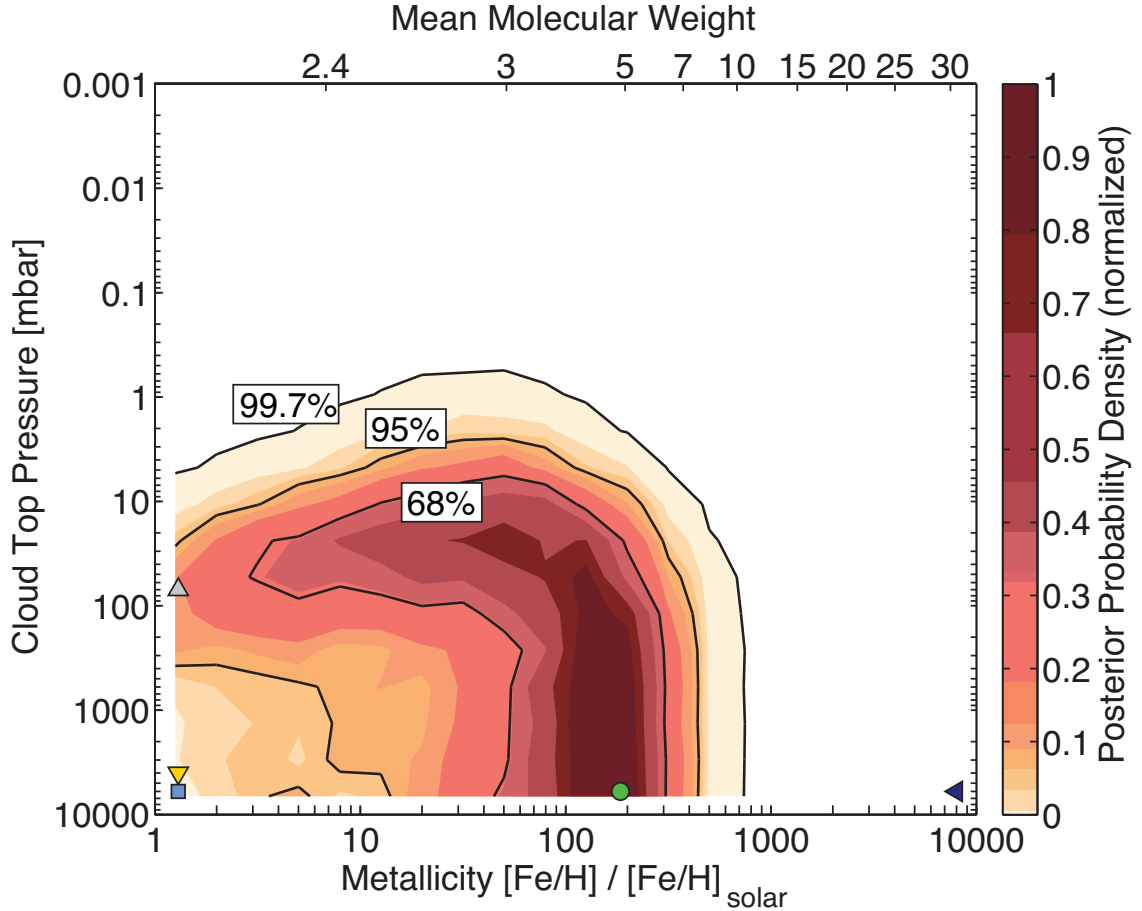


Figure 3.9: Spectral retrieval results of our transmission spectrum. The coloured regions indicate the probability density as a function of metallicity (the abundance of heavy elements relative to solar) and cloud top pressure derived using our Bayesian atmospheric retrieval framework [9, 10]. Mean molecular weight was derived for a solar C/O ratio at 10 mbar. Black contours mark the 68%, 95%, and 99.7% Bayesian credible regions. The depth of the observed water feature in the WFC3 spectrum required the presence of a large atmospheric scale height that can only be obtained self-consistently with an atmospheric metallicity below 700 times solar at  $3\sigma$  (99.7%) confidence. The atmosphere is likely predominately cloud-free at least down to the 1 mbar level. We indicate the matching models plotted in Figure 3.7 with coloured markers.

### 3.4.2 The Nature of Starspots on HAT-P-11

HAT-P-11b crosses starspots on virtually every transit [61, 107], as seen prominently Figure 3.1a. Our WFC3 photometry has the sensitivity to detect starspot crossings [45], but none were observed when Hubble observed the system. Our WFC3 observations contain large temporal gaps because Hubble passes behind the Earth [19, 33, 38, 45, 48, 100], but not during the transit. Therefore, unocculted starspots, rather than occulted ones, potentially affect our transmission spectrum [36, 42]. When the planet blocks unspotted portions of the stellar photosphere, the absorption lines (including water vapour lines) in cool unocculted spots become relatively more prominent [61, 107].

Each of the Kepler light curves obtained concurrently with our Spitzer observations shows starspot crossings as deviations in the light curves between, 0.3 and 0.7 h after mid-transit. The amplitude of these deviations is a function of both the area and the temperature of the occulted spots [61, 107]. Because the Kepler and Spitzer photometry were concurrent, the relative intensity is independent of the starspots' areas. However, because the contrast between starspot temperature and the photosphere is a chromatic effect, the amplitude of these deviations varied with wavelength [36, 42]. The spot crossings are not obvious in the Spitzer data because thermal radiation produces a much smaller contrast between the stellar photosphere and spot fluxes in the infrared than in the optical. The ratio between the Spitzer and Kepler spot crossing amplitudes constrained lower limits on the starspot temperatures for the crossed starspots.

We included the relative shape of the spot crossings, sliced from each residual Kepler light curve, and scaled their amplitudes as free parameters in our MCMC analysis with our Spitzer transits. The distributions of the Spitzer/Kepler spot crossing amplitude ratios are shown in Figure 3.1b. The dashed black lines represent the predicted spot crossing amplitude ratios for given spot temperature contrasts. We calculated these temperatures by representing the spots using model stellar atmospheres at various temperatures [104]. Using  $\chi^2$  difference ( $\delta\chi^2$ ) tests, we indirectly detected spot crossings only at 3.6  $\mu m$  because only these Spitzer observations resulted in positive, bounded photosphere-to-spot temperature contrasts. The 4.5  $\mu m$  Spitzer observations are consistent with zero, or a non-detection at infrared wavelengths. These measurements, especially the non-detections, imply that the starspots crossed during each transit are too hot to mimic water vapour absorption features in the planetary spectrum (see Figure 3.1b) [61, 105].

The activity of HAT-P-11 [61, 102, 106, 107] produces variations in the total brightness of the star owing to the rotation of spots in and out of view, which changed the band-integrated transit depth measured at each epoch. If the relative stellar brightness at the epoch of each observation is known, then the white light transit depths can be corrected to a common value. Kepler measured HAT-P-11's relative brightness during all four Spitzer observations, but not during our WFC3 observation. The unknown stellar brightness during this observation introduced an additional uncertainty in our estimate of the WFC3 transit depth, relative to the Spitzer and Kepler observations, of  $\pm 51$  ppm. In Figure 3.8, the offset between the WFC3 spectrum and the best-fit model is  $\sim 93$  ppm, on average.

To determine the relative amplitude (Spitzer versus Kepler) of the spot crossings, we first measured their profiles in the Kepler transits as the residual of the individual Kepler light curves relative to the phased and binned model. We include the Kepler spot-crossing profile as a term in the MCMC fitting [66, 67, 118] to the Spitzer transits, fitting the spot crossing amplitude simultaneously with the transit parameters. Negative ratios are statistically possible here because of the low signal-to-noise ratio of the spot crossing profiles. We allowed our MCMC chains to probe these unphysically negative values of spot crossing amplitudes. In Figure 3.1b, the grey region represents the noise-dominated regime and the white region represents the physically relevant regime. Because the spot area crossed by the planet is the same for the simultaneous Spitzer and Kepler transits, the relative amplitudes can be converted to a color-temperature in Figure 3.1b.

To establish that the crossed spots are typical of the uncrossed ones, we fitted a Gaussian profile to each of the 298 Kepler starspot crossing profiles – during the 208 Kepler transits observed over four years – to determine the full distribution of the spot crossing amplitudes (Figure 3.4), as discussed below.

### 3.4.3 Constraining the Significance of Water Vapour in Starspots

The amplitude of the starspot effect that mimics exoplanetary absorption is given as  $f\epsilon\delta$  [33], where  $f$  is the fractional coverage of spots on the stellar disk,  $\epsilon$  is the depth of the transit, and  $\delta$  is the water vapour absorption line depth (relative to the spectral continuum) in the spatially resolved starspot spectrum, at the observed

spectral resolution. Because the planet’s orbit is not synchronous with the star’s rotation, spot crossings in the Kepler data were used to estimate a flux deficit of 0.0179 [61]. Accounting for the (small) optical intensity modulations of dark starspots lead to  $f = 0.02$ . We measured  $\epsilon = 0.0036$  directly with our WFC3 photometry (Figure 3.1a). Because we cannot obtain spatially resolved spectra of the starspots on HAT-P-11, we here estimate  $\delta$  from Phoenix model stellar atmospheres [104], using a relative temperature constraint for the starspots based on Figure 3.1b.

To establish that the spots occulted in our simultaneous Kepler and Spitzer photometry are typical of HAT-P-11, we plotted the distribution of spot crossing amplitudes over the entire set of Kepler photometric transits for HAT-P-11 (Figure 3.4). Spots on the disk of the star caused brightness variations as the star rotates. This variation had a peak-to-peak modulation of approximately 2%, consistent with the spot coverage inferred from our previous Kepler study [61]. The times of our Spitzer and WFC3 observations are indicated in Figure 3.3 by blue and red lines, respectively. Similarly, the spot crossing amplitudes during our Spitzer observations are identified in Figure 3.4 by the coloured, dashed lines. From this, we concluded that the total effect of spots on the disk of HAT-P-11 is approximately the same during our observations as during other times, and that spots crossed during our Spitzer observations are typical of the unocculted spots during our WFC3 observations.

Next we must determine  $\delta$ , the depth of the  $1.4 \mu m$  water absorption feature in the spectrum of starspots. We approximate the starspot spectrum as equivalent to a star of the same abundance and surface gravity as HAT-P-11, except at a

lower temperature. We examined PHOENIX model atmospheres that are enriched in oxygen by +0.3 in the log abundance [104] and convolved these spectra to the resolution of WFC3.

Even in the extreme case with a temperature contrast of 1800 K (Figure 3.1b), the Phoenix spectrum shows that  $\delta < 0.024$  at  $1.4 \mu m$ , yielding  $f\epsilon\delta < 2 \text{ ppm}$ , which is two orders of magnitudes less than the absorption we derived for the exoplanetary atmosphere. Because  $f$  and  $\epsilon$  are small, there is essentially no starspot temperature that can produce sufficiently strong water absorption to mimic our result, given our inferred values for  $f$  and  $\epsilon$ .

#### 3.4.4 Self-Consistent Atmospheric Retrieval for Exoplanets

We interpreted the observed transmission spectrum using a new variant of the atmospheric retrieval framework described in previous studies [9, 10]. The new SCARLET framework combined a self-consistent, line-by-line atmospheric forward model with the nested-sampling technique to efficiently compute the joint posterior probability distribution of the atmospheric parameters. We probed the multidimensional parameter space spanned by the atmospheric metallicity (the overall abundance of heavy elements), the C/O ratio, the cloud-top pressure, the planetary radius at the 1 bar level and the planetary Bond albedo.

For a given set of parameters, the atmospheric forward model self-consistently computed the molecular abundances in chemical equilibrium and the temperature pressure profile in radiative-convective equilibrium. Line-by-line radiative trans-

fer based on pre-calculated opacity look-up tables enabled us to model molecular absorption accurately for the entire range of compositions. We included Rayleigh scattering using the two-stream approximation. In this study, we included clouds as a grey opacity source that cut off the transmission of starlight below the parameterized cloud-top pressure.

We included the planetary Bond albedo as a free parameter to capture the uncertainty in the atmospheric composition introduced by the unknown albedo. For a given atmospheric composition, the Bond albedo introduced the dominant uncertainty in the planetary temperature profile, which (via the scale height) affects the relation between observed depths of the absorption features and the mean molecular mass.

The nested-sampling algorithm repeatedly invoked the atmospheric forward model to probe the agreement between model spectra and the observational data throughout the multidimensional parameter space. In total, several  $10^4$  self-consistent, line-by-line atmospheric models were computed. The algorithm was initiated by randomly sampling 1,000 active samples within the full multidimensional parameter space. The active samples then iteratively migrated towards the regions of high likelihood by replacing the lowest-likelihood active sample, that is, the worst fit to the observations, with a new, better-fitting random sample [10]. The algorithm obtained convergence once the logarithm of the Bayesian evidence,  $Z$ , computed from the active sample no longer changed by more than  $\Delta(\log Z) = 0.0001$ . The algorithm is robust to multimodal posterior distributions and highly elongated curving degeneracies frequently encountered in exoplanet atmospheric retrieval studies [10].

Figure 3.9 shows that constraints on the atmospheric metallicity and cloud-top pressure are correlated. Atmospheric compositional scenarios along a curved distribution agree with the data at  $3\sigma$ , spanning a range of atmospheric metallicities from 1 to 700 times the solar metallicity. Figure 3.8 shows that a representative 10,000-times-solar (water-dominated) spectrum is robustly excluded by the data. The high mean molecular weight and subsequent small scale height of this atmosphere would not allow the significant water absorption feature observed in the WFC3 band pass.

We found that models with atmospheric metallicities corresponding to solar metallicity required the presence of small-particle hazes to match the HST and Kepler data points simultaneously. The fit to the data improved towards higher metallicities, reaching the best-fit value at 190 times solar metallicity. The presence of the water absorption feature in the WFC3 spectrum required that any cloud deck must be at a pressure lower than the 10 mbar pressure level (higher altitude) (Figure 3.9), and the Kepler and Spitzer transit depths impose a similar lower limit on the cloud top pressure.

### 3.5 Conclusions

The atmospheric and bulk compositions of exoplanets provide important clues to their formation and evolution. Mass and radius alone do not provide unique constraints on the bulk compositions of these planets, which are degenerate for various combinations of rock, ice and hydrogen gas [27, 121]. By measuring the mean molecular weight of the atmosphere using transmission spectroscopy, we can resolve these degeneracies and provide stronger constraints on the interior compositions of

these planets [10, 18, 52, 121]. Observations of water vapour dominate the shape of the infrared spectral features for warm (planetary temperature,  $T_p \approx 1,000K$ ) exoplanets. In contrast, the featureless transmission spectra observed for several similarly small planets [19, 36, 45, 48, 100] ( $R_p \approx 3R_\oplus - 4R_\oplus$ ) imply that scattering hazes, clouds, or high mean molecular weights exist in those atmospheres, obscuring absorption features [9, 10, 18] and limiting our ability to understand their interiors directly [10, 18, 121]. HAT-P-11b is the smallest and coldest planet with an absorption signature measured by transmission; this allows the estimation of its atmosphere's mean molecular weight, providing new insights into the formation history of this Neptune-mass planet [10, 18, 39, 52, 121, 122].

Wavelength [microns]	Transit Depths [ppm]	Transit Depth Uncertainties [ppm]	Bandpass- / Bin- width [microns]
0.642 <sup>*</sup>	3365	8	0.2415
1.153	3502	40	0.0094
1.172	3407	47	0.0094
1.190	3421	46	0.0094
1.209	3445	38	0.0094
1.228	3350	41	0.0094
1.247	3377	38	0.0094
1.266	3380	45	0.0094
1.284	3457	40	0.0094
1.303	3436	35	0.0094
1.322	3448	39	0.0094
1.341	3476	43	0.0094
1.360	3536	44	0.0094
1.379	3499	46	0.0094
1.397	3498	40	0.0094
1.416	3524	41	0.0094
1.435	3591	44	0.0094
1.454	3524	43	0.0094
1.473	3520	39	0.0094
1.492	3447	39	0.0094
1.510	3344	45	0.0094
1.529	3513	41	0.0094
1.548	3471	50	0.0094
1.567	3438	49	0.0094
1.586	3414	53	0.0094
1.604	3383	45	0.0094
1.623	3415	38	0.0094
1.642	3480	48	0.0094
1.661	3498	60	0.0094
1.680	3376	74	0.0094
3.521 <sup>†</sup>	3384	20	0.3685
4.471 <sup>†</sup>	3363	27	0.5021
3.521	3421	29	0.3685
3.521	3347	29	0.3685
4.471	3321	38	0.5021
4.471	3407	37	0.5021

Table 3.3: Transit depths as a function of wavelength for Kepler, HST WFC3, Spitzer IRAC1, and Spitzer IRAC2.

<sup>b</sup>Kepler transit depth determined from all 208 phased and binned Kepler transits

<sup>†</sup>Weighted mean of the two other independent Spitzer transits for each channel

## Chapter 4: Warm Spitzer Eclipse Photometry of HAT-P-11b

### Abstract

Recent results from the Kepler space mission revealed that the primary population of exoplanets have radii between that of Earth and Neptune. This regime is therefore critical to understanding the bulk of planet formation and long term evolution of exoplanetary atmospheres. Bulk density measurements for many of these exoplanets are significantly degenerate between hydrogen-rich and high metallicity atmospheres. Given the predicted, inverse trend between planetary mass and atmospheric metallicity, it is important to investigate the atmospheric metallicity of planets within this regime; most planets are small, but we are unable to confirm if they are mostly gaseous or rocky. Our team observed the transiting warm-Neptune HAT-P-11b using the warm Spitzer-IRAC instrument to measure the eclipse depth at both 3.6 & 4.5  $\mu m$ . HAT-P-11b has a radius and mass at the upper edge of the bulk population for Kepler planets ( $\sim 4.5 R_{\oplus}$  &  $\sim 27 M_{\oplus}$ ), which provided a characterization of the boundaries of this distribution and favorable observability in that the larger radius (area) provides more photons for an eclipse depth to be measured – assuming the same temperature. Our team recently discovered a spectroscopic signature of water vapor in the upper atmosphere of HAT-P-11b, con-

straining many planetary properties such as scale height and molecular abundances, but only an upper limit on the atmospheric metallicity. Temperature measurements of this exoplanet are predicted to provide greater context for the energy budget and metallicity of the upper atmosphere. With an equilibrium temperature of  $878 \pm 15 K$ , the eclipse depth is predicted to be at the limits of warm Spitzer measurement uncertainty. As a result, we were unable to detect an eclipse depth at either wavelength, with over nine different observations, spanning two distinct ranges in phase. We present upper limits on the eclipse depth over the complete observation window at both wavelengths, with greater detail given the range in phase predicted for the eclipse using radial velocity (RV) measurements. Although it is still possible that the uncertainty in the planetary eccentricity could place the eclipse outside of the observed range in phase, it is more likely – given recent RV measurements – that the eclipse depth is below the detection threshold for the warm Spitzer mission, making it an excellent candidate for the upcoming James Webb Space Telescope observations.

## 4.1 Introduction

Planet formation theories, such as core-accretion, predict an inverse trend between planetary mass and atmospheric metallicity [5]. The more massive a core with which a planet forms, the more hydrogen it can accrete from its natal environment, and the less metal-rich its final atmosphere may become [52]. Combined radial velocity (RV) mass estimates with radius measurements for hundreds of transiting exoplanets [22–24, 29] have shown that, indeed, there is a trend with bulk density and planetary mass that supports core-accretion. In the case of small planets,  $R_p < 4 R_\oplus$  – the majority of known planets in our galaxy – there is a strong degeneracy between core mass and atmospheric mass. For a given small planet, with a known radius and mass, it is difficult to confirm whether it has a rocky core with a hydrogen envelope or a low density (volatile rich) core with a high-metallicity atmosphere [22]. To understand the bulk efficiency of planet formation [73, 123], we must break these degeneracies between core mass and atmospheric metallicity for small planets. It is therefore important to measure the atmospheric metallicity and temperature to uniquely constrain the mean molecular weight of the atmosphere.

Our ability to measure the metallicity of exoplanet atmospheres is improved for colder planets  $T_{eq} < 1000K$ , where methane absorption or emission may be more apparent in the upper atmosphere [8, 51]. By comparing the absorption features from  $CH_4$  and  $CO$ , we could in principle constrain both the atmospheric metallicity

and the  $C/O$ -ratio, another important planet formation metric [3]. For exoplanets with  $T_{eq} > 1000K$ , thermochemical equilibrium prefers  $CO$  production to  $CH_4$ , inhibiting a comparative analysis of these molecules. Non-equilibrium processes could enhance  $CO$  over  $CH_4$  for cooler planets [18, 39], providing a new regime of atmospheric physics to explore using emission spectroscopy – variations in the eclipse depths over a span of wavelength – especially at warm Spitzer wavelengths.

HAT-P-11b is a warm Neptune [30, 61, 102, 107] at the upper edge of the “small” planet regime ( $\sim 4.5 R_{\oplus}$  &  $\sim 27 M_{\oplus}$ ). With an equilibrium temperature of  $T_{eq} = 878 \pm 15$ , it provides an excellent test-case for spectroscopic observations to constrain its molecular abundances and atmospheric metallicity. Recently, our team discovered water vapor absorption through transmission spectroscopy from the upper atmosphere using the Hubble Space Telescope Wide Field Camera 3 (HST-WFC3) [30]. We combined these measurements with transit depths measured from Kepler ( $0.6 \mu m$ ) and Spitzer ( $3.6$  &  $4.5 \mu m$ ), but were only able to define an upper limit on the atmospheric metallicity. Unconstrained stellar activity during the HST-WFC3 spectroscopic observations inhibited our ability to directly compare the warm Spitzer and HST transit depths. Stellar activity is a significant complication with using transmission spectroscopy to measure atmospheric metallicity for exoplanets orbiting active stars. Comparing observations over multiple epochs is a primary difficulty with stellar activity, because the stellar flux varies over time and each epoch has a different reference stellar spectrum.

Eclipse photometry is much less affected by the presence of star spots. For eclipse photometry, fluctuations in the stellar luminosity primarily change the out

of eclipse baseline per observation. Therefore, we can more easily compare multiple eclipses directly, assuming no unresolved, correlated noise sources. In contrast, multiple epochs of transmission spectra must be carefully stitched together with either full knowledge of the stellar photosphere over time, or significant assumptions about the atmospheric behaviour and uniformity.

As the exoplanet passes behind its host star, we are in principle able to measure the flux emerging from its atmosphere as the change in the system flux from before, during, and after the eclipse. Because the photons from the planet are blocked by the host, the eclipse depth becomes

$$\delta = \frac{F_{OOE} - F_{IE}}{F_{OOE}} = \frac{(F_s + F_p) - F_s}{F_s + F_p} = \frac{F_p}{F_s + F_p} \approx \frac{F_p}{F_s} \quad (4.1)$$

with  $F_{OOE}$  and  $F_{IE}$  representing the flux “out of eclipse” and the flux “in eclipse”, respectively;  $F_s$  is the stellar flux;  $F_p$  is the planetary flux; and  $\delta$  is the eclipse depth.

The eclipse depth is therefore a function of the integrated number of photons absorbed by the detector before and after the eclipse, relative to the in-eclipse photons from only the star. The number of photons emitted by the planet is a function of the temperature of the planet, absorption properties, and the cross section of the illuminated portion of the planetary disk facing the Earth. We were unable to measure this effect for HAT-P-11b. We provide upper limits for its eclipse depths, at both wavelengths, in this paper. Non-detections of the eclipse of HAT-P-11b correspond to an upper limit of the brightness temperature, but also inform us about the limitations for using warm Spitzer to measure temperatures from small, cool

planets [18, 44].

This chapter is formatted such that Section 2 discusses the observations spanning 2009 - 2014 from warm Spitzer at both 3.6 & 4.5  $\mu m$ . Section 3 details the behaviour of warm Spitzer instrumental and correlated noise sources as well as our recently developed method for decorrelating it. In Section 4, we interpret the significance of our non-detections for both finding eclipse centers and false-positive rejection. We provided upper limits for the eclipse depths and temperature measurements. Section 5 concludes with a discussion about the role of eclipse photometry and the statistical significance and physical implications of our non-detections.

## 4.2 Observations

We observed HAT-P-11b over nine different epochs using warm Spitzer Infrared Array Camera (IRAC) Channel 1 & Channel 2 at 3.6 and 4.5  $\mu m$ , respectively [103]. On 2009 Dec 05, Spitzer observed HAT-P-11 for 21.96 hours (PI: Richard Barry). HAT-P-11 is a bright target ( $H_{mag} = 7.131 \pm 0.021$ ; [102]); to avoid saturation, and improve temporal coverage, we used sub-array mode with 0.4s integration per frame. We used this long time span observation to “find the eclipse” (FTE) and schedule follow-up observations in both warm Spitzer channels. HAT-P-11b orbits its host star every  $4.8878056 \pm 0.0000015$  days [102]. Therefore, the FTE observations covered a phase range between 0.53 to 0.72 – encompassing 97.5% of the radial velocity predicted eclipse phase range. We detected a prospective eclipse at a phase  $\sim 0.62$  and scheduled warm Spitzer to observe the system

again at both 3.6 and 4.5  $\mu m$  channels on 2010 July 18 & 2010 Dec 31 (3.6  $\mu m$ ) and 2010 Sept 05 & 2011 Jan 19 (4.5  $\mu m$ ) (see Table 4.1). Warm Spitzer again observed the system in sub-array mode with 0.4s integrations per frame. A confirmed eclipse was not detected during these observations. We re-analysed all 4 archival observations with our new “Pixel Level Decorrelation” algorithm (PLD) [64] on the FTE observation. We detected a second prospective eclipse at phase  $\sim 0.69$ . Our team then re-observed HAT-P-11 (PI: Heather Knutson) to confirm the detection of this eclipse and measure the eclipse depth of HAT-P-11b at both warm Spitzer wavelengths. Our new observations occurred on 2014 July 19 & 2014 July 23 (3.6  $\mu m$ ) and 2014 July 28 & 2014 Aug 22 (4.5  $\mu m$ ) (see Table 4.1). Warm Spitzer again observed the system in sub-array mode with 0.4s integrations per frame.

Table 4.1: A catalogue of our 9 observations for HAT-P-11b at 3.6 & 4.5  $\mu m$ , including the time of the observations, number of frames, time span in hours, wavelength, principle investigators, and aperture radius parameters – including the average aperture radius used for the measurement.

(\*static aperture radii; +variable aperture radii)

Epoch	Start Date	End Date	Number of Frames [#]	Time Span [hrs]	Wavelength [ $\mu m$ ]	“Best-Fit” Radii	PI Observations
115	2009-Dec-05	2009-Dec-06	184640	21.96	3.6	$b = 0.0; c = 3.00; r_{avg} = 3.00^+$	R. Barry
161	2010-Jul-18	2010-Jul-18	50048	5.95	3.6	$b = 0.0; c = 3.25; r_{avg} = 3.25^+$	R. Barry
171	2010-Sep-05	2010-Sep-05	50048	5.95	4.5	$b = 0.0; c = 2.75; r_{avg} = 2.75^+$	R. Barry
195	2010-Dec-31	2010-Dec-31	50048	5.95	3.6	$b = 0.0; c = 3.50; r_{avg} = 3.50^+$	R. Barry
199	2011-Jan-19	2011-Jan-20	50048	5.95	4.5	$b = 0.0; c = 1.75; r_{avg} = 1.75^+$	R. Barry
460	2014-Jul-19	2014-Jul-19	58240	6.93	4.5	$b = 0.1; c = 2.75; r_{avg} = 2.97^*$	H. Knutson
461	2014-Jul-23	2014-Jul-24	58240	6.93	3.6	$b = 0.0; c = 2.50; r_{avg} = 2.50^+$	H. Knutson
462	2014-Jul-28	2014-Jul-29	58240	6.93	4.5	$b = 0.2; c = 2.75; r_{avg} = 3.23^*$	H. Knutson
467	2014-Aug-22	2014-Aug-22	58240	6.93	3.6	$b = 0.1; c = 1.50; r_{avg} = 1.72^*$	H. Knutson

## 4.3 Analysis

### 4.3.1 Aperture Photometry

Our analysis utilized the Basic Calibrated Data (BCD) files produced by version S18.18.0 (2010 observations) and S19.1.0 (2014 observations) of the warm Spitzer pipeline. Our 2014 observations implemented the new “PEAK-UP” observing mode which maintained the telescope pointing within 0.1 pixels of the peak sensitivity regime to minimise instrumental effects [124, 125]. We used both two dimensional (2D) Gaussian centering and flux-weighted centroiding to track the location of the PSF over time [36, 86, 126]. Our final analysis was derived from Gaussian centering because it provided a more stable PSF-centroid distribution, with less outliers [127]. We then performed a  $4\sigma$  median filter of any residual outliers; we set those outliers to the locate median of a 7-point width window in time. To subtract the background, we tested a fleet of algorithms including median background estimation, Gaussian fitting to the background histogram, and kernel density estimation. Although kernel density estimation provided the most precise capture of the background distribution, a simple median background estimation provided the most improved residuals. We tested all three methods, but only present the results from the median background estimation technique. Prior to further analyses, we clipped the first 4500 data points (i.e.  $\sim 7.5\%$ ) – a common practice to ameliorate instrumental effects [30, 36, 64, 126].

In all 9 observations, we centered a circular aperture on the stellar image

using aperture photometry. We examined 176 different aperture radii, including both static and variable radii to measure the flux over time as a set of photometric light curves. We calculated the stellar flux within the aperture, including analytic approximations for the partial coverage of pixels at the boundary of the numerical aperture. Using formulae from [126], we chose to span a range of aperture radii from 1.0 to 7.0 pixels, where

$$r_{i,aper} = b\sqrt{\beta_i} + c \quad \beta_i = \frac{(\sum I_j)^2}{\sum (I_j)^2}, \quad (4.2)$$

where  $\beta_i$  represents the noise pixel parameter for the stellar image – or “effective width of the PRF” – for each frame  $i$  [36, 63, 86, 87, 126].  $b$  &  $c$  are parameters to adjust the aperture radius in units of pixels;  $b \in [0, 1.5]$  in steps of 0.1 (16 steps);  $c \in [1.0, 3.5]$  in steps of 0.25 pixel (11 steps). When  $b = 0$ , the aperture radii are in the limiting case of “static aperture radii”. For increased values of  $b$ , the aperture radii track the effective width of the PRF more closely. In the formula for  $\beta_i$ ,  $I_j$  is the intensity of pixel  $j$ , and the summations extend over all pixels wherein the stellar intensity is significant.

By adjusting the  $b$  parameter, we varied the significance of the noise pixels,  $\sqrt{\beta_i}$ , to collect the optimal amount of light per frame. We could then better understand the synergy between a photometric time series and our choice of decorrelation technique. As will be seen below, the PLD algorithm tends to favor more static radii aperture photometry,  $b \sim 0$ . [36] found that pixel-mapping techniques that use Gaussian kernel regression tend to prefer variable aperture radii,  $b > 0$  [62, 63].

We examined the span of aperture photometry that works best with our choice of decorrelation technique. This can vary between techniques, instruments, wavelengths, and possibly epochs with the same wavelength & instrument.

### 4.3.2 Decorrelation

After we measured the photometry, we immediately saw the well-known intra-pixel sensitivity effect for Spitzer-IRAC – a strong correlation between flux and position on the detector. Spitzer-IRAC has several, well-known instrumental noise profiles, related to various physical processes that add correlated noise to the observations. The most well-known of these effects is the intra-pixel effect [36, 44, 58, 62–64]. It is the variation in measured flux as a function of centroid because of non-uniform pixel response over the detector. This variation is caused by variable sensitivity on the sub-pixel crystalline structure of the detector [124]. This effect is on the same order of magnitude as the predicted eclipse and must be decorrelated (removed) from the data [11, 36, 58, 62, 63, 128, 129] (Figure 4.1).

Many teams [62–64, 117, 124, 130] uncovered correlated signals between physical processes from the telescope-instrument functions that can be attributed to these noise sources. Recently, our team developed and utilized a new, simple decorrelation technique on our HAT-P-11b observations, named “Pixel Level Decorrelation” (PLD). We used PLD to re-analyse the five archival HAT-P-11b observations and discovered a new, prospective detection at phase  $\sim 0.69$ . The residuals from our PLD algorithm contained a very low degree of residual correlated noise – a significant

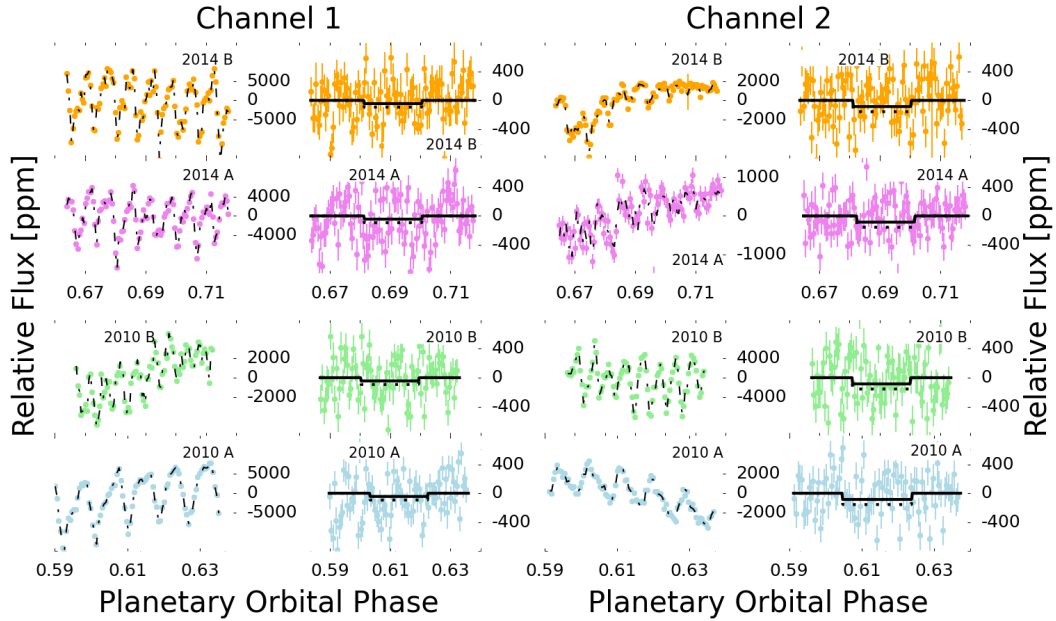


Figure 4.1: Eight epochs of our warm Spitzer-IRAC observations. (Left) Shows our 4 Spitzer-IRAC Channel 1 ( $3.6 \mu m$ ) observations. (Right) Shows our 4 warm Spitzer-IRAC Channel 2 ( $4.5 \mu m$ ) observations. All data are binned by a factor of 512 for illustration purposes only. Green and Blue data represent our 2010 observations (PI: Richard Barry); Violet and Orange data represent our 2014 observations (PI: Heather Knutson). The dashed lines represent the best-fit Pixel Level Decorrelation (PLD) model from our fits over the null hypothesis test (no eclipse model). In the decorrelated figures, the solid and dashed lines represent the black body predicted eclipse models assuming uniform redistribution and instantaneous re-radiation, respectively; the models have been arbitrarily centered at the central phase of each observation as a comparison between the eclipse curve predictions and the Spitzer-IRAC residuals. Uniform redistribution predicts a  $T_{eq} = 878$  K, corresponding to an eclipse depth of  $\sim 45$  ppm and  $\sim 87$  ppm at  $3.6$  and  $4.5 \mu m$ , respectively. Instantaneous re-radiation predicts a  $T'_{eq} = 1044$  K, corresponding to an eclipse depth of  $\sim 96$  ppm and  $\sim 156$  ppm at  $3.6$  and  $4.5 \mu m$ , respectively. See Table 4.2 for the upper limit predictions that we derived from each data set.

improvement over previous Spitzer-IRAC decorrelation techniques [36, 44, 62–64]. Taking advantage of our preliminary analysis and updated radial velocity measurements, which agreed with each other to within  $1\sigma$ , our team re-observed HAT-P-11 at four new epochs, encompassing a phase range centered at phase  $\sim 0.69$  (0.66 - 0.72), at both 3.6 & 4.5  $\mu m$ .

PLD is a basis vector algorithm that uses the measured flux values in the  $N$  brightest pixels over time,  $P_i(t)$  – normalised by their integrated flux over time,  $\sum_i P_i(t)$  – as its basis vectors. These normalised pixel levels,  $\hat{P}_i(t)$ , are stored in a linear matrix that we invert to generate the solution [64]. We must normalise the basis vectors to remove the average astrophysical signal. The normalised basis vector becomes,

$$\hat{P}_i(t) = P_i(t) \left( \sum_i P_i(t) \right)^{-1} \quad (4.3)$$

This was essential to preventing accidental injection of artificial signals (i.e. an eclipse) into the data. The raw pixel values over time include both stellar and instrumental variations, such as the eclipse for which we are searching. By normalising each pixel level basis vector,  $P_i(t)$ , by the sum of the basis vectors as a function of time (Equation 4.3), we removed the average astrophysical signal. We modeled the temporal portion of astrophysical component by simultaneously fitting the PLD linear matrix with a polynomial in time, combined with the basis vectors as columns in a single linear matrix.

We then solved this matrix using linear matrix inversion and maximum like-

likelihood estimation, followed by a Markov Chain Monte Carlo (MCMC) to estimate the uncertainties. The PLD matrix columns included the pixel level basis vectors, a polynomial function of time, and a [88] eclipse light curve model. We inverted this matrix onto the integrated flux over time (photometric light curve),  $\hat{F}(t)$ , to solve the equation

$$\hat{F}(t) = \left( \sum_i c_i \hat{P}_i(t) + \tilde{P}_n(t; \{a, b, c, \dots\}) \right) \times \text{eclipse}(t; P, T_c, b, R_s/a, F_o, e, \omega), \quad (4.4)$$

where the right hand side of this equation is the noise model we used to reduce the correlated noise sources;  $\hat{P}_i(t)$  are the basis vectors;  $c_i$  are the basis vector coefficients;  $\tilde{P}_n(t; \{a, b, c, \dots\})$  represents a time dependent polynomial that models the temporal portion of the astrophysical component –  $\{a, b, c, \dots\}$  are the polynomial coefficients; and  $\text{eclipse}(t)$  is computed as a [88] transit light curve with zero limb darkening included. Figure 4.2 shows the individual components of the PLD fitting algorithm in detail; note that the eclipse curve shown in Figure 4.2 is artificial because no eclipse was detected. We modeled the temporal portion of the astrophysical component (discussed above) as a quadratic polynomial in time, after subtracting the median time coordinate:

$$\tilde{P}_3(t; \{a, b, c\}) = a * (t - t_{med})^2 + b * (t - t_{med}) + c \quad (4.5)$$

In the PLD algorithm, we selected a 3x3 sub-section of the warm Spitzer-IRAC 32x32 grid, out of which we derived our N=9 PLD basis vectors. The median value of all Gaussian center positions in  $y$  &  $x$ , per epoch, was taken as the center of

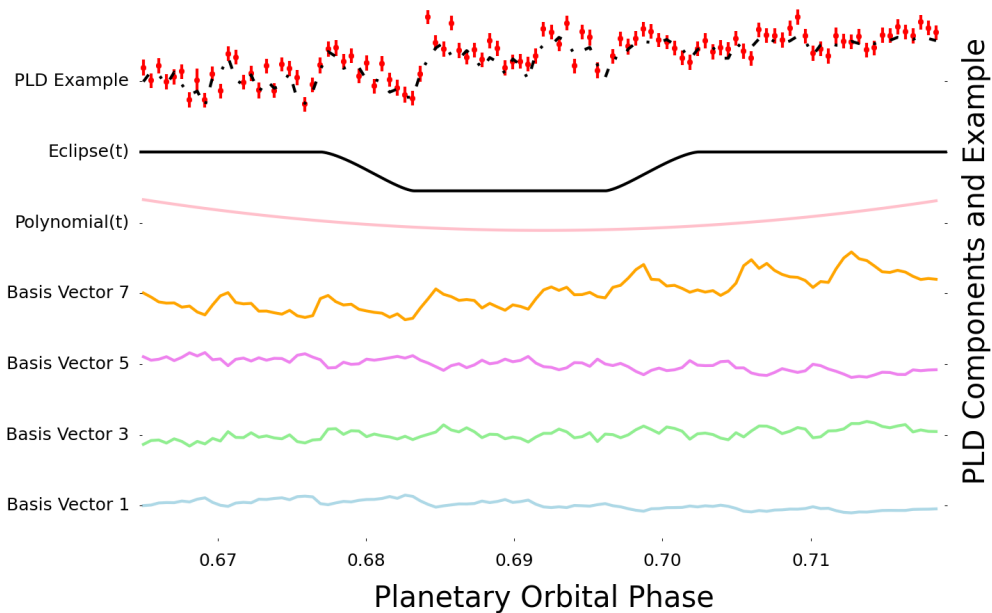


Figure 4.2: Components of our PLD algorithm, including 4 example basis vectors (Green, Blue, Violet, Orange), a quadratic model in time (Pink), Mandel & Agol (2011) [88] eclipse model (Black). The red points are the normalised raw data the we binned by a factor of 512 for illustration purposes only. The dashed black line is our PLD combined best fit model, with no eclipse model included (the null hypothesis). We rescaled all of the temporal features by a factor of 50 for illustration purposes only.

that 3x3 set of pixel values from which to form our PLD basis vectors. This was consistently the (15,15) pixel – which is the center of the Spitzer-IRAC sub-array. In this paper, we modified the PLD algorithm by subtracting the median value of each basis vector, which improved the resulting  $\chi^2$  values slightly. With the technique, we could multiply the [88] eclipse model to the  $PLD(t)$  function (Equation 4.4). Then the basis vectors only contained the information that directly correlated with the instrumental noise fluctuations, and not their relative offsets. This put more weight on the polynomial,  $\tilde{P}_n(t; \{a, b, c, \dots\})$ , to include at least a constant term.

### 4.3.3 Binning

To improve the performance of PLD, we binned the basis vectors,  $\hat{P}_i(t)$ , the polynomial in time,  $\tilde{P}_n(t; \{a, b, c\})$ , and the photometry,  $F(t)$ , by a factor of  $N = 64$ . This value was chosen because the image cubes are 64 frames in length. We also tested  $N=32$  and  $N=128$  with a linear matrix solver, but found no significant differences in the results. [64] provide an explanation for why binning the data is useful and valid: They find that solutions based on binned data often exhibit less noise on the time scale of the eclipse, but always have slightly greater point-to-point scatter when those coefficients are applied to unbinned data, versus a solution of Equation 4.4 obtained on the unbinned data directly. We accepted greater scatter on short time scales, as a trade-off for minimized noise on longer time scales. [64] found that Equation 4.4 was sufficiently effective that the solutions often exhibited less scatter than traditional methods on all time scales. They found that binning helped pixels at the edge of the stellar PSF with relatively low flux levels; binning also improved the precision of the normalised pixel levels,  $\hat{P}_i(t)$ , that form the basis vectors of their PLD decorrelation. We adopted this methodology and bin all of our PLD vectors by  $N = 64$ , but compute the Root-N, variance, and  $\chi^2$  values from the unbinned data.

### 4.3.4 Peak-up Observing Mode

Our 2014 observations utilized the new “peak-up” observing mode, which maintains the center of the stellar image within 0.1 pixels of the peak sensitiv-

ity regime over the sub-pixel crystalline structure [124, 125]. By limiting variations in the pixel position to this regime, the variations in the instrument response as a function of sub-pixel position were minimised. As a result, the intra-pixel effect was subsequently minimised, which improved our ability to mitigate this correlated noise source. Figure 4.1 shows the raw and reduced light curves for HAT-P-11b. The improvement gained by using peak-up over non-peak-up observations can be shown in the central concentration of the photons as a function of time. By maintaining peak sensitivity, the instrument response collects more photons in the central pixel, relative to observations with large deviations from the peak sensitivity regime (i.e. our 2010 warm Spitzer observations).

The central concentration of photons can be measured by the effective width of the PSF, which we refer to as the “noise-pixels” ( $\sqrt{\beta_i}$  in Equation 4.2). If the peak-up observing mode reduced the intra-pixel effect, then the “noise-pixels” should be relatively uniform over time. In 2010, without peak-up, the noise-pixel values during our HAT-P-11b Channel 1 and Channel 2 observations were concentrated around  $\langle\sqrt{\beta_{3.6}}\rangle = 2.368 \pm 0.103$  and  $\langle\sqrt{\beta_{4.5}}\rangle = 2.493 \pm 0.146$ , respectively. In 2014 (with peak-up), the noise-pixel values during our HAT-P-11b Channel 1 and Channel 2 observations were concentrated around  $\langle\sqrt{\beta_{3.6}}\rangle = 2.392 \pm 0.057$  and  $\langle\sqrt{\beta_{4.5}}\rangle = 2.201 \pm 0.062$ , respectively. The width of the PSF is set by the optics of the telescope and instrument; the central concentration of photons is therefore determined by the PSF width, apparent magnitude of the star, integration time, and the instrument response profile. For a given star + integration time setup, and a uniform instrument response profile, the central concentration of photons should

be constant. We predicted that an improvement in limiting the intra-pixel effect can be measured as a reduction in the variance of the “noise-pixel” distribution over the time span of our observations.

### 4.3.5 Selecting the Best Aperture Radius

We examined 176 raw photometric light curves with our PLD algorithm. We chose the “best-fit” aperture radius per observation as the combination of  $b$  and  $c$  that minimised both the  $\chi^2$  over the Root-N curve ( $\chi_{RMS}^2$ ) as well as the variance over the residuals,  $\sigma_{res}^2 - r'_{aper}(b_o, c_o) = \min_{b,c}(\chi_{RMS}^2 + \sigma_{res}^2)$ . Where the Root-N curve,  $RMS(N)$ , and its uncertainty,  $RMS(N)_{error}$ , can be measured using formulae from [131];

$$RMS(N) = \langle (Binned(Residuals, N))^2 \rangle \quad \text{and} \quad RMS(N)_{error} = \frac{RMS(N)}{\sqrt{2M}} \quad (4.6)$$

such that  $M$  is the number of bins over the observational time frame (e.g., if we have 2048 data points, at a bin size of  $N = 64$ ,  $M = 32$ ).

The Root-N curve is a measure of the time averaged variance as a function of bin size (i.e. the “Root-Mean-Squared”). We used this as a metric to determine how far the Root-N curve for the residuals deviated from white noise as a function of bin size,  $N$ . For an ideal, white noise signal, the Root-N curve falls off as a power-law with power  $-\frac{1}{2}$  ( $RMS(N) = N^{-\frac{1}{2}}$ ), see Figure 4.3. If we bin our data over a range of  $N$ , starting from unity – or unbinned – and successively increased  $N$  to well

over the time-span for our signal (i.e. the transit duration for the eclipse), and the resulting Root-N curve approached the white noise limit – within its uncertainties –, then we could be confident that we reduced any correlated noise sources that may interfere with detecting an eclipse. In Figure 4.3, the dashed black line represents the Gaussian, white noise model and the colored curves represent the Root-N curves for each of our “best-fit” aperture radii.

The significance of the intra-pixel effect varied dramatically as a function of  $b$  and  $c$ , in Equation 4.2. Static aperture photometry ( $b = 0$ ) exhibited the greatest deviations related to the effect of intra-pixel sensitivity. Our metric,  $\chi_{RMS}^2 + \sigma_{res}^2$ , measured the synergy between each photometric light curve and the choice of decorrelation technique by how much correlated noise remained in the residuals. Figures 4 and 5 show the  $b - \times - c$  grid for the  $\chi_{RMS}^2$  and the residual variance – in the limiting case of no eclipse – respectively; the colorscale is associated with “goodness of fit”. Figure 4.3 shows the Root-N curve for each of the “best-fit” aperture radii for all of our observations. Because we used variable aperture radii, the diagonal lines in our 2D maps represent the line of constant, average aperture radius; this occurs where  $\langle r_{aper}(b, c) \rangle_{b,c} = \{1, 2, 3, \dots\} \in \mathbb{Z}$ ; in the static aperture case, this occurs when  $r_{aper}(b, c) \in \mathbb{Z}$  (see Figure 4.4).

Figure 4.5 and Figure 4.6 show all 176 decorrelated photometry and Root-N curves associated an example observations from Channel 1 ( $3.6 \mu m$ ) and Channel 2 ( $4.5 \mu m$ ). We binned the decorrelated photometry by a factor of 512 for illustration purposes only. The red circles in Figure 4.6 represent the aperture radius that minimised our metric and corresponds to the orange curve in Figure 4.6. The blue

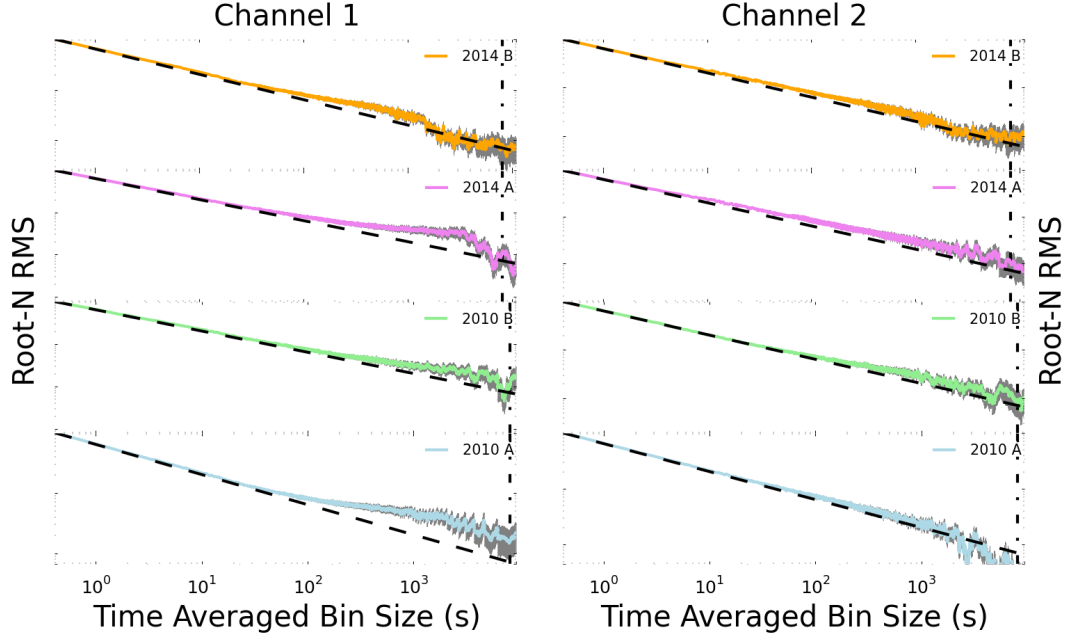


Figure 4.3: Eight epochs of warm Spitzer-IRAC observations Root-N curves. (Left) Shows the Root-N curves for our 4 warm Spitzer-IRAC Channel 1 ( $3.6 \mu m$ ) observations. (Right) Shows the Root-N curves for our 4 warm Spitzer-IRAC Channel 2 ( $4.5 \mu m$ ) observations. Green and Blue data are from our 2010 observations (PI: Richard Barry); Violet and Orange data are from our 2014 observations (PI: Heather Knutson). The sloped, dashed lines represent the predicted Gaussian (white) noise as a function of bin size for comparison to the residuals (colored). The vertical dashed lines represent the time span that corresponds to the predicted eclipse duration. We calculated the Root-N curves to a time span of  $\frac{1}{2}$  our observational time span. The distance between the Root-N curves for each epoch deviates from the white noise model as a result of residual correlated noise sources. This deviation is negligible for all but two observations, both in Channel 1 ( $3.6 \mu m$ ); but, the deviations from 2014 A and 2010 A observations are still within  $1\sigma$  of the predicted white noise model.

squares in Figure 4.6 and the blue curve in Figure 4.6 correspond to the aperture radius derived when we minimized the  $\chi_{RMS}^2$  grid alone, as oppose to the minimum over the  $\chi_{RMS}^2 + \sigma^2$  grids (Figures 4 & 5). In most of our observations, these curves

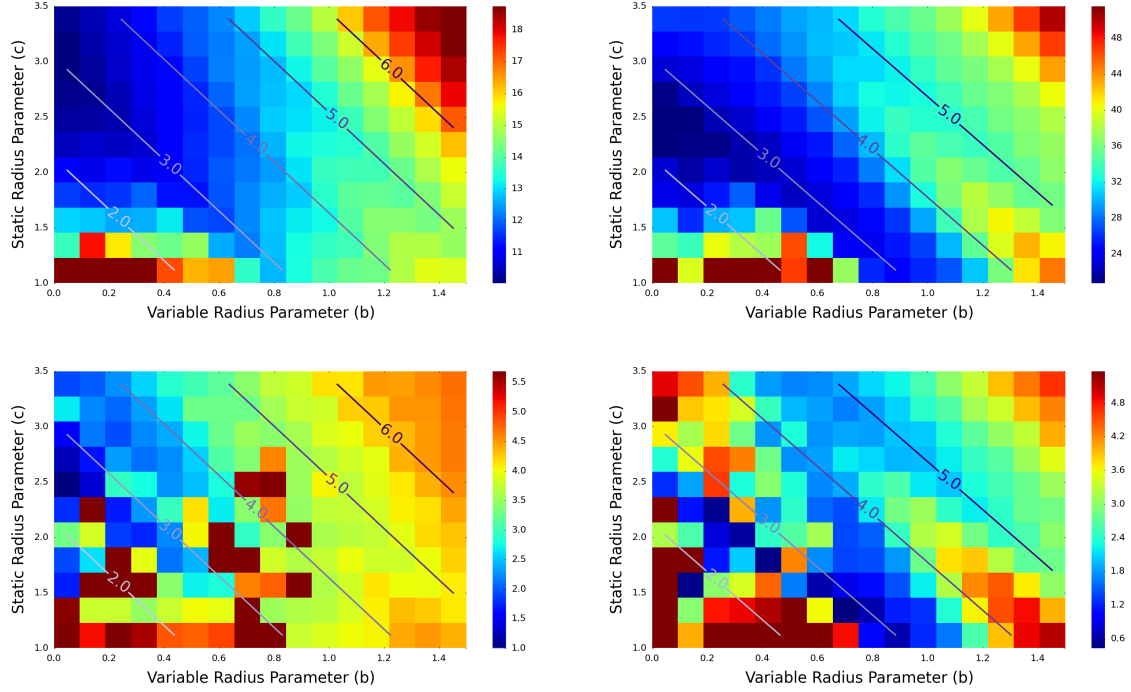


Figure 4.4: 2D maps of  $\chi_{RMS}^2$  vs pure white noise (top) and variance,  $\sigma^2$  (bottom) as a grid over  $b$  and  $c$ ; we will refer to both of these as the “goodness of fit”. The color scale is associated with “goodness of fit” for each category. Blue represents lower  $\chi_{RMS}^2$  (top) or  $\sigma^2$  (bottom) – better “goodness of fit” – than red. The straight lines represent where the radius is (on average) an integer value. Using the PLD algorithm, Channel 1 observations (3.6  $\mu m$ ; left) preferred static aperture radii,  $b = 0$ . Channel 2 observations (4.5  $\mu m$ ; right) were more ambiguous, but preferred small amounts of variable aperture tracking,  $b \sim 0$  or  $r_{aper} \sim 3$ . Channel 1 had definitive, unimodal results, while channel 2 results were degenerate, showing several local minima. Table 4.2 shows all of our “best-fit” aperture radii, as well as the values for  $b$  and  $c$  that we used to derive them.

overlapped or were well within the uncertainties.

We compared all decorrelated photometry with the black body predicted transit depths derived from equilibrium temperatures associated with uniform redistribution and instantaneous re-radiation,  $T_{eq} = 878$  K and  $T'_{eq} = 1044$  K, respectively.

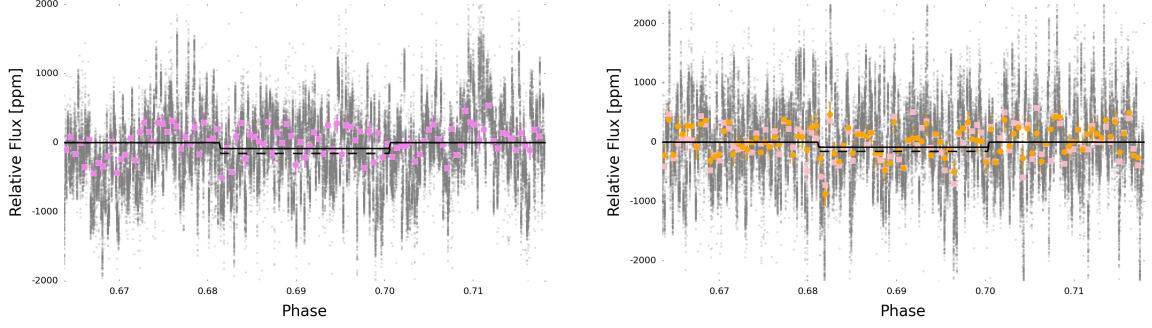


Figure 4.5: The grey points are the decorrelated photometry for all 176 photometry light curves for an example from Channel 1 ( $3.6 \mu m$ ; 2014 A; left) and Channel 2 ( $4.5 \mu m$ ; 2014 B; right). The grey points represent the full range of our decorrelated light curves for each of our observations. The violet (left) and orange (right) points are photometric light curves from the “best-fit” aperture radius (Table 4.1) and the pink squares (left & right) points an example if we chose the “best-fit” aperture radius as the minimum of only the  $\chi^2_{RMS}$ ; note that the pink squares are more apparent in channel 2 (right). It is important to understand the full range of uncertainties by marginalising over all numerical parameters as nuisance parameters. In our previous figures, we showed the light curves that represented the “best fit” aperture radii associated the minimum of both  $\chi^2_{RMS} + \sigma^2$  – the violet (left) and orange (right) points here. The solid (dashed) curves represent the predicted, black body eclipse curves with  $\delta \sim 45$  ppm ( $\delta \sim 94$  ppm) and  $\delta \sim 87$  ppm ( $\delta \sim 156$  ppm) at  $3.6$  and  $4.5 \mu m$ , respectively, assuming uniform redistribution (instantaneous re-radiation). Uniform redistribution (instantaneous re-radiation) predicts a  $T_{eq} = 878$  K ( $T'_{eq} = 1044$  K).

Uniform redistribution occurs when the radiation input from the host star (HAT-P-11) is transported evenly throughout the exoplanetary atmosphere through any combination of several different processes, including advective (winds), diffusive, and convective fluid dynamics [47, 132, 133]. Instantaneous re-radiation occurs when the radiative time scales are much shorter than than the advective time scales, such as in a static atmosphere.

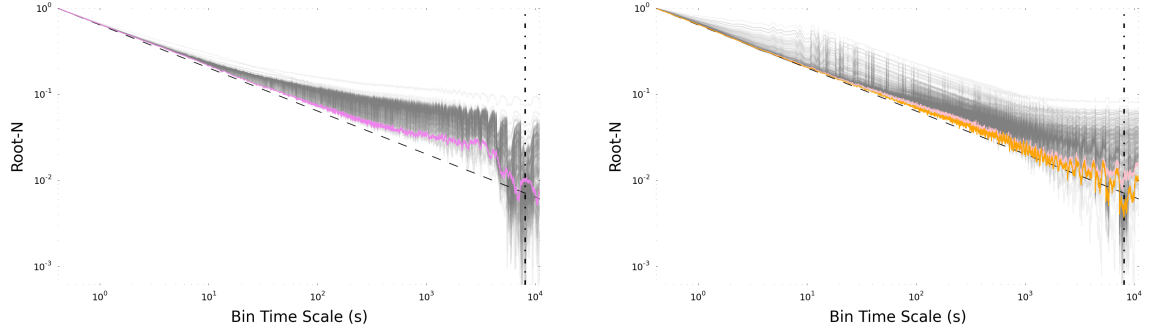


Figure 4.6: Root-N curves for all 176 photometry light curves for an example from Channel 1 (3.6  $\mu\text{m}$ ; 2014 A; left) and channel 2 (4.5  $\mu\text{m}$ ; 2014 B; right). The grey curves represent the full range of the Root-N curve for each of our light curves. The violet (left) and orange (right) curves are the Root-N curves for the “best-fit” aperture radius (Table 4.1) and the pink (left & right) curves are an example if we chose the “best-fit” aperture radius as the minimum of only the  $\chi_{RMS}^2$ ; note that the pink curve is more apparent in channel 2 (right). . Most of our observations could not distinguish between the pink and the violet/orange curves here. In our previous figures, we showed the Root-N curves that represented the “best fit” aperture radii associated the minimum of both  $\chi_{RMS}^2 + \sigma^2$  – the violet (left) and orange (right) curves here.

## 4.4 Discussion

### 4.4.1 Equilibrium Temperature Eclipse Depth Predictions

The expected signal from the eclipse of an exoplanet as it passes behind its host star – the loss of planetary photons from the star + planet system – creates a dip in the total light from the system (Equation 4.7). The measured depth of an eclipse is therefore dependent on the flux coming from the planet relative to the amount of flux coming from the host star, integrated over the instrument spectral response profile [11],

$$\delta = \left(\frac{R_p}{R_s}\right)^2 \frac{\int F_p(\lambda)S(\lambda)(\lambda/hc)d\lambda}{\int F_s(\lambda)S(\lambda)(\lambda/hc)d\lambda} \quad (4.7)$$

where  $\delta$  is the photometric eclipse depth;  $F_p(\lambda)$  is the flux from the planet;  $F_s(\lambda)$  is the flux from the star; and  $S(\lambda)$  is the integrated over the spectral response function of the detector. Physically, the eclipse depth is a differential measurement of the lack of planetary photons as the planet passed behind its host star along our line of sight.

We used a black body model, at the equilibrium temperature of HAT-P-11b to approximate the planetary spectrum and a PHOENIX model [104] to approximate the stellar spectrum at the effective temperature of HAT-P-11. The equilibrium temperature is calculated as

$$T_{eq} = T_s \sqrt{\frac{R_s}{2a}} (f(1 - A))^{\frac{1}{4}}, \quad (4.8)$$

such that  $T_s$  is the stellar effective temperature;  $R_s$  is the measured stellar radius;  $a$  is the orbital semi-major axis;  $A$  is the bond albedo;  $f$  is the redistribution factor:  $f = 1$  represents uniform redistribution and  $f = 2$  represents instantaneous re-radiation. In the case of uniform redistribution (straight line in Figures 1 & 5), HAT-P-11b has an equilibrium temperature of  $T_{eq} = 878 \pm 15\text{K}$  [102]. In the case of instantaneous re-radiation (dashed line in Figures 1 & 5)  $T'_{eq} = 1044\text{K}$ . The equilibrium temperatures predict eclipse depths of  $\delta_{3.6} \sim 45$  ppm &  $\delta'_{3.6} \sim 94$  ppm ( $3.6 \mu\text{m}$ ) and  $\delta_{4.5} \sim 86$  ppm &  $\delta'_{4.5} \sim 156$  ppm ( $4.5 \mu\text{m}$ ). Figure 4.1 shows the eclipse curves at these predicted transit depths for HAT-P-11b in both warm Spitzer

channels for 8 of our observations, assuming that the eclipse was centered at the central phase of each observation. Figure 4.5 shows a representative example of our warm Spitzer observations at  $3.6 \mu m$  and  $4.5 \mu m$ .

#### 4.4.2 Searching for an Eclipse

To find the central phase of the eclipse, we first fit the FTE photometric light-curve (22.96 hrs;  $3.6 \mu m$ ) without an eclipse model – PLD noise model only. We then used this as our null hypothesis to compare  $\Delta\chi^2$  as a function of phase (see Figure 4.7). We then included an eclipse model and used linear matrix inversion – the core of the PLD algorithm – to simultaneously solve for our PLD basis coefficients, the polynomial coefficients, and the eclipse depth, at 100 locations in phase between 0.53 and 0.72. Given that,

$$\Delta\chi^2 = \chi_{eclipse}^2 - \chi_{no-eclipse}^2, \quad (4.9)$$

if a prospective eclipse was detected, we expected a large, negative deviation in  $\Delta\chi^2$  at the phase of the prospective eclipse.

Figure 4.7 shows our map of  $\Delta\chi^2$  as a function of orbital phase from 0.53 to 0.72. We computed  $\Delta\chi^2$  relative to the “no eclipse” null hypothesis model. Prior to our 2014 observations, we predicted a prospective eclipse detection at phase  $\sim 0.69$ . We reanalysed this location and found that this initial detection was a false-positive; it was most likely caused by our preliminary version of the PLD algorithm identifying a significant, uncorrected, instrumental noise feature. Figure 4.7 shows that only

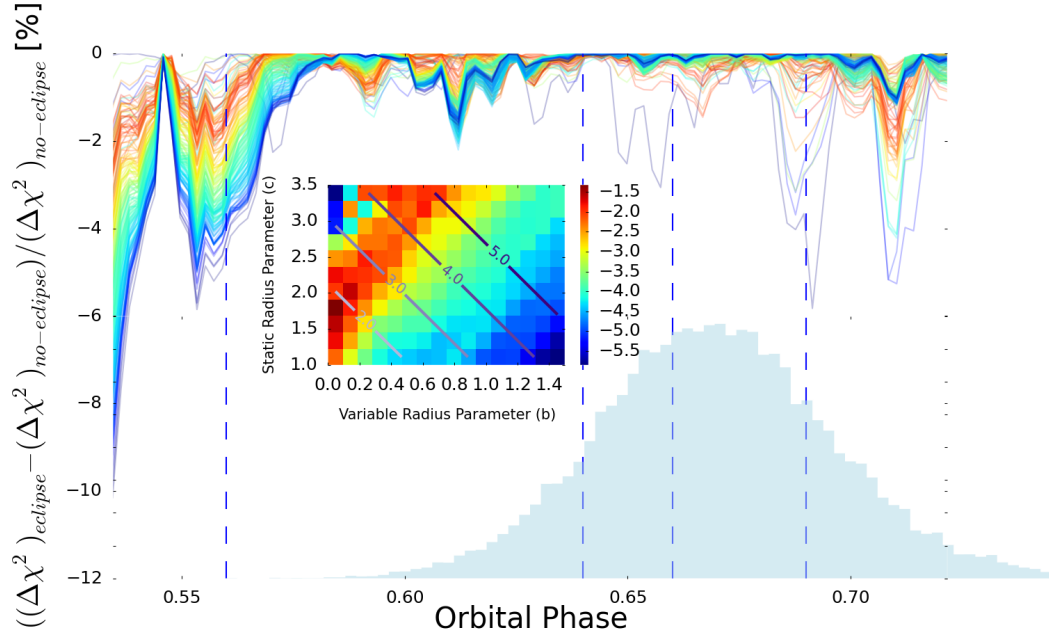


Figure 4.7: A map of  $\Delta\chi^2$  over a span of central phases for a prospective eclipse model at 100 phase values from 0.53 to 0.72. Each color is associated with one of the 176 photometric light curves. The larger the deviation from 0.0, the greater adding an eclipse model at that phase improves the fit to the data – and the more blue we represented the color of the curve. The light blue histogram represents the relative probability – from our latest, unpublished, radial velocity measurements – of an eclipse to occur at each phase. The peak of this distribution occurred near a of phase of  $\sim 0.67$ . The dashed, vertical lines represent the 4 phase locations that we focused on closely to search for the eclipse; i.e. phases  $\sim 0.56$ ,  $\sim 0.69$ ,  $\sim 0.64$ , and  $\sim 0.66$ . We derived the former set from our  $\Delta\chi^2$  map shown here; we derived the latter set from published [111] and unpublished radial velocity measurements. We could not confirm the eclipse at any of these locations. The sub-figure shows the combination of  $b$  and  $c$  that generated the color for each of the  $\Delta\chi^2$  curves. The values of the colors are a measure of the minimum most point in the  $\Delta\chi^2$  curves. All values and colors disregard the spike at phase  $\sim 0.53$  because we argue that this is an edge effect in both the Spitzer-IRAC light curve and the  $\Delta\chi^2$  test.

5 (out of 176) photometric light curves identified the phase  $\sim 0.69$  as a prospective detection. These photometric light curves used aperture radii that were ruled out by our  $\chi^2_{RMS} + \sigma^2$  metric (discussed above). These false-positive deviations occurred for when ( $b = 0$ ) – or near-constant ( $b \sim 0$ ) – and  $c$  was near the limit our range, implying that the aperture that we used included systematic noise from the outer regions of the warm Spitzer-IRAC sub-array.

We compared  $\Delta\chi^2$  from the residuals of the FTE light curves using multiple aperture radii as a false-positive test to confirm or rule out each prospective detection. We closely examined 4 key phases with a robust MCMC analysis. With our improved PLD algorithm [64], we fit to all 176 light curves over the FTE observations and found one prospective detection of an eclipse that could not be ruled out by our false-positive rejection test, most notably at phase  $\sim 0.56$ . After a combination of statistical analysis (see below), we found no conclusive eclipse detections at any phase. The vertical lines in Figure 4.7 represents the 4 phases that we focused on closely; i.e. phases  $\sim 0.56$ ,  $\sim 0.69$ ,  $\sim 0.64$ , and  $\sim 0.66$ . We derived the former set from our  $\Delta\chi^2$  map (Figure 4.7); we derived the latter set from published [111] and unpublished radial velocity measurements. The light blue histogram in Figure 4.7 shows the most recent, unpublished radial velocity predicted location of the eclipse. Our observations span the lower  $5\sigma$  phase range and upper  $2\sigma$  phase range over the RV distribution.

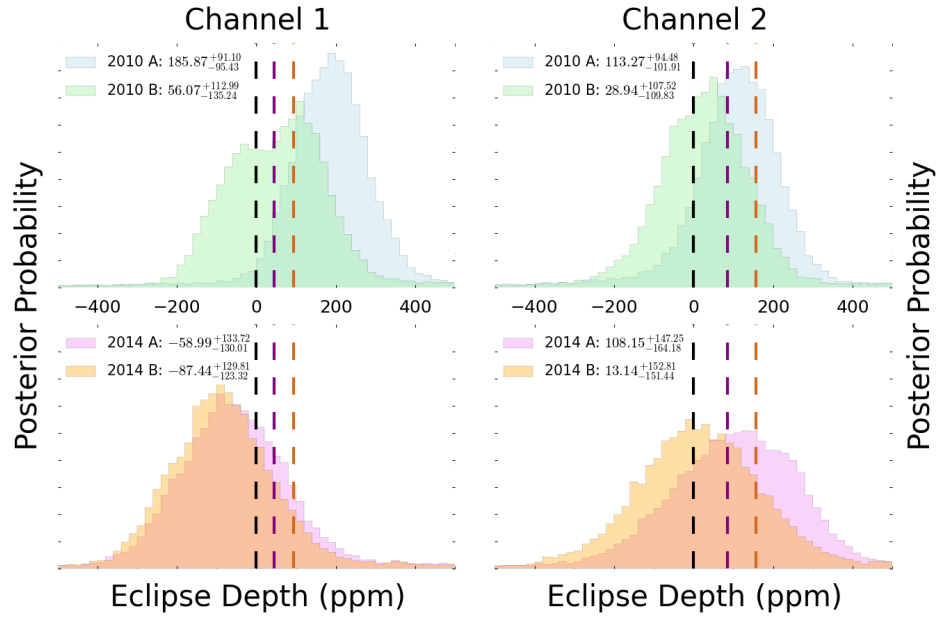


Figure 4.8: Markov Chain Monte Carlo (MCMC) Posterior probability distributions for the eclipse depth during our 8 independent epochs of warm Spitzer-IRAC observations. All 8 posteriors are consistent with the null hypothesis, no eclipse, to within  $2\sigma$ . (Left) Posteriors represent Channel 1 ( $3.6 \mu m$ ) and (Right) Posteriors represent Channel 2 ( $4.5 \mu m$ ). (Top) Posteriors represent our 2010 observations (without PEAK-UP) and (Bottom) Posteriors represent our 2014 observations (with PEAK-UP). The purple and brown dashed lines represent the black body predicted eclipse depths, assuming equilibrium temperatures of  $T_{eq} = 878K$  and  $T'_{eq} = 1044K$  for uniform redistribution (purple) and instantaneous re-radiation (brown), respectively. In the case of uniform redistribution (straight line), HAT-P-11b has an equilibrium temperature of  $T_{eq} = 878 \pm 15K$  [102]. The equilibrium temperatures predict eclipse depths of  $\delta_{3.6} \sim 45 \text{ ppm}$  &  $\delta'_{3.6} \sim 94 \text{ ppm}$  ( $3.6 \mu m$ ) and  $\delta_{4.5} \sim 86 \text{ ppm}$  &  $\delta'_{4.5} \sim 156 \text{ ppm}$  ( $4.5 \mu m$ ). We conclude that we did not detect an eclipse in any of our 8 observations.

#### 4.4.3 Deriving Eclipse Depth Upper Limits

We used an affine invariant, Bayesian MCMC framework [68, 134] to generate robust posterior distributions and constrain upper limits on the eclipse depths at

each phase in our warm Spitzer-IRAC observations. Figure 4.8 shows the MCMC posterior distributions from the “best-fit” aperture radii light-curve (see Table 4.1). The MCMC posterior distributions include the null hypothesis ( $\delta = 0$ ) to within 1-2 $\sigma$ . Figure 4.8 shows eclipse depths from black body flux at the equilibrium temperature predictions for HAT-P-11b (dashed lines).

Table 4.2: List of eclipse depth upper limits and black body predictions for both uniform redistribution and instantaneous re-radiation.

Epoch	Start Date	Wavelength [ $\mu m$ ]	Uniform	Instantaneous	MCMC
			Redistribution [ppm]	Re-Radiation [ppm]	Upper limits [ppm]
115	2009-Dec-05	3.6	45	86	$41^{+69}_{-66}$
161	2010-Jul-18	3.6	45	86	$186^{+91}_{-95}$
171	2010-Sep-05	4.5	94	156	$113^{+95}_{-102}$
195	2010-Dec-31	3.6	45	86	$56^{+113}_{-135}$
199	2011-Jan-19	4.5	94	156	$29^{+108}_{-110}$
460	2014-Jul-19	4.5	94	156	$108^{+147}_{-161}$
461	2014-Jul-23	3.6	45	86	$-59^{+134}_{-130}$
462	2014-Jul-28	4.5	94	156	$13^{+153}_{-151}$
467	2014-Aug-22	3.6	45	86	$-87^{+130}_{-123}$

Markov Chain Monte Carlo (MCMC) is a selection technique used in a statistical, machine learning framework that iterates over a given set of parameters to maximize the likelihood space with respect to a given prior. The likelihood is a measure of the probability that the data were sampled from a specific model distribution. The prior is the quantification of our background knowledge of the physics surrounding our observations – e.g. eccentricity is confined between zero and one for a gravitationally bound object. In the presence of noise, we relax many of the physically motivated prior conditions and allow the MCMC to walk through un-

physical values to properly characterise the limitations of fitting for small signals in the presence of noise. Our MCMC posterior distributions, Figure 4.8, span both physical ( $\delta \geq 0$ ) and unphysical ( $\delta < 0$ ) regimes, which provided more robust constraints on the upper limits of our eclipse depths (see Table 4.2). For the eclipse light curves, we fit for the PLD basis coefficients, polynomial coefficients, and the eclipse light curve parameters – eclipse depth,  $\delta$  and the eccentricity,  $e$ , but held all other parameters constant.

We initialised our MCMC chains using linear matrix inversion to establish the ideal minimum  $\chi^2$  solutions. This became the initial conditions for our maximum likelihood estimates (MLE), using a built-in Python optimization routine [114]. Finally, the solutions derived from our MLE analyses became the initial conditions for our MCMC routine (Figure 4.8). We implemented the public MCMC routine, *emcee*, developed by [60]. *emcee* uses an affine invariant ensemble MCMC solver developed by [134]. An ensemble solver is an algorithm that iterates many, interacting MCMC chains simultaneously. Affine invariant refers to the mathematical technique that [134] developed for determining the next step in the ensemble chain by topologically remapping the N-dimensional parameter space into a convex pseudo-parameter space, which the algorithm could then more easily interpret for correlations between steps in the chains over the physical parameter space [60, 134, 135]. We used a Gaussian likelihood function ( $\chi^2$ ) and a uniform prior for all MCMC analyses.

#### 4.4.4 Bayesian Information Criterion

When comparing multiple models and observations,  $\chi^2$  becomes ambiguous over changes in degrees of freedom,  $\nu$ . For example, if we fit a quadratic model ( $\nu = 3$ ) to a data set, the fit will always be better than a straight line fit ( $\nu = 2$ ) because the quadratic model has more degrees of freedom. To confirm that we did not detect an eclipse, we examined histograms for our 8 observations for all values  $b$  and  $c$  using the Bayesian Information Criterion (BIC) as our metric [116].

$$BIC = \chi^2 + k \log N \quad \text{and} \quad \Delta BIC = BIC_{no-eclipse} - BIC_{eclipse} \quad (4.10)$$

Because we compared each  $BIC$  to the same observations, we set  $N_e = N_{ne}$ . We were then able use the following equation as our metric for detection of an eclipse:

$$\Delta BIC = \chi_{ne}^2 - \chi_e^2 + (k_{ne} - k_e) \log N \quad (4.11)$$

This metric examined the difference between “no eclipse” ( $BIC_{ne}$ ) and “with eclipse” ( $BIC_e$ ). When considering an eclipse model, we fit for an extra 2 parameters (i.e  $e$  and  $\delta$ ), therefore  $(k_{ne} - k_e) = -2$ . Figure 4.9 examines the distribution of  $\Delta BIC$  as a set of histograms over each set of 176 photometric light curves. If adding a [88] eclipse curve did not effect the  $BIC$ , then these histograms would be centered around zero, the null hypothesis. If adding an eclipse model improved the BIC results, then the  $\Delta BIC$  distribution would be significantly above the null hypothesis line ( $\delta = 0$ ) [75, 116]. Figure 4.9 shows that for the distribution of our photometric light curves, the  $\Delta BIC \sim 0$ , which implies that adding an eclipse model did not improve the quality of fit – primarily reducing it– and confirmed that we did not

detect an eclipse in any of our observations.

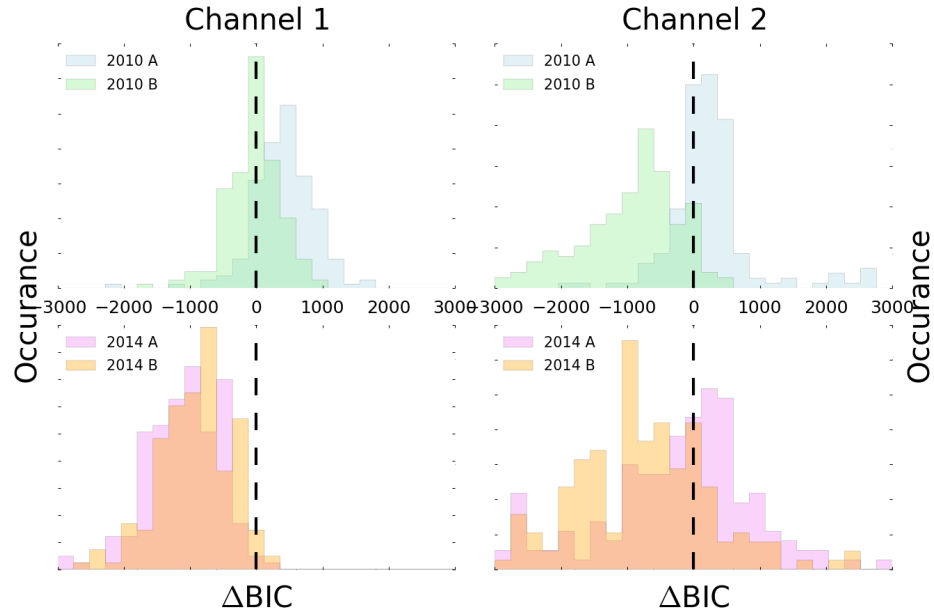


Figure 4.9: Distribution of change in the Bayesian Information Criterion  $\Delta BIC$  over the 176 photometric light curves between models with an eclipse and models without an eclipse. If we had detected an eclipse in our observations, then the  $\Delta BIC$  associated with the detection would be distinctly positive. If adding a [88] eclipse curve did not effect the  $BIC$ , then these histograms would be centered around zero, the null hypothesis. If adding an eclipse model improved the  $BIC$  results, then the  $\Delta BIC$  distribution would lie significantly above the null hypothesis line ( $\delta = 0$ ) [75, 116]. Because all of our photometric light curves have  $\Delta BIC \sim 0$ , implying that adding an eclipse model did not improve the quality of fit – primarily reducing it–, we confirm that we did not detect an eclipse in any of our observations.

## 4.5 Conclusions

Exoplanet atmospheres can provide a probe of planet formation and evolutionary processes. Eclipse photometry is a technique to measure the brightness temper-

ature averaged over the detector bandpass. We can model brightness temperature at multiple wavelengths to understand the atmospheric metallicity, molecular abundances, and temperature-pressure profiles of exoplanet atmospheres, which could allow us to understand the end results of planet formation processes.

Spitzer-IRAC wavelengths are especially useful for measuring the relative abundances of  $CH_4$  and  $CO$  in exoplanet atmospheres, which could in principle provide useful measurements of the  $C/O$  ratio and atmospheric metallicity; both are probes of the atmospheric formation conditions in its natal environment and post-formation evolution. Thermochemical equilibrium predicts that planets with temperatures  $T_p < 1000K$  could have strong  $CH_4$  absorption at  $3.3\mu m$ . Comparing eclipse depths at  $3.6$  and  $4.5 \mu m$  could thus provide constraints on the above planet formation metrics.

The Kepler space mission revealed that the bulk population of planets in our galaxy are “small” ( $R_p < 4R_\oplus$ ). HAT-P-11b would provide an excellent case study for the upper limit of this regime ( $\sim 4.5 R_\oplus$  &  $\sim 27 M_\oplus$ ); simultaneously providing a “small” planet with an observable atmosphere. Our team recently measured water absorption through transmission spectroscopy in the upper atmosphere of HAT-P-11b.

We observed the transiting warm Neptune, HAT-P-11b, using warm Spitzer-IRAC at  $3.6$  and  $4.5 \mu m$ , over a large range of orbital phase in search of the exoplanetary eclipse. We analysed the archival, “find the eclipse” data using our new PLD algorithm to search for the eclipse, and detected a preliminary eclipse at a phase of  $\sim 0.69$ . We then re-observed this system using warm Spitzer-IRAC, near

phase  $\sim 0.69$ , but were unable to confirm the eclipse in any of our nine epochs – 5 archival observations from 2010 (PI: Richard Barry) and 4 new observations from 2014 (PI: Heather Knutson). We did not detect the eclipse at any phase in our observational range. This phase range encompassed 97.5% ( $2\sigma$  upper limit &  $5\sigma$  lower limit) of the radial velocity (RV) predicted range for the eclipse to occur.

We derived upper limit estimates using warm Spitzer-IRAC at  $3.6$  &  $4.5 \mu m$  for HAT-P-11b. We focused closely on 4 prospective detections at phases  $\sim 0.56$ ,  $\sim 0.69$ ,  $\sim 0.64$ , and  $\sim 0.66$ ; Figure 4.8 examines the MCMC posteriors each of these phases. The predicted, black body eclipse depth for HAT-P-11b was  $\sim 45$  ppm ( $\sim 94$  ppm) and  $\sim 87$  ppm ( $\sim 156$  ppm) at  $3.6$  and  $4.5 \mu m$ , respectively, assuming uniform redistribution (instantaneous re-radiation). We showed that these predictions are within the uncertainties derived from our nine observations, and are equally as likely as the null hypothesis,  $\delta = 0$ , or no detection. It is still possible that the eclipse occurred outside of our observational phase range. More recent RV results imply that it is more likely that the eclipse occurred during our observations, but below the detection threshold allowed by the warm Spitzer-IRAC noise profile. We examined the noise profile of Spitzer-IRAC in detail, using our new PLD decorrelation method, and were unable to confirm any prospective detections to better than  $2\sigma$ .

## Chapter 5: Ground Based Spectroscopic

### Surveys of Exoplanetary Atmospheres

#### 5.1 Introduction

The science of extrasolar planets provides context for our own origins. If we constrain the underlying physics of planet formation from a statistically significant population of exoplanets, we could better understand how our own Solar System formed and evolved. To understand the bulk processes of planet formation and evolution, we must analyse a sample of planets formed around stars that are both different and similar to our own. For example, the Kepler Space Telescope – a four year mission that discovered over 4000 planet candidates and over 1000 confirmed planets – concluded that the significant majority of exoplanets are small planets ( $R < 4R_{\oplus}$ ) [55, 56, 73]. Small planets form efficiently around small stars; [72] find that M-dwarfs host planets that have radii  $R_p < 4R_{\oplus}$ , with an occurrence rate of  $0.9_{-0.03}^{0.04}$  planets per M-dwarf – the upper limit assumes that Kepler’s detectable range in period is representative of planet formation physics.

The most accepted planet formation theory, “core accretion” hypothesizes that planets are built from the inside out. It predicts that small planets should

have larger ratios of core mass to atmospheric mass (smaller scale heights) than large planets [1, 4]; that is, protoplanets with a larger core mass are able to accrete larger amounts of hydrogen, which would decrease their atmospheric mean molecular weight,  $\mu_p$ , and increase their scale height,  $H_p$  – at a given temperature. “Core accretion” theory predicts that protoplanets with small core masses would only be able to accrete small amounts of hydrogen, increasing  $\mu_p$  and decreasing  $H_p$  [5, 52].

Figure 5.1 shows predictions for the atmospheric metallicity (the ratio of heavy elements relative to hydrogen in the atmosphere,  $Z \propto H_p^{-1}$ ) as a function of planetary mass from Fortney et al. 2013 [52] population synthesis models. The distinct trend between  $M_p \approx 30 - 300M_\oplus$  that defines the “transition region” between small and large planetary masses can be seen in Figure 5.1. For large planetary masses, the atmospheres are predicted to be hydrogen dominated (i.e. low atmospheric metallicity and large scale heights); and, for small planetary masses, the atmospheres have a large degeneracy over atmospheric metallicity, with a concentration nearly  $Z = 1$  (i.e. large atmospheric metallicity and small scale heights). The red and blue points represent distinct populations of source particles for the growth of the planetary embryos; red = 1 km and blue = 100 km. The transition region from  $M_p \approx 30 - 300M_\oplus$  provides a prospective observational test for planet formation theories such as core accretion [1, 4, 5, 52].

Figure 5.2 shows the distributions of mass and radius for 200 transiting exoplanets. The positive trend between mass and radius from 1 - 300 Earth masses coincides with predictions from core accretion. These measurements confirm the trend for medium and large planets [5, 22], but reveal the degeneracy between the

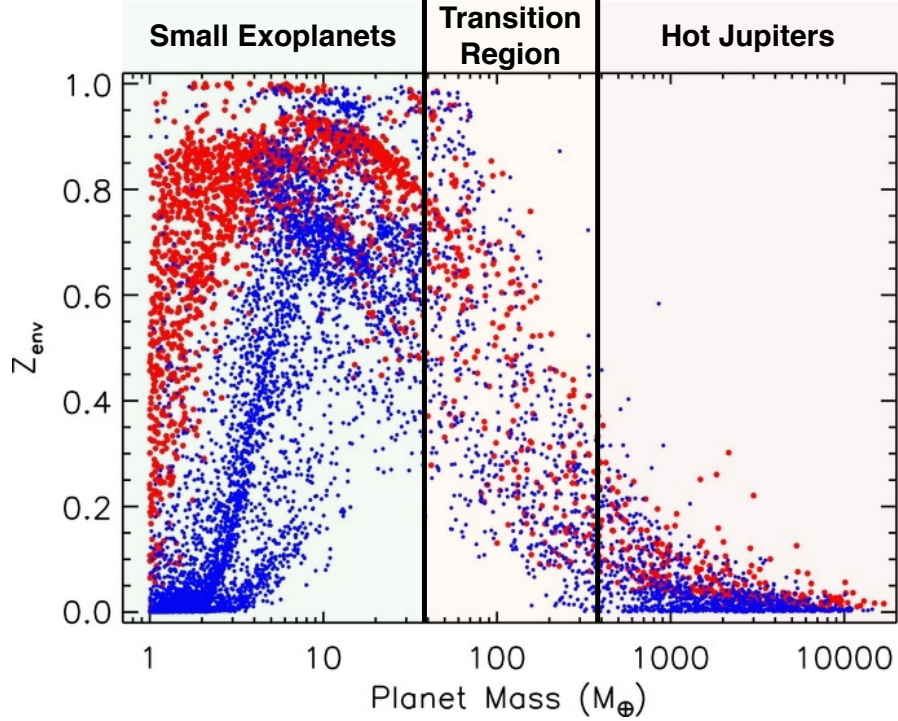


Figure 5.1: [52] plotted the mass and atmospheric metallicity,  $Z_{env}$ , for a large population of exoplanets built from population synthesis models using core accretion simulations. The segment colors are associated with the independent exoplanet mass regimes: Small Exoplanets ( $< 30M_{\oplus}$ ), giant planets ( $> 300M_{\oplus}$ ), and the transition region ( $30 - 300M_{\oplus}$ ). The color of the points is associated with a different population of seed particles. Blue dots use 100 km planetesimals and red dots use 1 km planetesimals. They predict a strong correlation between hydrogen envelope fraction and planetary mass. By focusing our surveys on this transition region, we can constrain the evolution of atmospheric metallicity over planetary mass.

atmospheric mass and core mass for small planets. In the small planet regime, several compositions and internal structure models coincide with each mass and radius measurement. The bulk density of medium and large planets is distributed near that of Saturn and Jupiter (i.e. hydrogen-dominated); but mass and radius measurements of small planets compared with bulk density models cannot uniquely

define the internal structures (i.e. core mass to atmospheric mass ratio) [5, 22]. They are degenerate between rocky cores with hydrogen envelopes and volatile rich cores with heavy (volatile rich) atmospheres; some measurements in this regime even coincide with pure rock or ice models, without an atmospheric envelope being necessary.

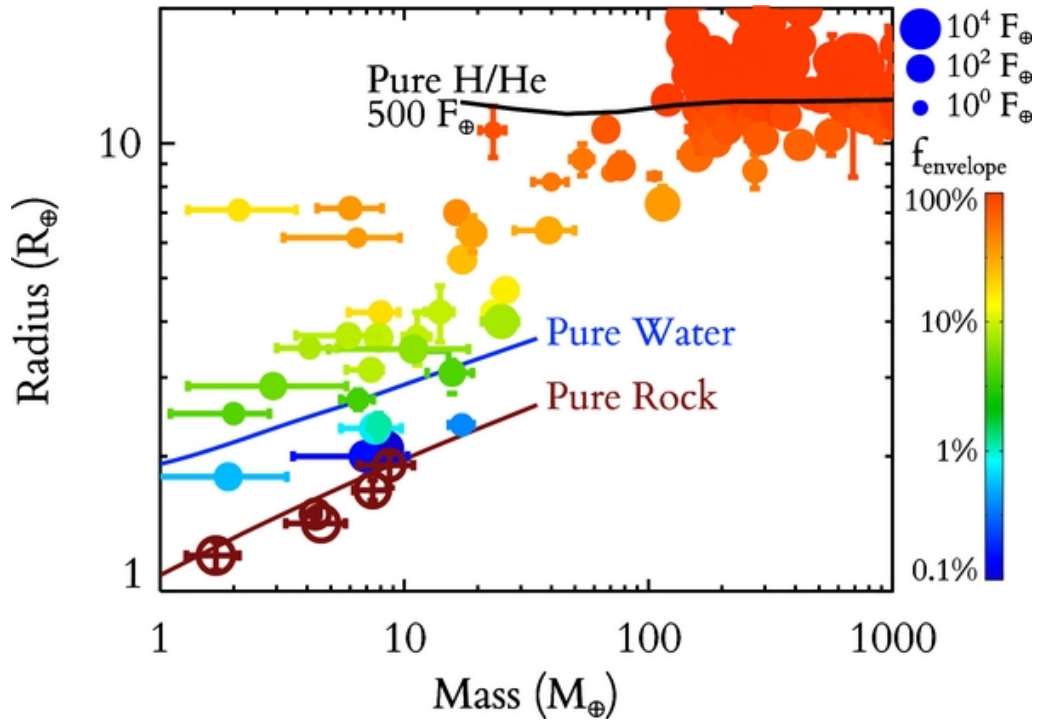


Figure 5.2: Lopez & Fortney (2014) [5] plotted the mass and radius of 200 transiting exoplanets. The color is associated with the predicted hydrogen envelope fraction,  $f_{envelope}$  ( $\sim$  inverse of atmospheric metallicity), derived from internal structure models. The marker size corresponds to the stellar insolation with respect to the Earth. They predict a strong correlation between hydrogen envelope fraction and planetary mass over the region from 30 - 300  $M_{\oplus}$ . My observations will test this prediction by constraining the existence and significance of such a correlation. By focusing on this transition region, we can track the evolution of atmospheric metallicity over planetary mass.

With our current technology, the most readily available measurement to un-

cover this degeneracy is transmission spectroscopy of these exoplanetary atmospheres to measure the scale heights and constrain the atmospheric mean molecular weights. Transmission spectroscopy consists of spectroscopically observing the host star as the exoplanet passes between our detectors and the star, constraining the planetary transit depth as a function of wavelength [7, 8]. If molecules exist in the optically thin part of the planetary atmosphere (above any cloud decks), and the atmosphere is sufficiently light (large scale heights relative to measurement precision), then we can constrain the abundance of the absorbing species by measuring variations in transit depth,  $\frac{dD_\lambda}{d\lambda}$ , near molecular or atomic absorption features. We define the transit depth as the ratio between the flux absorbed by the planet in-transit,  $F_{OOT} - F_{IT}$ , relative to the flux out-of-transit,  $F_{OOT}$ . As the planet passes between our detectors and the host star, the transit depth becomes

$$D_\lambda = \frac{F_{OOT}(\lambda) - F_{IT}(\lambda)}{F_{OOT}(\lambda)} = \left(\frac{R_p}{R_s}\right)^2 + 2\epsilon_\lambda \left(\frac{R_p}{R_s}\right) \left(\frac{H_p}{R_s}\right) (1 - e^{-\tau_\lambda}) \quad (5.1)$$

and the transmission spectrum becomes,

$$\frac{dD_\lambda}{d\lambda} = 2\epsilon_\lambda \left(\frac{R_p}{R_s}\right) \left(\frac{H_p}{R_s}\right) e^{-\tau_\lambda}. \quad (5.2)$$

$\tau_\lambda$  represents the wavelength dependent optical depth discussed in Chapter 1:  $\tau_\lambda = \int_x \rho \kappa_\lambda dx$ ;  $\epsilon_\lambda$  represents the number of scale heights over which the atmosphere is opaque because the atmospheric absorption cross sections peak at wavelength  $\lambda$  (e.g.  $\epsilon_\lambda$  is large at 589 nm if Na is observable in the atmosphere). We theoretically predict that  $\langle \epsilon_\lambda \rangle \sim 5$  for a hydrogen dominated, clear atmosphere [3, 30, 33, 34]. Empirically, many teams have measured  $\langle \epsilon_\lambda \rangle \sim 2$  for exoplanet atmospheres [3, 30, 33, 34]. In

the event that a cloud/haze layer exists over the observational regime ( $\sim 1$  mbar) or the atmosphere is significantly dense (i.e. small scale height), then  $\tau_\lambda \gg 1$  and the transmission spectrum would be featureless, because  $\langle \epsilon_\lambda \rangle \sim 0$  within the observational precision.

Recent studies have inferred that opaque, low pressure clouds in exoplanets could be more prevalent than predicted from extrapolations of Solar System analogues [17–19, 45]; and, these clouds are most likely composed of refractory materials (e.g. ZnS or MgSiO<sub>3</sub>), unlike the volatile rich clouds in our own Solar System (e.g. H<sub>2</sub>O, CO<sub>2</sub>, or NH<sub>3</sub>) [17, 49]. These observations showed that smaller Super Earth and Neptune-sized exoplanets have cloud-tops or haze layers at significantly lower pressures than the larger Jupiter-sized exoplanets, resulting in opaque atmospheres over the observational regime for our detectors [19, 33, 45, 100, 111]. Both high atmospheric metallicity (small scale height) and cloud/haze layers can increase the opacity of the atmosphere at low pressures, especially within our observational regime [8, 18]. In all but one small exoplanet (i.e. HAT-P-11b, Fraine et al., 2014), the atmospheres were found to be opaque, producing a featureless transmission spectra in the near infrared using Hubble Space Telescope Wide Field Camera 3 (HST-WFC3) [19, 30, 36, 45, 100, 111].

Although planet formation theories like core accretion predict the observed relationship between planetary masses and radii (discussed above), the ratio between the atmospheric mass and the core mass for small planet planets (the bulk of planet formation) is still unconstrained. This ratio could reveal the efficiency of both the formation processes – how much hydrogen was accreted from the protoplanet-

tary disk – and post-formation evolution, such as accreting comets and asteroids after formation [47]. Spectroscopically detecting molecules from exoplanetary atmospheres would constrain this ratio by measuring the scale height and inferring the atmospheric hydrogen fraction (see Figure 5.2) [3, 9, 10, 30, 42, 46]. The ability to detect molecular absorption through transmission (i.e. from molecules like  $H_2O$ ,  $CH_4$ , or  $CO$ ), implies that the atmosphere must be light enough to sustain a large scale height (see below). The significance of spectroscopic features through transmission (adapted from Equation 2) is directly related to the scale height and mean molecular weight as

$$\frac{dD}{d\lambda} = \alpha_\lambda H_p = \alpha_\lambda \frac{kT_p}{\mu_p g_p} \quad (5.3)$$

This equation shows that  $\mu$  is inversely proportional to the significance of the transmission spectrum; note that  $\alpha_\lambda$  is directly proportional to the significance of the molecular absorption over wavelength. If  $\mu$  is small enough (i.e.  $\mu \sim 1$ ), then the atmosphere is likely to be hydrogen-rich. If we are able to estimate the atmospheric temperature profile,  $T(P)$ , and spectroscopically detect a molecular feature,  $\frac{dD}{d\lambda}$ , then we would be able to constrain the mean molecular weight from the atmospheric scale height.

## 5.2 Observations

My team and I used both space and ground based spectroscopic observations to detect molecular and atomic absorption features and constrain the atmospheric

metallicity over a range of planetary masses [30, 33, 36, 46]. Constraining the scale height, and thereby the core-to-atmospheric mass ratio, over a range of planetary masses could allow us to understand how much hydrogen planets accrete during formation as a function of planetary embryo mass [5, 22, 52]. Spectroscopic observations serve to probe the atmospheric scale heights of exoplanets [3, 5, 9, 10]. [52] show that focusing surveys on the mass range  $M_p \sim 30 - 300 M_\oplus$  could constrain this trend over the “transition region” and infer the efficiency of planet growth during formation (see Figure 5.1).

In addition to the planetary scale height,  $H_p$ , the apparent magnitude and radius of the host stars are critical parameters in predicting whether an exoplanetary atmosphere is amenable to spectroscopic observations with current technology [15, 28, 34, 77]. Hot Jupiters with clear atmospheres have scale heights on the order of  $H_{HJ} \sim 550$  km. For a nominal hot Jupiter ( $T = 1500$  K) orbiting a solar-type star,  $\frac{\Delta D}{\Delta \lambda} \sim 10 \left(\frac{R_p}{R_s}\right) \left(\frac{H_p}{R_s}\right) \sim 600$  ppm. For a nominal exo-Neptune ( $T = 1500$  K) orbiting a solar-type star,  $H_{EN} \sim 275$  km and  $\frac{\Delta D}{\Delta \lambda} \sim 200$  ppm. HST-WFC3 can attain spectroscopic precision down to  $\sim 25$  ppm for bright host stars or by combining multiple transits [19, 30, 33, 45, 111]; ground based telescopes are currently able to attain precisions of  $\sim 100$ - $200$  ppm for bright host stars, enabling us to study hot Jupiter atmospheres and detect exo-Neptune atmospheres [30, 33, 46].

Because small planets ( $R_p < 4R_\oplus$ ) comprise the majority of known planets in the galaxy, it is important to detect molecules on small planets and constrain their scale heights over a range of planetary masses [5, 52]. The detection of opaque exoplanetary atmospheres inhibited our instruments from detecting spectroscopic

features on many of these targets, which would otherwise have been observationally amenable with current technology [19, 30, 45, 111]. A lack of spectroscopic features (null hypothesis) is predicted for atmospheres with high altitude cloud or haze layers and high mean molecular weight (large atmospheric metallicity; small scale height).

Models that include atmospheric metallicity and the pressure associated with a cloud/haze layer in the atmosphere are strongly correlated [18, 19, 30, 45]. [45] was able to show that clouds were far more likely to explain the opaque atmosphere of the transiting Super Earth GJ 1214b. Although, the moderate planetary bulk density ( $\rho_p \sim 2g/cm^3$ ) is less likely to sustain a large hydrogen envelope ( $\rho_{HJ} \sim 1g/cm^3$ ). [19] presented results for the opaque atmosphere of GJ 436b (a transiting warm-Neptune), but was unable to constrain the atmospheric metallicity as strongly as for GJ 1214b and, instead, probed the degeneracy of cloud top pressure with atmospheric metallicity [9, 10, 18]. [30] was able to detect absorption from water vapour in the transiting warm-Neptune HAT-P-11b. The HST-WFC3 transmission spectrum for HAT-P-11b provided more precise constraints for the intrinsically degenerate cloud top pressure and atmospheric metallicity, compared to the opaque atmospheric non-detections discussed above. Unfortunately, stellar activity inhibited Fraine et al. 2014 from measuring the atmospheric scale height, such that they provided upper limits related to the detection of water vapour alone; the atmosphere of HAT-P-11b must be light enough (i.e. a sufficiently large scale height) for any molecular detection to be observed.

As discussed above, detecting molecular species in the upper atmospheres of exoplanets places constraints on their scale height. Because scale height is an

intrinsic property of the atmosphere, we can observe these planets in many different molecular or atomic absorption bands and constrain the scale height from a range of detectors. Specifically, the Hubble Space Telescope Wide Field Camera 3 (HST-WFC3 or just WFC3) was very useful in recent years for detecting water absorption on hot Jupiters and a warm Neptune [30, 32, 33, 136]. It is especially useful with the new observational mode, “Scanning Mode”, for planets orbiting host stars with bright H-band magnitudes. [30] reached up to  $\text{SNR} \sim 2 \times 10^4$  per wavelength channel (average precision of 50 ppm) with HAT-P-11 ( $H_{mag} = 7.6$ ).

### 5.2.1 Spectroscopic Surveys for Exoplanetary Atmospheres

There are several ongoing programs to target a large number of exoplanets, with predicted scale heights that are in the regime necessary to detect molecular features through transmission. I am one of the founding members of the ACCESS collaboration – Arizona-CfA-Católica Exoplanet Spectroscopy Survey. The ACCESS collaboration combines the proprietary telescope time from the CfA, Arizona, Católica, Carnegie, and MIT, as well as theoretical support from UCSC, Caltech, and STScI. We utilize the IMACS and MMIRS multi-object spectrometers on the twin, 6.5m Magellan Baade and Clay, respectively, to build a catalog of transmission spectra for exoplanets ranging between  $M_p \sim 7 - 300 M_{\oplus}$ . The combination of optical and near infrared observations provides a wide wavelength coverage, which is useful to robustly model these exoplanetary atmospheres [3, 10, 18, 20, 21].

IMACS – Inamori-Magellan Areal Camera & Spectrograph on Magellan [137]

– has the sensitivity to observe Na & K atomic transitions in exoplanetary atmospheres at 589 nm and 769 nm, respectively; we can also detect Rayleigh scattering – through an increase in transit depth at short wavelengths [46]. Our pilot paper [46] studied WASP-6b and detailed the utility and systematics of IMACS as a survey telescope (see Figure 5.3b). ACCESS is the first, large scale, ground based, optical, spectroscopic survey for exoplanetary atmospheres. We are a discovery based survey seeking to uncover trends in the exoplanet spectra as a function of planetary mass, focusing on small to medium mass planets.

Observing the Na & K atomic transitions for hydrogen-dominated worlds could also provide a constraint on the atmospheric temperature [42, 46] by comparing the width and depth of the atomic lines across a range of models with variable temperature predictions. Atmospheric temperature is predominantly measured through emission in the infrared by detecting the eclipse of the exoplanet passing behind its host star [11, 54]. Optical transmission spectra are able to constrain the temperature for hydrogen-dominated worlds, because the scale height uniquely defines the shape of the atomic absorption lines [42, 46]; see Equation 5.3. Assuming that the planet is primarily composed of hydrogen implies that  $\mu_p = 1$  and that the scale height is directly proportional to the temperature of the atmosphere:  $H_p = \frac{k_b}{g_p} T_p$ . The detection would require a large signal-to-noise observation from the clear atmosphere of a transiting exoplanet.

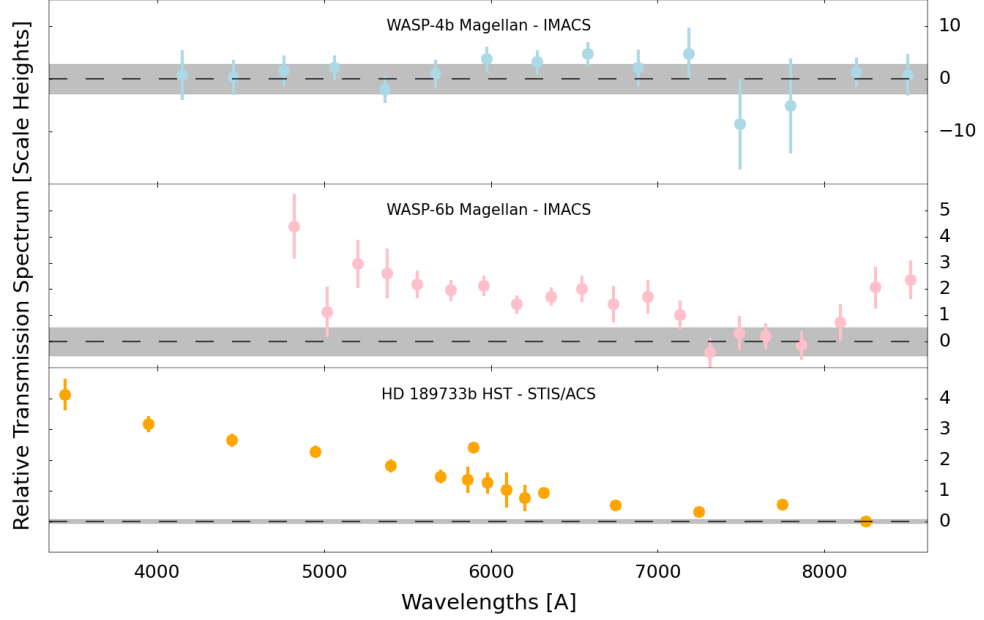


Figure 5.3: Comparison between the optical spectra of WASP-4b (top; our new observations), WASP-6b (middle; [46]), and HD 189733b (bottom; [40]). The top and middle spectra were observed from Magellan with IMACS, a multi-object, optical spectrometers mounted onto the 6.5m Baade Telescope. The HST-STIS transmission spectrum of HD 189733b (bottom) shows a robust Rayleigh scattering feature that infers the existence high altitude dust scattering light away from our detectors. The Magellan-IMACS transmission spectrum of WASP-6b also shows a distinct rise in transit depth that is inversely correlated with wavelength. The spectra for WASP-4b (top) does not exhibit any spectroscopic features or Rayleigh scattering slope. This is representative of a high altitude cloud layer that increased the optical depth throughout our observational regime, obscuring any detection of molecular absorption features.

### 5.2.2 Multi-Object Spectroscopy

Ground-based observatories provide access to significantly larger telescopes with both optical and NIR instruments to collect many more photons through a suite of photometric and spectroscopic detectors. The ultimate limiting factor in any spectroscopic analysis is the number of photons collected. For all ground-based telescopes, the most significant limiting factor is the Earth’s atmosphere, which introduces a  $\sec(z)$  effect. As  $z$  increases, the number of photons absorbed or scattered by the atmosphere also increases.  $z$  is referred to as “air mass”, the ratio of the amount of mass of atmosphere that the stellar light path travels through, relative to when the telescope is targeting zenith.

Because the effect of the Earth’s atmosphere is chromatic, we use multi-object spectroscopy to compare the effects of the airmass on our target star with respect to those stars along similar light paths. We use machine learning algorithms to combine the measured light signatures and form a wavelength dependent solution to decorrelate the effect of Earth’s atmosphere from our exoplanetary spectrum [28,77]. [46] used multi-object spectroscopy with IMACS to measure the stellar spectrum for WASP-6 (the target star) at the same time as 7 nearby star in the same field of view. By sampling the stellar spectra along the same atmospheric column, [46] compared common mode variations over time (per wavelength channel) between the target and comparison stars. In addition to the noise signature from the Earth’s atmosphere, IMACS also introduced correlated noise signatures that varied the flux read per wavelength channel over time. [46] used a dual PCA-Wavelet analysis and

built a noise model function to decorrelate both the atmospheric and instrumental noise profiles simultaneously with the astrophysical and planetary signatures. In the next section, I will adapt the analysis presented in [46] for our new observations of WASP-4b.

### 5.2.3 ACCESS Observations of WASP-4b

Our collaboration used Magellan-IMACS to observe the transiting hot Jupiter WASP-4b twice, and expect to combine these observations with a third transit in Sept 2015. The first observation (UT 09-2015) sustained engineering difficulties for the first half of the transit because the calibration mask was in place during the science observations. I will present here our preliminary analysis of the second epoch using IMACS to observe WASP-4 (UT 2013-10-18).

We took 494 spectra of WASP-4 simultaneously with 12 comparison stars for spectroscopic calibration. Our observations were taken on UT 10-18-2013 using the f/2 camera on IMACS. The f/2 provided an unvignetted circular field of view of radius  $r \approx 12'$ . This large field of view provided 12 comparison stars of similar magnitude and color. The median cadence for our observations was 58s, ranging from 55s to 68s. We varied the integration time to maintain constant ADU counts of  $\approx 36000$  ( $\sim 55\%$  saturation) for our target star.

Of our 12 comparison stars that we monitored, two comparison stars saturated on the detector, and we were unable to robustly derive wavelength calibrations for two other calibration stars; this left 8 calibration stars that were spectroscopically

well calibrated and unsaturated. The 8 remaining comparison stars accumulated enough signal-to-noise over the same wavelength range of interest ( $\sim 450 - 880$  nm) as our target star (WASP-4). To avoid slit loss and collect the maximum possible number of photons that passed through the planetary atmosphere, each star was observed through a 20" x 20" slit. These wide slits captured the majority of the light from IMACS's PSF, for the extent of the observations.

Prior to our science observations, we also took several calibration frames, including 20 HeNeAr arc lamps (using 0.7" wide slits), 10 quartz spectroscopic flat fields (before and after science observations), and 40 dark frames to calibrate the wavelength dispersion, sensitivity variations, and thermal background for each comparison star across the detector, respectively. We used the same analysis pipeline for WASP-4 as [46] used for WASP-6 (described therein).

### 5.2.3.1 White Light Curve

After we calibrated the target star and each of the 8 comparison stars, we integrated in the spectral dimension to create the "white light" curves (WLCs) for our target star and all 8 comparison stars. The target star's WLC contains the orbital,  $(P, \frac{a}{R_s}, i, e, \omega)$ , and temporal,  $T_c$ , information, as well as the Earth's average atmospheric noise profile and IMACS's instrument noise profile. The comparison stars' WLCs contain only Earth's atmospheric and IMACS's instrument noise profiles. We used a Markov Chain Monte Carlo (MCMC) approach to fit a [88] model, in the time domain, on top of a PCA-Wavelet based noise model [46, 117] that searched for

common mode noise sources in the comparison stars to divide out of the target star. Because the orbital and temporal information is achromatic, we held these variables constant for our spectroscopic, light curve analysis (discussed below).

### 5.2.3.2 Transmission Spectrum and Chromatic Noise

The planetary transmission spectrum is measured as variations in the transit depth as a function of wavelength. To extract the wavelength dependent planetary spectrum of WASP-4b, we used a similar MCMC approach and fit a [88] model to each wavelength bin ( $\sim 30$  nm wide), using theoretically calculated limb darkening coefficients and the set of orbital and temporal parameters derived from our WLC analysis (discussed above). Figure 5.3 shows the wavelength dependent transit depth of WASP-4b, WASP-6b [46], and HD 189733b [40] as a function of their individual scale heights.

WASP-6b (measured with Magellan-IMACS) and HD 189733b (measured with HST-STIS) show a robust increase in the transit depth with a decrease in wavelength (see Figure 5.3). [46] and [40] independently compared atmospheric models to this negative, spectral slope and concluded that Rayleigh scattering was the most appropriate explanation for this feature. Many solar system planets also exhibit Rayleigh scattering as a slope in optical spectra, including the Earth [138–144]. Rayleigh scattering becomes dominant at a wavelength that is directly related to the size of the particle scattering the light. For the Earth, Rayleigh scattering begins to be apparent at short wavelengths  $< 500$  nm, implying that the scattering is caused

by molecules in the atmosphere. For WASP-6b and HD 189733b, the Rayleigh scattering is dominant at longer wavelengths ( $< 1 \mu m$ ), implying that dust in the atmosphere is the more likely cause of the scattering [40, 46]. The significance of the Rayleigh scattering in WASP-6b and HD 189733b covered  $\sim 4$  scale heights. Spectroscopic features from a clear atmosphere with solar composition (i.e. the abundance of all elements relative to hydrogen is the same as that of our Sun) are expected to vary over  $\sim 5$  scale heights (see Equation 2) [33, 34].

We did not detect any spectroscopic features or slope in our WASP-4b observations (see Figure 5.3). The wavelength dependent transmission spectrum for WASP-4b is featureless from 400 nm to  $1 \mu m$ . Comparing the short (400 - 700 nm) versus long (700 nm -  $1 \mu m$ ) wavelength channels, the spectrum results in a  $\sim 0.3$  scale heights, with an uncertainty of  $\sim 4.6$  scale heights. we can rule out a nominal Rayleigh scattering model – spanning 5 scale heights over our wavelength range – to  $1.8\sigma$ ; where, the significance [19] is calculated as

$$\text{Significance} = \frac{\chi_{\text{obs}}^2 - \langle \chi^2 \rangle}{\sigma} == \frac{\chi_{\text{obs}}^2 - \nu}{\nu} \quad (5.4)$$

where  $\nu$  is the degrees of freedom in the fit. We compute a value of  $1.8\sigma$  from the  $\chi^2$  of the nominal Rayleigh scattering model.

The analysis discussed above is preliminary; we intend to examine more noise models and raw data. If we assume that all of our observations sustain Gaussian distributed residuals, then we could co-add them and distinguish the planetary spectrum of WASP-4b from a nominal Rayleigh scattering atmosphere to  $4.6\sigma$ .

## 5.2.4 Clouds in WASP-4b

Because the significance of a transmission spectrum depends strongly on the atmospheric scale height [42, 46], when we increase the atmospheric metallicity (i.e. the mean molecular weight) the scale height, and thus the significance of the transmission detection, decrease respectively. [19] showed that the featureless transmission spectrum for the exo-Neptune GJ 436b could be explained by a very large atmospheric metallicity – a high mean molecular weight – ( $\sim 1000\times$  Solar) given a bulk density of this exo-Neptune,  $\rho_{\text{GJ436b}}$ , as large as  $3.53 \text{ g/cm}^3$  and assuming  $3\sigma$  uncertainty boundaries [145]. We measured the bulk density of WASP-4b,  $\rho_{\text{WASP-4b}}$ , at  $\sim 0.565 \text{ g/cm}^3$ , which is  $\sim 6\times$  less dense than GJ 436b and similar in density to Saturn, a world known to be hydrogen dominated (i.e.  $\rho_{\text{Saturn}} \sim 0.687 \text{ g/cm}^3$ ). With currently known internal structure models, it is unlikely for the mean molecular weight to be large enough to explain the featureless transmission spectrum of WASP-4b [18, 19, 22].

Hazes increase the optical depth at high altitudes by scattering the light away from our detectors [3, 40, 146–148]. This introduces a large, quasi-linear slope in the transmission spectrum towards small wavelengths. We see Rayleigh scattering in the transmission spectra of both WASP-6b and HD 189733b (see Figure 5.3). With our IMACS transmission spectrum of WASP-4b, we can rule out a nominal Rayleigh scattering model – spanning 5 scale heights over our wavelength range – by  $1.8\sigma$ . We will co-add our other 2 transits to test whether that significance will increase.

Clouds suppress absorption features in a transmission spectrum by increasing

the optical depth through the observational range. For example, with HST-WFC3, the observational regime is in the range of 1 mbar or higher for a clear atmosphere with solar abundance composition [19, 30, 33, 45]. [3] examined a detailed analysis of correlations between cloud and molecular abundance constraints for the atmospheres of hot Jupiters. They detailed the model degeneracy between a molecular detection and cloud top pressures. In the models, as we increased the cloud top pressure, the lower portion of the transmission spectrum became truncated because the clouds obscured the lower features in the water vapour absorption [9, 10]. If the cloud top pressure is above the observational regime for water vapour absorption, then the entirety of the molecular feature will be obscured [18, 36, 45].

To explain our featureless, optical transmission spectrum for WASP-4b, a nominal Rayleigh scattering model can be ruled out by almost  $2\sigma$  and it is unlikely for the mean molecular weight to be large enough to explain such a featureless transmission spectrum for a hydrogen dominated world. Therefore, high altitude clouds are the most physically amenable model to produce our featureless spectrum [17, 18, 40, 42, 147]. We conclude that it is more likely that a high altitude (low pressure) cloud layer muted the transmission spectrum by increasing the optical depth enough to obscure any molecular absorption [3, 9, 10, 18]. With our current uncertainties at short wavelengths, we can rule out the Rayleigh scattering slope to  $1.8\sigma$ . By combining our other observations of WASP-4b with IMACS, we could improve our precision up to  $\sim 5\sigma$ .

When comparing WASP-6b with WASP-4b, both hazes and clouds increase the optical depth, which inhibits the detection of molecular features; but, hazes

are expected to exhibit a negative spectral slope caused by Rayleigh scattering [40, 42, 46, 147, 148]. With respect to WASP-4b (Figure 5.3a; light blue), we can rule out nominal Rayleigh scattering by  $\sim 2\sigma$ , but not for WASP-6b (Figure 5.3b; pink); WASP-6b exhibits a significant Rayleigh scattering slope throughout the optical regime [46]. Because low pressure (high altitude) clouds are not expected to increase the transit depth towards short wavelengths [18, 19, 45], the most likely explanation for the featureless spectrum of WASP-4b is an opaque cloud layer throughout or above the observational regime [3, 17, 19, 45]. With our preliminary analysis, we can only rule out the nominal Rayleigh scattering model atmosphere – spanning 5 scale heights over our wavelength range – to  $1.8\sigma$ . It is still possible that the atmosphere of WASP-4b exhibits less significant Rayleigh scattering than HD 189733b or WASP-6b – both of which coincide with Rayleigh scattering models over  $> 4$  scale heights. By examining our other 2 observations, we should be able to improve the resulting precision on the transmission spectrum and more robustly distinguish between a Rayleigh scattering model atmosphere and an opaque cloud model atmosphere.

## 5.3 Future Work

### 5.3.1 Improving the Transmission Spectrum of WASP-4b

Our WASP-4b analysis is preliminary in several respects. I will investigate more detailed techniques and more observations to improve the precision of our measurements. To begin with, I will examine our other (UT 09-2013) spectroscopic observation of WASP-4b and our upcoming observations (UT 09-2015). The co-

addition of three IMACS transits from WASP-4b – assuming Gaussian noise limited residuals – should improve the ability to distinguish between a featureless cloud model and a sloped Rayleigh scattering model by  $\sim 60\%$ , reaching up to a significance of  $4.6\sigma$ .

In addition to increasing the number of photons observed by Magellan from the IMACS instrument, I will also examine multiple, advanced, decorrelation techniques above the first order PCA-Wavelet analysis techniques that I used in this preliminary analysis. Similarly, a detailed examination of each individual comparison star’s contribution (positive or negative) to these decorrelation techniques could improve the uncertainties derived from individual transit observations. [46] examined several different analysis techniques and derived robust statistical boundaries for the planetary spectrum of WASP-6b (see Figure 5.3). WASP-4 and WASP-6 are both  $V_{mag} \approx 12.5$  stars, therefore they share the same photon limited uncertainties. Our ability to achieve photon limited precision depends on our ability to mitigate the atmospheric, astrophysical, and instrumental noise sources. By using the same and more advanced decorrelation techniques as [46], we could minimise residual, correlated noise signals from the transmission spectrum of WASP-4b.

### 5.3.2 ACCESS Collaboration Survey

To expand the ACCESS collaboration to the northern hemisphere, I piloted an experimental, optical transmission spectroscopy observation using LRIS on Keck I (PI: Heather Knutson). We successfully completed our first observation on UT

21-09-14 and are preparing future proposals using DEIMOS and MOSFIRE, on Keck, in order to determine the most spectroscopically viable and temporally stable instrument to expand the ACCESS survey to the northern sky. Because many of the currently known exoplanets – especially the large catalog of Kepler targets – reside in the Northern sky, this pilot program could unlock the potential to spectroscopically characterize the majority of known exoplanetary atmospheres.

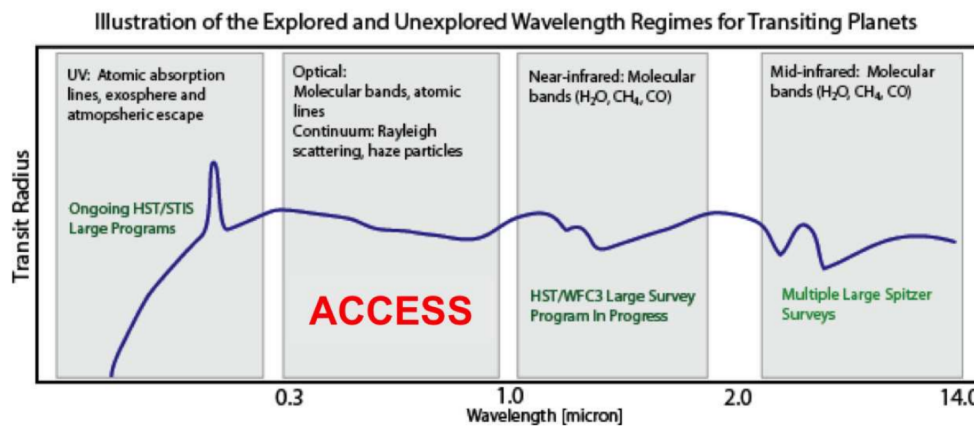


Figure 5.4: This diagram illustrates the type of information learned from transmission spectra in different spectral regimes. The blue curve represents a nominal, low-resolution transmission spectrum for a hot Jupiter with a clear, Solar composition atmosphere. The UV, near-IR, and mid-IR wavelengths are explored with the HST and Spitzer, and the optical regime – lacking a suitable and easily accessible space based spectroscopic facility – remains poorly studied. The ACCESS survey provides the first complete and uniform catalogue of transiting planetary spectra in the optical, allowing the comparison of atmospheres from hot Jupiters through Neptunes. Our survey is an excellent complement to ongoing and upcoming space based surveys at multiple wavelength ranges.

Optical spectroscopy is an important and insufficiently explored regime for characterizing exoplanetary atmospheres (see Figure 5.4). The ACCESS collabora-

tion is investigating the prevalence of Na & K atomic absorption features, as well as Rayleigh scattering, across a span of planetary masses. Benneke & Seager (2014) [10] predict that a positive detection of Rayleigh scattering and a spectral feature – at the same reference pressure – should improve constraints on the mean molecular weight and infer the boundaries on the atmospheric mass. Sing et al. (2011) [42] showed that with a plausible signal-to-noise ratio, an optical transmission spectrum can allow us to derive the planet’s temperature via the scale height. Mean molecular weight, planetary mass, and atmospheric temperature are all important metrics for interpreting the formation and evolution of exoplanets.

### 5.3.3 Planet Formation Constraints

The ACCESS collaboration has only recently begun its survey of optical spectroscopy to sample optical spectra of exoplanetary atmospheres [40, 42, 46, 148]. We have observed nearly 40 optical spectra, using IMACS, of almost 20 targets; we continue to observe new spectroscopic and photometric transits of these targets to better constrain their atmospheres. Our survey is building a statistically significant sample of optical spectra to interpret trends in exoplanetary atmospheres over a span in planetary mass. I will lead the analysis of several of our targets and piece together our representative sample of scale heights as a function of planetary mass. If we are able to discover a relationship between scale height and planetary mass, we may be able to draw a relationship between core mass and atmospheric mass, constraining the efficiency of planet formation and other physically relevant planet formation properties.

## Chapter 6: Looking Forward: Where Will We Go Next?

The exoplanet community is exploding in many directions simultaneously. We are developing new instruments for tackling problems with existing technologies [12, 55, 149, 150], while we develop techniques to improve the use of current instruments [30, 32, 33, 64]. We are expanding our understanding of planetary atmospheres [3, 17, 18] and planet formation physics [72, 73, 151–153]. At the same time, we are uncovering new theoretical regimes for planetary atmospheres to exist [3, 18, 19, 30, 45, 111, 136, 154].

With the side-by-side advances in both observational and theoretical understanding of planet formation and planetary atmospheres, we can begin to develop statistics and interpret trends in the population of known planets [3, 73, 136]. Specifically, the Kepler mission [55, 56, 71–73, 123] discovered over 4000 planetary candidates and 1000 confirmed planets – more than doubling the population of known planets in the universe. This population of exoplanets revealed that the majority of exoplanets are “small” planets ( $\sim 80\%$ ), with  $R < 4R_{\oplus}$  [6, 123]. This implies that small planets form more efficiently than large planets. Dressing et al. 2013 [72] further examined the small stars (M-dwarfs) with  $M_s < 0.5M_{\odot}$ . Their investigation derived an occurrence rate of  $\sim 90\%$  of M-dwarf’s host at least one exoplanet.

It is technologically less difficult to investigate small planets orbiting small, quiet stars [155]. As a result, with the derived population of small planets orbiting small stars, many upcoming detection and characterization surveys are examining this population by focusing our instruments on M-dwarf stars, such as EPIC and TESS [12, 156]. The Kepler mission closely studied 2543 M-dwarfs and discovered 156 planets orbiting them, which is well within the predicted detectability thresholds for M-dwarfs – implying that most M-dwarfs host planets [72].

In the coming years, several large missions to discover and characterize transiting and directly imaged planets should reveal a plethora of new planets to investigate [12, 149, 150, 157]. The Gemini Planet Imager (GPI; [149]) and Spectro Polarimetric High-contrast Exoplanet REsearch (SPHERE; [150]) instruments are currently operating on the Gemini-S and VLT 8-meter telescopes, respectively. They are searching for the faint signal of light coming directly from giant exoplanets. These directly imaged exoplanets provide a glimpse at the earliest stages of planets formation, from planet forming disks to young giant planets. GPI and SPHERE provide a rich quality of data to investigate the unique planetary conditions from these young systems by simultaneously imaging at multiple wavelengths via their IFU systems [149, 150]. SPHERE can also investigate the polarization of the light coming from the young planets and planetary systems to study their scattering and molecular properties [150]. An IFU captures a low resolution spectrum ( $R \approx 50$ ) at every pixel in the image, providing spectroscopy and photometry at the same time. This complex technique can both discover and characterize young giant planets in a single observation [149].

The Transiting Exoplanet Survey Satellite (TESS) is scheduled to be launched in 2017, providing an all sky search for transiting exoplanets that orbit their host stars with a period  $< 40$  days. The Kepler mission found 1000s of planetary candidates within 40 day orbits of their host stars [6, 71]. In the case of M-dwarfs, even the furthest reaches of a reasonable habitable zone are expected to be within the 40 day orbits of stars that have a  $M_s \sim 0.2M_\odot$ . The TESS mission is targeting all stars that are bright in the NIR; these stars are therefore either massive and far away, or small and nearby. Because M-dwarfs account for 93% of all nearby stars in the galaxy [72], the TESS mission expects to discover 1000s of small planets orbiting nearby M-dwarfs [12] that can be investigated as prevalently as the well-known GJ 1214b [17, 25, 28, 36–38, 45, 77, 158]. M-dwarfs provide the greatest contrast for both detection and characterization of small planets in the nearby galaxy [12].

The PLANetary Transits and Oscillation of stars mission (PLATO) is scheduled to launch by 2024 to search for planets in 1100 deg<sup>2</sup> of the night sky, closely examining 1 million stars! The Kepler space mission discovered over 4000 planetary candidates in a sample of 150k stars over 115 deg<sup>2</sup>. The PLATO mission will be examining 10 times that number [157] of stars and fields. The number of planets that are about to be discovered could be orders of magnitude greater than our currently known population. This is made more important because the ability to interpret planet formation physics improves significantly with the the number of planets [60, 68]. We may be able to answer decades old questions about planet formation theory in the next 10 years.

In addition to discovering 10s of 1000s of planets in the next decade, many

teams are also using the high precision photometry provided by space-based discovery missions (i.e. Kepler, EPIC, TESS, and PLATO) to make great strides in understanding stellar physics and age estimates as well [159, 160]. By investigating stellar oscillations and pulsations – called asteroseismology –, we can place constraints on stellar activity, age, internal structure, equations of state, and modes of variability [159, 160]. Decades old questions in stellar structure and evolution are being re-examined with exoplanet discovery observations. Advances in both data analysis and theoretical interpretations allowed several teams to add orders of magnitude precision estimates on stellar age estimates and internal structure models [159]; both of which are key properties in interpreting exoplanet results, as well as understanding planet formation processes and stellar physics [159, 160]. The TESS and PLATO missions promise to provide 100s of 1000s more stars to finely investigate asteroseismology.

Dynamicists investigate the long term evolution of gravitational interactions and stability of planetary systems [161, 162]. These specialists were able to use the Kepler observations for investigating planet formation physics [163], characterizing individual planetary properties [162], and placing constraints on the existent of even more, non-transiting exoplanets [161]. The high precision photometry and long time span observations taken by the Kepler space mission transformed the historically theoretical field of planetary dynamics into the observational realm of discovery and characterization [161, 162].

The apex of 10s of 1000s of new exoplanets is the pristine ability to characterize their atmospheric physics using the next generation of space telescopes. The James

Webb Space Telescope (JWST) is on schedule to be launched in October 2018 [164]. One of the four primary missions of JWST is to “study the atmospheres of exoplanets and search for the building blocks of life elsewhere in the universe” [164]. JWST has four primary instruments: NIRCam, NIRSpec, NIRISS, and MIRI [165–171]. Each of these powerful instruments specializes in a specific wavelength range and sensitivity that can be tuned to investigate the atmospheres of both transiting and directly imaged exoplanets [164]. Although it is not expected that we will be able to directly investigate the atmosphere of a habitable Earth orbiting a Sun-like star, the upcoming instrumentation provided by the JWST should be able to closely examine the planetary conditions on habitable Super-Earths orbiting nearby M-dwarfs [172].

In the last decade, we discovered completely new frontiers in understanding planet formation [6, 73, 123, 152] and re-invented our understanding of planetary atmospheres [3, 17–19, 30, 45]. Most of which was achieved with instrumentation that was not designed for exoplanet research, but adapted through evolving analysis techniques and observational modes [30, 32, 33, 36, 44, 54, 62, 63, 130]. The next generation of telescopes, instruments, and missions are being specifically designed and calibrated for exoplanet research [12, 157, 171]. We will likely be able to answer many long standing questions in planet formation theory, as well as whether other habitable worlds exist in the universe. The more interesting prospect is what new questions will be asked next.

## Bibliography

- [1] J. B. Pollack, O. Hubickyj, P. Bodenheimer, J. J. Lissauer, M. Podolak, and Y. Greenzweig. Formation of the Giant Planets by Concurrent Accretion of Solids and Gas. *Icarus*, 124:62–85, November 1996.
- [2] N. Madhusudhan, J. Harrington, K. B. Stevenson, S. Nymeyer, C. J. Campo, P. J. Wheatley, D. Deming, J. Blečić, R. A. Hardy, N. B. Lust, D. R. Anderson, A. Collier-Cameron, C. B. T. Britt, W. C. Bowman, L. Hebb, C. Hellier, P. F. L. Maxted, D. Pollacco, and R. G. West. A high C/O ratio and weak thermal inversion in the atmosphere of exoplanet WASP-12b. *Nature*, 469:64–67, January 2011.
- [3] B. Benneke. Strict Upper Limits on the Carbon-to-Oxygen Ratios of Eight Hot Jupiters from Self-Consistent Atmospheric Retrieval. *ArXiv e-prints*, April 2015.
- [4] P. Bodenheimer and D. N. C. Lin. Implications of Extrasolar Planets for Understanding Planet Formation. *Annual Review of Earth and Planetary Sciences*, 30:113–148, 2002.
- [5] E. D. Lopez and J. J. Fortney. Understanding the Mass-Radius Relation for Sub-neptunes: Radius as a Proxy for Composition. *ApJ*, 792:1, September 2014.
- [6] A. W. Howard. Observed Properties of Extrasolar Planets. *Science*, 340:572–576, May 2013.
- [7] S. Seager and D. Deming. Exoplanet Atmospheres. *ARA&A*, 48:631–672, September 2010.
- [8] A. S. Burrows. Spectra as windows into exoplanet atmospheres. *Proceedings of the National Academy of Science*, 111:12601–12609, September 2014.
- [9] B. Benneke and S. Seager. Atmospheric Retrieval for Super-Earths: Uniquely Constraining the Atmospheric Composition with Transmission Spectroscopy. *ApJ*, 753:100, July 2012.

- [10] B. Benneke and S. Seager. How to Distinguish between Cloudy Mini-Neptunes and Water/Volatile-dominated Super-Earths. *ApJ*, 778:153, December 2013.
- [11] D. Charbonneau, L. E. Allen, S. T. Megeath, G. Torres, R. Alonso, T. M. Brown, R. L. Gilliland, D. W. Latham, G. Mandushev, F. T. O’Donovan, and A. Sozzetti. Detection of Thermal Emission from an Extrasolar Planet. *ApJ*, 626:523–529, June 2005.
- [12] G. R. Ricker, J. N. Winn, R. Vanderspek, D. W. Latham, G. Á. Bakos, J. L. Bean, Z. K. Berta-Thompson, T. M. Brown, L. Buchhave, N. R. Butler, R. P. Butler, W. J. Chaplin, D. Charbonneau, J. Christensen-Dalsgaard, M. Clampin, D. Deming, J. Doty, N. De Lee, C. Dressing, E. W. Dunham, M. Endl, F. Fressin, J. Ge, T. Henning, M. J. Holman, A. W. Howard, S. Ida, J. Jenkins, G. Jernigan, J. A. Johnson, L. Kaltenegger, N. Kawai, H. Kjeldsen, G. Laughlin, A. M. Levine, D. Lin, J. J. Lissauer, P. MacQueen, G. Marcy, P. R. McCullough, T. D. Morton, N. Narita, M. Paegert, E. Palle, F. Pepe, J. Pepper, A. Quirrenbach, S. A. Rinehart, D. Sasselov, B. Sato, S. Seager, A. Sozzetti, K. G. Stassun, P. Sullivan, A. Szentgyorgyi, G. Torres, S. Udry, and J. Villaseñor. Transiting Exoplanet Survey Satellite (TESS). *Journal of Astronomical Telescopes, Instruments, and Systems*, 1(1):014003, 2015.
- [13] P. W. Sullivan, J. N. Winn, Z. K. Berta-Thompson, D. Charbonneau, D. Deming, C. D. Dressing, D. W. Latham, A. M. Levine, P. R. McCullough, T. Morton, G. R. Ricker, R. Vanderspek, and D. Woods. The Transiting Exoplanet Survey Satellite: Simulations of planet detections and astrophysical false positives. *ArXiv e-prints*, June 2015.
- [14] D. Charbonneau, T. M. Brown, D. W. Latham, and M. Mayor. Detection of Planetary Transits Across a Sun-like Star. *ApJl*, 529:L45–L48, January 2000.
- [15] J. N. Winn. *Exoplanet Transits and Occultations, Exoplanets, Ed. Sara Seager*, pages 55–77. Arizona Press, December 2010.
- [16] M. R. Line, G. Vasisht, P. Chen, D. Angerhausen, and Y. L. Yung. Thermochemical and Photochemical Kinetics in Cooler Hydrogen-dominated Extrasolar Planets: A Methane-poor GJ436b? *ApJ*, 738:32, September 2011.
- [17] C. V. Morley, J. J. Fortney, E. M.-R. Kempton, M. S. Marley, C. Visscher, and K. Zahnle. Quantitatively Assessing the Role of Clouds in the Transmission Spectrum of GJ 1214b. *ApJ*, 775:33, September 2013.
- [18] J. I. Moses, M. R. Line, C. Visscher, M. R. Richardson, N. Nettelmann, J. J. Fortney, T. S. Barman, K. B. Stevenson, and N. Madhusudhan. Compositional Diversity in the Atmospheres of Hot Neptunes, with Application to GJ 436b. *ApJ*, 777:34, November 2013.

- [19] H. A. Knutson, B. Benneke, D. Deming, and D. Homeier. A featureless transmission spectrum for the Neptune-mass exoplanet GJ436b. *Nature*, 505:66–68, January 2014.
- [20] M. R. Line, H. Knutson, A. S. Wolf, and Y. L. Yung. A Systematic Retrieval Analysis of Secondary Eclipse Spectra. II. A Uniform Analysis of Nine Planets and their C to O Ratios. *ApJ*, 783:70, March 2014.
- [21] M. R. Line, J. J. Fortney, M. S. Marley, and S. Sorahana. A Data-driven Approach for Retrieving Temperatures and Abundances in Brown Dwarf Atmospheres. *ApJ*, 793:33, September 2014.
- [22] L. A. Rogers. Most 1.6 Earth-radius Planets are Not Rocky. *ApJ*, 801:41, March 2015.
- [23] P. Ingraham, M. S. Marley, D. Saumon, C. Marois, B. Macintosh, T. Barman, B. Bauman, A. Burrows, J. K. Chilcote, R. J. De Rosa, D. Dillon, R. Doyon, J. Dunn, D. Erikson, M. P. Fitzgerald, D. Gavel, S. J. Goodsell, J. R. Graham, M. Hartung, P. Hibon, P. G. Kalas, Q. Konopacky, J. A. Larkin, J. Maire, F. Marchis, J. McBride, M. Millar-Blanchaer, K. M. Morzinski, A. Norton, R. Oppenheimer, D. W. Palmer, J. Patience, M. D. Perrin, L. A. Poyneer, L. Pueyo, F. Rantakyro, N. Sadakuni, L. Saddlemyer, D. Savransky, R. Soummer, A. Sivaramakrishnan, I. Song, S. Thomas, J. K. Wallace, S. J. Wiktorowicz, and S. G. Wolff. Gemini Planet Imager Spectroscopy of the HR 8799 Planets c and d. *ApJl*, 794:L15, October 2014.
- [24] L. M. Weiss, G. W. Marcy, J. F. Rowe, A. W. Howard, H. Isaacson, J. J. Fortney, N. Miller, B.-O. Demory, D. A. Fischer, E. R. Adams, A. K. Dupree, S. B. Howell, R. Kolbl, J. A. Johnson, E. P. Horch, M. E. Everett, D. C. Fabrycky, and S. Seager. The Mass of KOI-94d and a Relation for Planet Radius, Mass, and Incident Flux. *ApJ*, 768:14, May 2013.
- [25] D. Charbonneau, Z. K. Berta, J. Irwin, C. J. Burke, P. Nutzman, L. A. Buchhave, C. Lovis, X. Bonfils, D. W. Latham, S. Udry, R. A. Murray-Clay, M. J. Holman, E. E. Falco, J. N. Winn, D. Queloz, F. Pepe, M. Mayor, X. Delfosse, and T. Forveille. A super-Earth transiting a nearby low-mass star. *Nature*, 462:891–894, December 2009.
- [26] D. Deming. Planetary science: A cloudy view of exoplanets. *Nature*, 468:636–637, December 2010.
- [27] L. A. Rogers and S. Seager. Three Possible Origins for the Gas Layer on GJ 1214b. *ApJ*, 716:1208–1216, June 2010.
- [28] J. L. Bean, E. Miller-Ricci Kempton, and D. Homeier. A ground-based transmission spectrum of the super-Earth exoplanet GJ 1214b. *Nature*, 468:669–672, December 2010.

- [29] F. Sohl, F. W. Wagner, and H. Rauer. Mass-radius relationships of rocky exoplanets. *ArXiv e-prints*, November 2012.
- [30] J. Fraine, D. Deming, B. Benneke, H. Knutson, A. Jordán, N. Espinoza, N. Madhusudhan, A. Wilkins, and K. Todorov. Water vapour absorption in the clear atmosphere of a Neptune-sized exoplanet. *Nature*, 513:526–529, September 2014.
- [31] N. Nettelmann. Predictions on the core mass of Jupiter and of giant planets in general. *Ap&SS*, 336:47–51, November 2011.
- [32] P. R. McCullough, N. Crouzet, D. Deming, and N. Madhusudhan. Water Vapor in the Spectrum of the Extrasolar Planet HD 189733b. I. The Transit. *ApJ*, 791:55, August 2014.
- [33] D. Deming, A. Wilkins, P. McCullough, A. Burrows, J. J. Fortney, E. Agol, I. Dobbs-Dixon, N. Madhusudhan, N. Crouzet, J.-M. Desert, R. L. Gilliland, K. Haynes, H. A. Knutson, M. Line, Z. Magic, A. M. Mandell, S. Ranjan, D. Charbonneau, M. Clampin, S. Seager, and A. P. Showman. Infrared Transmission Spectroscopy of the Exoplanets HD 209458b and XO-1b Using the Wide Field Camera-3 on the Hubble Space Telescope. *ApJ*, 774:95, September 2013.
- [34] D. Charbonneau, T. M. Brown, R. W. Noyes, and R. L. Gilliland. Detection of an Extrasolar Planet Atmosphere. *ApJ*, 568:377–384, March 2002.
- [35] S. Redfield, M. Endl, W. D. Cochran, and L. Koesterke. Sodium Absorption from the Exoplanetary Atmosphere of HD 189733b Detected in the Optical Transmission Spectrum. *ApJl*, 673:L87–L90, January 2008.
- [36] J. D. Fraine, D. Deming, M. Gillon, E. Jehin, B.-O. Demory, B. Benneke, S. Seager, N. K. Lewis, H. Knutson, and J.-M. Désert. Spitzer Transits of the Super-Earth GJ1214b and Implications for its Atmosphere. *ApJ*, 765:127, March 2013.
- [37] J.-M. Désert, J. Bean, E. Miller-Ricci Kempton, Z. K. Berta, D. Charbonneau, J. Irwin, J. Fortney, C. J. Burke, and P. Nutzman. Observational Evidence for a Metal-rich Atmosphere on the Super-Earth GJ1214b. *ApJl*, 731:L40, April 2011.
- [38] Z. K. Berta, D. Charbonneau, J.-M. Désert, E. Miller-Ricci Kempton, P. R. McCullough, C. J. Burke, J. J. Fortney, J. Irwin, P. Nutzman, and D. Homeier. The Flat Transmission Spectrum of the Super-Earth GJ1214b from Wide Field Camera 3 on the Hubble Space Telescope. *ApJ*, 747:35, March 2012.
- [39] R. Hu and S. Seager. Photochemistry in Terrestrial Exoplanet Atmospheres. III. Photochemistry and Thermochemistry in Thick Atmospheres on Super Earths and Mini Neptunes. *ApJ*, 784:63, March 2014.

- [40] F. Pont, D. K. Sing, N. P. Gibson, S. Aigrain, G. Henry, and N. Husnoo. The prevalence of dust on the exoplanet HD 189733b from Hubble and Spitzer observations. *MNRAS*, 432:2917–2944, July 2013.
- [41] A. S. Ackerman and M. S. Marley. Precipitating Condensation Clouds in Substellar Atmospheres. *ApJ*, 556:872–884, August 2001.
- [42] D. K. Sing, F. Pont, S. Aigrain, D. Charbonneau, J.-M. Désert, N. Gibson, R. Gilliland, W. Hayek, G. Henry, H. Knutson, A. Lecavelier Des Etangs, T. Mazeh, and A. Shporer. Hubble Space Telescope transmission spectroscopy of the exoplanet HD 189733b: high-altitude atmospheric haze in the optical and near-ultraviolet with STIS. *MNRAS*, 416:1443–1455, September 2011.
- [43] J. Moses. Extrasolar planets: Cloudy with a chance of dustballs. *Nature*, 505:31–32, January 2014.
- [44] K. B. Stevenson, J. Harrington, S. Nymeyer, N. Madhusudhan, S. Seager, W. C. Bowman, R. A. Hardy, D. Deming, E. Rauscher, and N. B. Lust. Possible thermochemical disequilibrium in the atmosphere of the exoplanet GJ 436b. *Nature*, 464:1161–1164, April 2010.
- [45] L. Kreidberg, J. L. Bean, J.-M. Désert, B. Benneke, D. Deming, K. B. Stevenson, S. Seager, Z. Berta-Thompson, A. Seifahrt, and D. Homeier. Clouds in the atmosphere of the super-Earth exoplanet GJ1214b. *Nature*, 505:69–72, January 2014.
- [46] A. Jordán, N. Espinoza, M. Rabus, S. Eyheramendy, D. K. Sing, J.-M. Désert, G. Á. Bakos, J. J. Fortney, M. López-Morales, P. F. L. Maxted, A. H. M. J. Triaud, and A. Szentgyorgyi. A Ground-based Optical Transmission Spectrum of WASP-6b. *ApJ*, 778:184, December 2013.
- [47] V. Parmentier, A. P. Showman, and Y. Lian. 3D mixing in hot Jupiters atmospheres. I. Application to the day/night cold trap in HD 209458b. *A&A*, 558:A91, October 2013.
- [48] H. A. Knutson, D. Dragomir, L. Kreidberg, E. M.-R. Kempton, P. R. McCullough, J. J. Fortney, J. L. Bean, M. Gillon, D. Homeier, and A. W. Howard. Hubble Space Telescope Near-IR Transmission Spectroscopy of the Super-Earth HD 97658b. *ApJ*, 794:155, October 2014.
- [49] H. R. Wakeford and D. K. Sing. Transmission spectral properties of clouds for hot Jupiter exoplanets. *A&A*, 573:A122, January 2015.
- [50] C. V. Morley, M. S. Marley, J. J. Fortney, R. Lupu, D. Saumon, T. Greene, and K. Lodders. Water Clouds in Y Dwarfs and Exoplanets. *ApJ*, 787:78, May 2014.

- [51] J. J. Fortney, M. S. Marley, and J. W. Barnes. Planetary Radii across Five Orders of Magnitude in Mass and Stellar Insolation: Application to Transits. *ApJ*, 659:1661–1672, April 2007.
- [52] J. J. Fortney, C. Mordasini, N. Nettelmann, E. M.-R. Kempton, T. P. Greene, and K. Zahnle. A Framework for Characterizing the Atmospheres of Low-mass Low-density Transiting Planets. *ApJ*, 775:80, September 2013.
- [53] M. Mayor and D. Queloz. A Jupiter-mass companion to a solar-type star. *Nature*, 378:355–359, November 1995.
- [54] D. Deming, S. Seager, L. J. Richardson, and J. Harrington. Infrared radiation from an extrasolar planet. *Nature*, 434:740–743, March 2005.
- [55] W. J. Borucki, D. Koch, G. Basri, N. Batalha, T. Brown, D. Caldwell, J. Caldwell, J. Christensen-Dalsgaard, W. D. Cochran, E. DeVore, E. W. Dunham, A. K. Dupree, T. N. Gautier, J. C. Geary, R. Gilliland, A. Gould, S. B. Howell, J. M. Jenkins, Y. Kondo, D. W. Latham, G. W. Marcy, S. Meibom, H. Kjeldsen, J. J. Lissauer, D. G. Monet, D. Morrison, D. Sasselov, J. Tarter, A. Boss, D. Brownlee, T. Owen, D. Buzasi, D. Charbonneau, L. Doyle, J. Fortney, E. B. Ford, M. J. Holman, S. Seager, J. H. Steffen, W. F. Welsh, J. Rowe, H. Anderson, L. Buchhave, D. Ciardi, L. Walkowicz, W. Sherry, E. Horch, H. Isaacson, M. E. Everett, D. Fischer, G. Torres, J. A. Johnson, M. Endl, P. MacQueen, S. T. Bryson, J. Dotson, M. Haas, J. Kolodziejczak, J. Van Cleve, H. Chandrasekaran, J. D. Twicken, E. V. Quintana, B. D. Clarke, C. Allen, J. Li, H. Wu, P. Tenenbaum, E. Verner, F. Bruhweiler, J. Barnes, and A. Prsa. Kepler Planet-Detection Mission: Introduction and First Results. *Science*, 327:977–, February 2010.
- [56] D. G. Koch, W. J. Borucki, G. Basri, N. M. Batalha, T. M. Brown, D. Caldwell, J. Christensen-Dalsgaard, W. D. Cochran, E. DeVore, E. W. Dunham, T. N. Gautier, III, J. C. Geary, R. L. Gilliland, A. Gould, J. Jenkins, Y. Kondo, D. W. Latham, J. J. Lissauer, G. Marcy, D. Monet, D. Sasselov, A. Boss, D. Brownlee, J. Caldwell, A. K. Dupree, S. B. Howell, H. Kjeldsen, S. Meibom, D. Morrison, T. Owen, H. Reitsema, J. Tarter, S. T. Bryson, J. L. Dotson, P. Gazis, M. R. Haas, J. Kolodziejczak, J. F. Rowe, J. E. Van Cleve, C. Allen, H. Chandrasekaran, B. D. Clarke, J. Li, E. V. Quintana, P. Tenenbaum, J. D. Twicken, and H. Wu. Kepler Mission Design, Realized Photometric Performance, and Early Science. *ApJl*, 713:L79–L86, April 2010.
- [57] M. R. Line and Y. L. Yung. A Systematic Retrieval Analysis of Secondary Eclipse Spectra. III. Diagnosing Chemical Disequilibrium in Planetary Atmospheres. *ApJ*, 779:3, December 2013.
- [58] H. A. Knutson, D. Charbonneau, L. E. Allen, A. Burrows, and S. T. Megeath. The 3.6-8.0  $\mu\text{m}$  Broadband Emission Spectrum of HD 209458b: Evidence for an Atmospheric Temperature Inversion. *ApJ*, 673:526–531, January 2008.

- [59] N. P. Gibson, S. Aigrain, S. Roberts, T. M. Evans, M. Osborne, and F. Pont. A Gaussian process framework for modelling instrumental systematics: application to transmission spectroscopy. *MNRAS*, 419:2683–2694, January 2012.
- [60] D. Foreman-Mackey, D. W. Hogg, and T. D. Morton. Exoplanet Population Inference and the Abundance of Earth Analogs from Noisy, Incomplete Catalogs. *ApJ*, 795:64, November 2014.
- [61] D. Deming, P. V. Sada, B. Jackson, S. W. Peterson, E. Agol, H. A. Knutson, D. E. Jennings, F. Haase, and K. Bays. Kepler and Ground-based Transits of the Exo-Neptune HAT-P-11b. *ApJ*, 740:33, October 2011.
- [62] S. Ballard, D. Charbonneau, D. Deming, H. A. Knutson, J. L. Christiansen, M. J. Holman, D. Fabrycky, S. Seager, and M. F. A’Hearn. A Search for a Sub-Earth-Sized Companion to GJ 436 and a Novel Method to Calibrate Warm Spitzer IRAC Observations. *PASP*, 122:1341–1352, November 2010.
- [63] N. K. Lewis, H. A. Knutson, A. P. Showman, N. B. Cowan, G. Laughlin, A. Burrows, D. Deming, J. R. Crepp, K. J. Mighell, E. Agol, G. Á. Bakos, D. Charbonneau, J.-M. Désert, D. A. Fischer, J. J. Fortney, J. D. Hartman, S. Hinkley, A. W. Howard, J. A. Johnson, M. Kao, J. Langton, and G. W. Marcy. Orbital Phase Variations of the Eccentric Giant Planet HAT-P-2b. *ApJ*, 766:95, April 2013.
- [64] D. Deming, H. Knutson, J. Kammer, B. J. Fulton, J. Ingalls, S. Carey, A. Burrows, J. J. Fortney, K. Todorov, E. Agol, N. Cowan, J.-M. Desert, J. Fraine, J. Langton, C. Morley, and A. P. Showman. Spitzer Secondary Eclipses of the Dense, Modestly-irradiated, Giant Exoplanet HAT-P-20b Using Pixel-level Decorrelation. *ApJ*, 805:132, June 2015.
- [65] A. N. Wilkins, D. Deming, N. Madhusudhan, A. Burrows, H. Knutson, P. McCullough, and S. Ranjan. The Emergent 1.1-1.7  $\mu\text{m}$  Spectrum of the Exoplanet CoRoT-2b as Measured Using the Hubble Space Telescope. *ApJ*, 783:113, March 2014.
- [66] E. B. Ford. Quantifying the Uncertainty in the Orbits of Extrasolar Planets. *AJ*, 129:1706–1717, March 2005.
- [67] E. B. Ford. Improving the Efficiency of Markov Chain Monte Carlo for Analyzing the Orbits of Extrasolar Planets. *ApJ*, 642:505–522, May 2006.
- [68] D. Foreman-Mackey, D. W. Hogg, D. Lang, and J. Goodman. emcee: The MCMC Hammer. *PASP*, 125:306–312, March 2013.
- [69] J.E. Van Celve and D.A. Caldwell. Kepler Instrument Handbook. Technical report, NASA Ames Research Center, 2009.
- [70] A. R. Howe and A. S. Burrows. Theoretical Transit Spectra for GJ 1214b and Other ”Super-Earths”. *ApJ*, 756:176, September 2012.

- [71] E. A. Petigura, A. W. Howard, and G. W. Marcy. Prevalence of Earth-size planets orbiting Sun-like stars. *Proceedings of the National Academy of Science*, 110:19273–19278, November 2013.
- [72] C. D. Dressing and D. Charbonneau. The Occurrence Rate of Small Planets around Small Stars. *ApJ*, 767:95, April 2013.
- [73] J.-M. Désert, D. Charbonneau, G. Torres, F. Fressin, S. Ballard, S. T. Bryson, H. A. Knutson, N. M. Batalha, W. J. Borucki, T. M. Brown, D. Deming, E. B. Ford, J. J. Fortney, R. L. Gilliland, D. W. Latham, and S. Seager. Low False Positive Rate of Kepler Candidates Estimated From A Combination Of Spitzer And Follow-Up Observations. *ApJ*, 804:59, May 2015.
- [74] S. Seager and D. D. Sasselov. Theoretical Transmission Spectra during Extrasolar Giant Planet Transits. *ApJ*, 537:916–921, July 2000.
- [75] A. M. Mandell, K. Haynes, E. Sinukoff, N. Madhusudhan, A. Burrows, and D. Deming. Exoplanet Transit Spectroscopy Using WFC3: WASP-12 b, WASP-17 b, and WASP-19 b. *ApJ*, 779:128, December 2013.
- [76] E. Miller-Ricci, S. Seager, and D. Sasselov. The Atmospheric Signatures of Super-Earths: How to Distinguish Between Hydrogen-Rich and Hydrogen-Poor Atmospheres. *ApJ*, 690:1056–1067, January 2009.
- [77] J. L. Bean, J.-M. Désert, P. Kabath, B. Stalder, S. Seager, E. Miller-Ricci Kempton, Z. K. Berta, D. Homeier, S. Walsh, and A. Seifahrt. The Optical and Near-infrared Transmission Spectrum of the Super-Earth GJ 1214b: Further Evidence for a Metal-rich Atmosphere. *ApJ*, 743:92, December 2011.
- [78] I. J. M. Crossfield, T. Barman, and B. M. S. Hansen. High-resolution, Differential, Near-infrared Transmission Spectroscopy of GJ 1214b. *ApJ*, 736:132, August 2011.
- [79] Z. K. Berta, D. Charbonneau, J. Bean, J. Irwin, C. J. Burke, J.-M. Désert, P. Nutzman, and E. E. Falco. The GJ1214 Super-Earth System: Stellar Variability, New Transits, and a Search for Additional Planets. *ApJ*, 736:12, July 2011.
- [80] E. J. W. de Mooij, M. Brogi, R. J. de Kok, J. Koppenhoefer, S. V. Nefs, I. A. G. Snellen, J. Greiner, J. Hanse, R. C. Heinsbroek, C. H. Lee, and P. P. van der Werf. Optical to near-infrared transit observations of super-Earth GJ 1214b: water-world or mini-Neptune? *A&A*, 538:A46, February 2012.
- [81] B. Croll, L. Albert, R. Jayawardhana, E. Miller-Ricci Kempton, J. J. Fortney, N. Murray, and H. Neilson. Broadband Transmission Spectroscopy of the Super-Earth GJ 1214b Suggests a Low Mean Molecular Weight Atmosphere. *ApJ*, 736:78, August 2011.

- [82] M. Gillon, A. H. M. J. Triaud, J. J. Fortney, B.-O. Demory, E. Jehin, M. Lendl, P. Magain, P. Kabath, D. Queloz, R. Alonso, D. R. Anderson, A. Collier Cameron, A. Fumel, L. Hebb, C. Hellier, A. Lanotte, P. F. L. Maxted, N. Mowlavi, and B. Smalley. The TRAPPIST survey of southern transiting planets. I. Thirty eclipses of the ultra-short period planet WASP-43 b. *A&A*, 542:A4, June 2012.
- [83] M. Gillon, E. Jehin, P. Magain, V. Chantry, D. Hutsemékers, J. Manfroid, D. Queloz, and S. Udry. TRAPPIST: a robotic telescope dedicated to the study of planetary systems. In *European Physical Journal Web of Conferences*, volume 11 of *European Physical Journal Web of Conferences*, page 6002, February 2011.
- [84] E. Jehin, M. Gillon, D. Queloz, P. Magain, J. Manfroid, V. Chantry, M. Lendl, D. Hutsemékers, and S. Udry. TRAPPIST: TRANSiting Planets and Planetes-Imals Small Telescope. *The Messenger*, 145:2–6, September 2011.
- [85] E. Agol, N. B. Cowan, H. A. Knutson, D. Deming, J. H. Steffen, G. W. Henry, and D. Charbonneau. The Climate of HD 189733b from Fourteen Transits and Eclipses Measured by Spitzer. *ApJ*, 721:1861–1877, October 2010.
- [86] H. A. Knutson, N. Lewis, J. J. Fortney, A. Burrows, A. P. Showman, N. B. Cowan, E. Agol, S. Aigrain, D. Charbonneau, D. Deming, J.-M. Désert, G. W. Henry, J. Langton, and G. Laughlin. 3.6 and 4.5  $\mu\text{m}$  Phase Curves and Evidence for Non-equilibrium Chemistry in the Atmosphere of Extrasolar Planet HD 189733b. *ApJ*, 754:22, July 2012.
- [87] K. J. Mighell. Stellar photometry and astrometry with discrete point spread functions. *MNRAS*, 361:861–878, August 2005.
- [88] K. Mandel and E. Agol. Analytic Light Curves for Planetary Transit Searches. *ApJl*, 580:L171–L175, December 2002.
- [89] A. R. Liddle. Information criteria for astrophysical model selection. *MNRAS*, 377:L74–L78, May 2007.
- [90] A. Claret and S. Bloemen. Gravity and limb-darkening coefficients for the Kepler, CoRoT, Spitzer, uvby, UBVRIJHK, and Sloan photometric systems. *A&A*, 529:A75, May 2011.
- [91] J.-M. Désert, D. Sing, A. Vidal-Madjar, G. Hébrard, D. Ehrenreich, A. Lecavelier Des Etangs, V. Parmentier, R. Ferlet, and G. W. Henry. Transit spectrophotometry of the exoplanet HD 189733b. II. New Spitzer observations at 3.6  $\mu\text{m}$ . *A&A*, 526:A12, February 2011.
- [92] P. Nutzman and D. Charbonneau. Design Considerations for a Ground-Based Transit Search for Habitable Planets Orbiting M Dwarfs. *PASP*, 120:317–327, March 2008.

- [93] F. Allard and P. H. Hauschildt. Model atmospheres for M (sub)dwarf stars. 1: The base model grid. *ApJ*, 445:433–450, May 1995.
- [94] J. B. Rice and K. G. Strassmeier. Doppler imaging of stellar surface structure. VII. The very young, single K2-dwarf LQ Hydrae. *A&A*, 336:972–979, August 1998.
- [95] P. V. Sada, D. Deming, B. Jackson, D. E. Jennings, S. W. Peterson, F. Haase, K. Bays, E. O’Gorman, and A. Lundsford. Recent Transits of the Super-Earth Exoplanet GJ 1214b. *ApJl*, 720:L215–L218, September 2010.
- [96] J. A. Carter, J. N. Winn, M. J. Holman, D. Fabrycky, Z. K. Berta, C. J. Burke, and P. Nutzman. The Transit Light Curve Project. XIII. Sixteen Transits of the Super-Earth GJ 1214b. *ApJ*, 730:82, April 2011.
- [97] P. Kundurthy, E. Agol, A. C. Becker, R. Barnes, B. Williams, and A. Mukadam. APOSTLE Observations of GJ 1214b: System Parameters and Evidence for Stellar Activity. *ApJ*, 731:123, April 2011.
- [98] F. Murgas, E. Pallé, A. Cabrera-Lavers, K. D. Colón, E. L. Martín, and H. Parviainen. Narrow band H $\alpha$  photometry of the super-Earth GJ 1214b with GTC/OSIRIS tunable filters. *A&A*, 544:A41, August 2012.
- [99] N. Narita, Y. H. Takahashi, M. Kuzuhara, T. Hirano, T. Suenaga, R. Kandori, T. Kudo, B. Sato, R. Suzuki, S. Ida, M. Nagasawa, L. Abe, W. Brandner, T. D. Brandt, J. Carson, S. E. Egner, M. Feldt, M. Goto, C. A. Grady, O. Guyon, J. Hashimoto, Y. Hayano, M. Hayashi, S. S. Hayashi, T. Henning, K. W. Hodapp, M. Ishii, M. Iye, M. Janson, G. R. Knapp, N. Kusakabe, J. Kwon, T. Matsuo, S. Mayama, M. W. McElwain, S. M. Miyama, J.-I. Morino, A. Moro-Martin, T. Nishimura, T.-S. Pyo, E. Serabyn, H. Suto, M. Takami, N. Takato, H. Terada, C. Thalmann, D. Tomono, E. L. Turner, M. Watanabe, J. P. Wisniewski, T. Yamada, H. Takami, T. Usuda, and M. Tamura. A Common Proper Motion Stellar Companion to HAT-P-7. *PASJ*, 64:L7, December 2012.
- [100] D. Ehrenreich, X. Bonfils, C. Lovis, X. Delfosse, T. Forveille, M. Mayor, V. Neves, N. C. Santos, S. Udry, and D. Ségransan. Near-infrared transmission spectrum of the warm-Uranus GJ 3470b with the Wide Field Camera-3 on the Hubble Space Telescope. *A&A*, 570:A89, October 2014.
- [101] G. D’Angelo, R. H. Durisen, and J. J. Lissauer. *Giant Planet Formation, Exoplanets, Ed. Sara Seager*, pages 319–346. Arizona Press, December 2010.
- [102] G. Á. Bakos, G. Torres, A. Pál, J. Hartman, G. Kovács, R. W. Noyes, D. W. Latham, D. D. Sasselov, B. Sipőcz, G. A. Esquerdo, D. A. Fischer, J. A. Johnson, G. W. Marcy, R. P. Butler, H. Isaacson, A. Howard, S. Vogt, G. Kovács,

- J. Fernandez, A. Moór, R. P. Stefanik, J. Lázár, I. Papp, and P. Sári. HAT-P-11b: A Super-Neptune Planet Transiting a Bright K Star in the Kepler Field. *ApJ*, 710:1724–1745, February 2010.
- [103] G. G. Fazio, J. L. Hora, L. E. Allen, M. L. N. Ashby, P. Barmby, L. K. Deutsch, J.-S. Huang, S. Kleiner, M. Marengo, S. T. Megeath, G. J. Melnick, M. A. Pahre, B. M. Patten, J. Polizotti, H. A. Smith, R. S. Taylor, Z. Wang, S. P. Willner, W. F. Hoffmann, J. L. Pipher, W. J. Forrest, C. W. McMurty, C. R. McCreight, M. E. McKelvey, R. E. McMurray, D. G. Koch, S. H. Moseley, R. G. Arendt, J. E. Mentzell, C. T. Marx, P. Losch, P. Mayman, W. Eichhorn, D. Krebs, M. Jhabvala, D. Y. Gezari, D. J. Fixsen, J. Flores, K. Shakoorzadeh, R. Jungo, C. Hakun, L. Workman, G. Karpati, R. Kichak, R. Whitley, S. Mann, E. V. Tollestrup, P. Eisenhardt, D. Stern, V. Gorjian, B. Bhattacharya, S. Carey, B. O. Nelson, W. J. Glaccum, M. Lacy, P. J. Lowrance, S. Laine, W. T. Reach, J. A. Stauffer, J. A. Surace, G. Wilson, E. L. Wright, A. Hoffman, G. Domingo, and M. Cohen. The Infrared Array Camera (IRAC) for the Spitzer Space Telescope. *ApJs*, 154:10–17, September 2004.
- [104] T.-O. Husser, S. Wende-von Berg, S. Dreizler, D. Homeier, A. Reiners, T. Barman, and P. H. Hauschildt. A new extensive library of PHOENIX stellar atmospheres and synthetic spectra. *A&A*, 553:A6, May 2013.
- [105] P. F. Bernath. Water in sunspots and stars. *Highlights of Astronomy*, 12:70–72, 2002.
- [106] H. A. Knutson, A. W. Howard, and H. Isaacson. A Correlation Between Stellar Activity and Hot Jupiter Emission Spectra. *ApJ*, 720:1569–1576, September 2010.
- [107] R. Sanchis-Ojeda and J. N. Winn. Starspots, Spin-Orbit Misalignment, and Active Latitudes in the HAT-P-11 Exoplanetary System. *ApJ*, 743:61, December 2011.
- [108] P. McCullough and J. MacKenty. Considerations for using Spatial Scans with WFC3. Technical report, Space Telescope Science Institute, May 2012.
- [109] N. Espinoza and A. Jordán. Limb darkening and exoplanets: testing stellar model atmospheres and identifying biases in transit parameters. *MNRAS*, 450:1879–1899, June 2015.
- [110] J. Eastman, R. Siverd, and B. S. Gaudi. Achieving Better Than 1 Minute Accuracy in the Heliocentric and Barycentric Julian Dates. *PASP*, 122:935–946, August 2010.
- [111] H. A. Knutson, B. J. Fulton, B. T. Montet, M. Kao, H. Ngo, A. W. Howard, J. R. Crepp, S. Hinkley, G. Á. Bakos, K. Batygin, J. A. Johnson, T. D. Morton, and P. S. Muirhead. Friends of Hot Jupiters. I. A Radial Velocity

- Search for Massive, Long-period Companions to Close-in Gas Giant Planets. *ApJ*, 785:126, April 2014.
- [112] A. Claret. A new non-linear limb-darkening law for LTE stellar atmosphere models. Calculations for  $-5.0 \leq \log[M/H] \leq +1$ ,  $2000 \text{ K} \leq T_{eff} \leq 50000 \text{ K}$  at several surface gravities. *A&A*, 363:1081–1190, November 2000.
- [113] F. Castelli and R. L. Kurucz. New Grids of ATLAS9 Model Atmospheres. *ArXiv Astrophysics e-prints*, May 2004.
- [114] Travis E. Oliphant. Python for scientific computing. *Computing in Science and Engineering*, 9(3):10–20, 2007.
- [115] A. Rajan and et al. *WFC3 Data Handbook v. 2.1*. Space Telescope Science Institute, May 2011.
- [116] Robert E. Kass and Adrian E. Raftery. Bayes factors. *Journal of the American Statistical Association*, 90(430):pp. 773–795, 1995.
- [117] J. A. Carter and J. N. Winn. Parameter Estimation from Time-series Data with Correlated Errors: A Wavelet-based Method and its Application to Transit Light Curves. *ApJ*, 704:51–67, October 2009.
- [118] Anand Patil, David Huard, and Christopher J. Fonnesbeck. Pymc: Bayesian stochastic modelling in python. *Journal of Statistical Software*, 35(4):1–81, 7 2010.
- [119] K. O. Todorov, D. Deming, H. A. Knutson, A. Burrows, P. V. Sada, N. B. Cowan, E. Agol, J.-M. Desert, J. J. Fortney, D. Charbonneau, G. Laughlin, J. Langton, A. P. Showman, and N. K. Lewis. Warm Spitzer Observations of Three Hot Exoplanets: XO-4b, HAT-P-6b, and HAT-P-8b. *ApJ*, 746:111, February 2012.
- [120] N. Madhusudhan. C/O Ratio as a Dimension for Characterizing Exoplanetary Atmospheres. *ApJ*, 758:36, October 2012.
- [121] L. A. Rogers and S. Seager. A Framework for Quantifying the Degeneracies of Exoplanet Interior Compositions. *ApJ*, 712:974–991, April 2010.
- [122] E. Chiang and G. Laughlin. The minimum-mass extrasolar nebula: in situ formation of close-in super-Earths. *MNRAS*, 431:3444–3455, June 2013.
- [123] F. Fressin, G. Torres, D. Charbonneau, S. T. Bryson, J. Christiansen, C. D. Dressing, J. M. Jenkins, L. M. Walkowicz, and N. M. Batalha. The False Positive Rate of Kepler and the Occurrence of Planets. *ApJ*, 766:81, April 2013.

- [124] S. Carey, J. Ingalls, J. Hora, J. Surace, W. Glaccum, P. Lowrance, J. Krick, D. Cole, S. Laine, C. Engelke, S. Price, R. Bohlin, and K. Gordon. Absolute photometric calibration of IRAC: lessons learned using nine years of flight data. In *Society of Photo-Optical Instrumentation Engineers (SPIE) Conference Series*, volume 8442 of *Society of Photo-Optical Instrumentation Engineers (SPIE) Conference Series*, page 1, September 2012.
- [125] S. Ballard, W. J. Chaplin, D. Charbonneau, J.-M. Désert, F. Fressin, L. Zeng, M. W. Werner, G. R. Davies, V. Silva Aguirre, S. Basu, J. Christensen-Dalsgaard, T. S. Metcalfe, D. Stello, T. R. Bedding, T. L. Campante, R. Handberg, C. Karoff, Y. Elsworth, R. L. Gilliland, S. Hekker, D. Huber, S. D. Kawaler, H. Kjeldsen, M. N. Lund, and M. Lundkvist. Kepler-93b: A Terrestrial World Measured to within 120 km, and a Test Case for a New Spitzer Observing Mode. *ApJ*, 790:12, July 2014.
- [126] K. O. Todorov, D. Deming, H. A. Knutson, A. Burrows, J. J. Fortney, N. K. Lewis, N. B. Cowan, E. Agol, J.-M. Desert, P. V. Sada, D. Charbonneau, G. Laughlin, J. Langton, and A. P. Showman. Warm Spitzer Photometry of Three Hot Jupiters: HAT-P-3b, HAT-P-4b and HAT-P-12b. *ApJ*, 770:102, June 2013.
- [127] N. B. Lust, D. Britt, J. Harrington, S. Nymeyer, K. B. Stevenson, E. L. Ross, W. Bowman, and J. Fraine. Least Asymmetry Centering Method and Comparisons. *PASP*, 126:1092–1101, December 2014.
- [128] W. T. Reach, S. T. Megeath, M. Cohen, J. Hora, S. Carey, J. Surace, S. P. Willner, P. Barmby, G. Wilson, W. Glaccum, P. Lowrance, M. Marengo, and G. G. Fazio. Absolute Calibration of the Infrared Array Camera on the Spitzer Space Telescope. *PASP*, 117:978–990, September 2005.
- [129] P. R. McCullough, J. E. Stys, J. A. Valenti, C. M. Johns-Krull, K. A. Janes, J. N. Heasley, B. A. Bye, C. Dodd, S. W. Fleming, A. Pinnick, R. Bissinger, B. L. Gary, P. J. Howell, and T. Vanmunster. A Transiting Planet of a Sun-like Star. *ApJ*, 648:1228–1238, September 2006.
- [130] H. A. Knutson, D. Charbonneau, L. E. Allen, J. J. Fortney, E. Agol, N. B. Cowan, A. P. Showman, C. S. Cooper, and S. T. Megeath. A map of the day-night contrast of the extrasolar planet HD 189733b. *Nature*, 447:183–186, May 2007.
- [131] P. Cubillos, J. Harrington, N. Madhusudhan, K. B. Stevenson, R. A. Hardy, J. Blečić, D. R. Anderson, M. Hardin, and C. J. Campo. WASP-8b: Characterization of a Cool and Eccentric Exoplanet with Spitzer. *ApJ*, 768:42, May 2013.
- [132] N. K. Lewis, A. P. Showman, J. J. Fortney, M. S. Marley, R. S. Freedman, and K. Lodders. Atmospheric Circulation of Eccentric Hot Neptune GJ436b. *ApJ*, 720:344–356, September 2010.

- [133] A. P. Showman, J. Y.-K. Cho, and K. Menou. *Atmospheric Circulation of Exoplanets, Exoplanets, Ed. Sara Seager*, pages 471–516. Arizona Press, December 2010.
- [134] Jonathan Goodman and Jonathan Weare. Ensemble samplers with affine invariance. *Commun. Appl. Math. Comput. Sci.*, 5:65–80, 2010.
- [135] H. Ngo, H. A. Knutson, S. Hinkley, J. R. Crepp, E. B. Bechter, K. Batygin, A. W. Howard, J. A. Johnson, T. D. Morton, and P. S. Muirhead. Friends of Hot Jupiters. II. No Correspondence between Hot-jupiter Spin-Orbit Misalignment and the Incidence of Directly Imaged Stellar Companions. *ApJ*, 800:138, February 2015.
- [136] L. Kreidberg, J. L. Bean, J.-M. Désert, M. R. Line, J. J. Fortney, N. Madhusudhan, K. B. Stevenson, A. P. Showman, D. Charbonneau, P. R. McCullough, S. Seager, A. Burrows, G. W. Henry, M. Williamson, T. Kataria, and D. Homeier. A Precise Water Abundance Measurement for the Hot Jupiter WASP-43b. *ApJl*, 793:L27, October 2014.
- [137] A. Dressler, B. Bigelow, T. Hare, B. Sutin, I. Thompson, G. Burley, H. Epps, A. Oemler, A. Bagish, C. Birk, K. Clardy, S. Gunnels, D. Kelson, S. Sheckman, and D. Osip. IMACS: The Inamori-Magellan Areal Camera and Spectrograph on Magellan-Baade. *PASP*, 123:288–332, March 2011.
- [138] J. C. Brandt. A note on Rayleigh and Raman scattered Lyman- $\alpha$  radiation from Jupiter and Saturn. *P&SS*, 11:725–726, June 1963.
- [139] D. S. Hayes and D. W. Latham. A rediscussion of the atmospheric extinction and the absolute spectral-energy distribution of VEGA. *ApJ*, 197:593–601, May 1975.
- [140] L. D. G. Young and G. W. Kattawar. Scattering in the atmosphere of Venus. III - Line profiles and phase curves for Rayleigh scattering. *Icarus*, 30:360–366, February 1977.
- [141] R. K. Bhatia and K. D. Abhyankar. Intensity and polarization line profiles in a semi-infinite Rayleigh-scattering planetary atmosphere. I - Integrated flux. *Journal of Astrophysics and Astronomy*, 3:303–324, September 1982.
- [142] R. K. Bhatia and K. D. Abhyankar. Intensity and polarization line profiles in a semi-infinite Rayleigh-scattering planetary atmosphere. II - Variations of equivalent width over the disk. *Journal of Astrophysics and Astronomy*, 4:27–33, March 1983.
- [143] T. Viik. Flux and polarization reflected from a nonconservative Rayleigh-scattering planetary atmosphere. *Earth Moon and Planets*, 48:41–48, January 1990.

- [144] V. S. Meadows and D. Crisp. Ground-based near-infrared observations of the Venus nightside: The thermal structure and water abundance near the surface. *JGR*, 101:4595–4622, 1996.
- [145] J. Southworth. Homogeneous studies of transiting extrasolar planets - III. Additional planets and stellar models. *MNRAS*, 408:1689–1713, November 2010.
- [146] A. Lecavelier Des Etangs, A. Vidal-Madjar, and J.-M. Desert. The origin of hydrogen around HD 209458b. *Nature*, 456:1, November 2008.
- [147] D. K. Sing, J.-M. Désert, A. Lecavelier Des Etangs, G. E. Ballester, A. Vidal-Madjar, V. Parmentier, G. Hebrard, and G. W. Henry. Transit spectrophotometry of the exoplanet HD 189733b. I. Searching for water but finding haze with HST NICMOS. *A&A*, 505:891–899, October 2009.
- [148] N. Nikolov, D. K. Sing, F. Pont, A. S. Burrows, J. J. Fortney, G. E. Ballester, T. M. Evans, C. M. Huitson, H. R. Wakeford, P. A. Wilson, S. Aigrain, D. Deming, N. P. Gibson, G. W. Henry, H. Knutson, A. Lecavelier des Etangs, A. P. Showman, A. Vidal-Madjar, and K. Zahnle. Hubble Space Telescope hot Jupiter transmission spectral survey: a detection of Na and strong optical absorption in HAT-P-1b. *MNRAS*, 437:46–66, January 2014.
- [149] B. Macintosh, J. R. Graham, P. Ingraham, Q. Konopacky, C. Marois, M. Perrin, L. Poyneer, B. Bauman, T. Barman, A. S. Burrows, A. Cardwell, J. Chilcote, R. J. De Rosa, D. Dillon, R. Doyon, J. Dunn, D. Erikson, M. P. Fitzgerald, D. Gavel, S. Goodsell, M. Hartung, P. Hibon, P. Kalas, J. Larkin, J. Maire, F. Marchis, M. S. Marley, J. McBride, M. Millar-Blanchaer, K. Morzinski, A. Norton, B. R. Oppenheimer, D. Palmer, J. Patience, L. Pueyo, F. Rantakyro, N. Sadakuni, L. Saddlemyer, D. Savransky, A. Serio, R. Soummer, A. Sivaramakrishnan, I. Song, S. Thomas, J. K. Wallace, S. Wiktorowicz, and S. Wolff. First light of the Gemini Planet Imager. *Proceedings of the National Academy of Science*, 111:12661–12666, September 2014.
- [150] J.-L. Beuzit, M. Feldt, K. Dohlen, D. Mouillet, P. Puget, F. Wildi, L. Abe, J. Antichi, A. Baruffolo, P. Baudoz, A. Boccaletti, M. Carbillet, J. Charton, R. Claudi, M. Downing, C. Fabron, P. Feautrier, E. Fedrigo, T. Fusco, J.-L. Gach, R. Gratton, T. Henning, N. Hubin, F. Joos, M. Kasper, M. Langlois, R. Lenzen, C. Moutou, A. Pavlov, C. Petit, J. Pragt, P. Rabou, F. Rigal, R. Roelfsema, G. Rousset, M. Saisse, H.-M. Schmid, E. Stadler, C. Thalmann, M. Turatto, S. Udry, F. Vakili, and R. Waters. SPHERE: a 'Planet Finder' instrument for the VLT. In *Society of Photo-Optical Instrumentation Engineers (SPIE) Conference Series*, volume 7014 of *Society of Photo-Optical Instrumentation Engineers (SPIE) Conference Series*, page 18, July 2008.
- [151] K. I. Öberg, R. Murray-Clay, and E. A. Bergin. The Effects of Snowlines on C/O in Planetary Atmospheres. *ApJL*, 743:L16, December 2011.

- [152] E. A. Petigura, G. W. Marcy, and A. W. Howard. A Plateau in the Planet Population below Twice the Size of Earth. *ApJ*, 770:69, June 2013.
- [153] K. Zhang, G. A. Blake, and E. A. Bergin. Evidence of Fast Pebble Growth Near Condensation Fronts in the HL Tau Protoplanetary Disk. *ApJL*, 806:L7, June 2015.
- [154] K. B. Stevenson, J.-M. Désert, M. R. Line, J. L. Bean, J. J. Fortney, A. P. Showman, T. Kataria, L. Kreidberg, P. R. McCullough, G. W. Henry, D. Charbonneau, A. Burrows, S. Seager, N. Madhusudhan, M. H. Williamson, and D. Homeier. Thermal structure of an exoplanet atmosphere from phase-resolved emission spectroscopy. *Science*, 346:838–841, November 2014.
- [155] D. Deming, S. Seager, J. Winn, E. Miller-Ricci, M. Clampin, D. Lindler, T. Greene, D. Charbonneau, G. Laughlin, G. Ricker, D. Latham, and K. Ennico. Discovery and Characterization of Transiting Super Earths Using an All-Sky Transit Survey and Follow-up by the James Webb Space Telescope. *PASP*, 121:952–967, September 2009.
- [156] D. Huber and S.T. Bryson. K2: Extending Keplers Power to the Ecliptic. Technical report, NASA Ames Research Center, 2015.
- [157] H. Rauer, C. Catala, C. Aerts, T. Appourchaux, W. Benz, A. Brandeker, J. Christensen-Dalsgaard, M. Deleuil, L. Gizon, M.-J. Goupil, M. Güdel, E. Janot-Pacheco, M. Mas-Hesse, I. Pagano, G. Piotto, D. Pollacco, C. Santos, A. Smith, J.-C. Suárez, R. Szabó, S. Udry, V. Adibekyan, Y. Alibert, J.-M. Almenara, P. Amaro-Seoane, M. A.-v. Eiff, M. Asplund, E. Antonello, S. Barnes, F. Baudin, K. Belkacem, M. Bergemann, G. Bihain, A. C. Birch, X. Bonfils, I. Boisse, A. S. Bonomo, F. Borsa, I. M. Brandão, E. Brocato, S. Brun, M. Burleigh, R. Burston, J. Cabrera, S. Cassisi, W. Chaplin, S. Charpinet, C. Chiappini, R. P. Church, S. Csizmadia, M. Cunha, M. Damasso, M. B. Davies, H. J. Deeg, R. F. Díaz, S. Dreizler, C. Dreyer, P. Eggenberger, D. Ehrenreich, P. Eigmüller, A. Erikson, R. Farmer, S. Feltzing, F. de Oliveira Fialho, P. Figueira, T. Forveille, M. Fridlund, R. A. García, P. Giommi, G. Giuffrida, M. Godolt, J. Gomes da Silva, T. Granzer, J. L. Grenfell, A. Grotzsch-Noels, E. Günther, C. A. Haswell, A. P. Hatzes, G. Hébrard, S. Hekker, R. Helled, K. Heng, J. M. Jenkins, A. Johansen, M. L. Khodachenko, K. G. Kislyakova, W. Kley, U. Kolb, N. Krivova, F. Kupka, H. Lammer, A. F. Lanza, Y. Lebreton, D. Magrin, P. Marcos-Arenal, P. M. Marrese, J. P. Marques, J. Martins, S. Mathis, S. Mathur, S. Messina, A. Miglio, J. Montalbán, M. Montalto, M. J. P. F. G. Monteiro, H. Moradi, E. Moravveji, C. Mordasini, T. Morel, A. Mortier, V. Nascimbeni, R. P. Nelson, M. B. Nielsen, L. Noack, A. J. Norton, A. Ofir, M. Oshagh, R.-M. Ouazzani, P. Pápics, V. C. Parro, P. Petit, B. Plez, E. Poretti, A. Quirrenbach, R. Ragazzoni, G. Raimondo, M. Rainer, D. R. Reese, R. Redmer, S. Reffert, B. Rojas-Ayala, I. W. Roxburgh, S. Salmon, A. Santerne, J. Schneider, J. Schou, S. Schuh, H. Schunker, A. Silva-Valio, R. Silvotti, I. Skillen,

- I. Snellen, F. Sohl, S. G. Sousa, A. Sozzetti, D. Stello, K. G. Strassmeier, M. Švanda, G. M. Szabó, A. Tkachenko, D. Valencia, V. Van Grootel, S. D. Vauclair, P. Ventura, F. W. Wagner, N. A. Walton, J. Weingrill, S. C. Werner, P. J. Wheatley, and K. Zwintz. The PLATO 2.0 mission. *Experimental Astronomy*, 38:249–330, November 2014.
- [158] T. Kataria, A. P. Showman, J. J. Fortney, M. S. Marley, and R. S. Freedman. The Atmospheric Circulation of the Super Earth GJ 1214b: Dependence on Composition and Metallicity. *ApJ*, 785:92, April 2014.
- [159] R. Angus, S. Aigrain, D. Foreman-Mackey, and A. McQuillan. Calibrating gyrochronology using Kepler asteroseismic targets. *MNRAS*, 450:1787–1798, June 2015.
- [160] S. Aigrain, S. T. Hodgkin, M. J. Irwin, J. R. Lewis, and S. J. Roberts. Precise time series photometry for the Kepler-2.0 mission. *MNRAS*, 447:2880–2893, March 2015.
- [161] K. M. Deck, E. Agol, M. J. Holman, and D. Nesvorný. TTVFast: An Efficient and Accurate Code for Transit Timing Inversion Problems. *ApJ*, 787:132, June 2014.
- [162] D. Jontof-Hutter, J. F. Rowe, J. J. Lissauer, D. C. Fabrycky, and E. B. Ford. The mass of the Mars-sized exoplanet Kepler-138 b from transit timing. *Nature*, 522:321–323, June 2015.
- [163] K. M. Deck and K. Batygin. Migration of two massive planets into (and out of) first order mean motion resonances. *ArXiv e-prints*, June 2015.
- [164] J. C. Mather. The James Webb Space Telescope Mission. In D. J. Whalen, V. Bromm, and N. Yoshida, editors, *American Institute of Physics Conference Series*, volume 1294 of *American Institute of Physics Conference Series*, pages 1–8, November 2010.
- [165] G. S. Wright, G. H. Rieke, L. Colina, E. van Dishoeck, G. Goodson, T. Greene, P.-O. Lagage, A. Karnik, S. D. Lambros, D. Lemke, M. Meixner, H.-U. Norgaard, G. Oloffson, T. Ray, M. Ressler, C. Waelkens, D. Wright, and A. Zhen-der. The JWST MIRI instrument concept. In J. C. Mather, editor, *Optical, Infrared, and Millimeter Space Telescopes*, volume 5487 of *Society of Photo-Optical Instrumentation Engineers (SPIE) Conference Series*, pages 653–663, October 2004.
- [166] B. M. Swinyard, G. H. Rieke, M. Ressler, A. Glasse, G. S. Wright, M. Ferlet, and M. Wells. Sensitivity estimates for the mid-infrared instrument (MIRI) on the JWST. In J. C. Mather, editor, *Optical, Infrared, and Millimeter Space Telescopes*, volume 5487 of *Society of Photo-Optical Instrumentation Engineers (SPIE) Conference Series*, pages 785–793, October 2004.

- [167] J. Köhler, M. Melf, W. Posselt, W. Holota, and M. te Plate. Optical design of the near-infrared spectrograph NIRSpec. In L. Mazuray and R. Wartmann, editors, *Optical Design and Engineering II*, volume 5962 of *Society of Photo-Optical Instrumentation Engineers (SPIE) Conference Series*, pages 563–574, September 2005.
- [168] M. J. Rieke, D. Kelly, and S. Horner. Overview of James Webb Space Telescope and NIRCams’s Role. In J. B. Heaney and L. G. Burriesci, editors, *Cryogenic Optical Systems and Instruments XI*, volume 5904 of *Society of Photo-Optical Instrumentation Engineers (SPIE) Conference Series*, pages 1–8, August 2005.
- [169] T. Greene, C. Beichman, D. Eisenstein, S. Horner, D. Kelly, Y. Mao, M. Meyer, M. Rieke, and F. Shi. Observing exoplanets with the JWST NIRCam grisms. In *Society of Photo-Optical Instrumentation Engineers (SPIE) Conference Series*, volume 6693 of *Society of Photo-Optical Instrumentation Engineers (SPIE) Conference Series*, page 0, September 2007.
- [170] R. Doyon, J. B. Hutchings, M. Beaulieu, L. Albert, D. Lafrenière, C. Willott, D. Touahri, N. Rowlands, M. Maszkiewicz, A. W. Fullerton, K. Volk, A. R. Martel, P. Chayer, A. Sivaramakrishnan, R. Abraham, L. Ferrarese, R. Jayawardhana, D. Johnstone, M. Meyer, J. L. Pipher, and M. Sawicki. The JWST Fine Guidance Sensor (FGS) and Near-Infrared Imager and Slitless Spectrograph (NIRISS). In *Society of Photo-Optical Instrumentation Engineers (SPIE) Conference Series*, volume 8442 of *Society of Photo-Optical Instrumentation Engineers (SPIE) Conference Series*, page 2, September 2012.
- [171] C. Beichman, B. Benneke, H. Knutson, R. Smith, P.-O. Lagage, C. Dressing, D. Latham, J. Lunine, S. Birkmann, P. Ferruit, G. Giardino, E. Kempton, S. Carey, J. Krick, P. D. Deroo, A. Mandell, M. E. Ressler, A. Shporer, M. Swain, G. Vasisht, G. Ricker, J. Bouwman, I. Crossfield, T. Greene, S. Howell, J. Christiansen, D. Ciardi, M. Clampin, M. Greenhouse, A. Sozzetti, P. Goudfrooij, D. Hines, T. Keyes, J. Lee, P. McCullough, M. Robberto, J. Stansberry, J. Valenti, M. Rieke, G. Rieke, J. Fortney, J. Bean, L. Kreidberg, D. Ehrenreich, D. Deming, L. Albert, R. Doyon, and D. Sing. Observations of Transiting Exoplanets with the James Webb Space Telescope (JWST). *PASP*, 126:1134–1173, December 2014.
- [172] S. Seager. The future of spectroscopic life detection on exoplanets. *Proceedings of the National Academy of Science*, 111:12634–12640, September 2014.